UNIVERSITÀ DEGLI STUDI DI PADOVA

Technical University of Denmark

UNIVERSITA' DEGLI STUDI DI PADOVA

Dipartimento di Ingegneria Industriale DII

Dipartimento di Ingegneria dell'Informazione DEI

Corso di Laurea Magistrale in Ingegneria Aerospaziale

Multi-Objective Optimal Control of Multi-Rotor Wind Turbine

Relatori:

Prof.ssa Maria Elena Valcher

Prof. Roberto Galeazzi

Dimitrios Papageorgiou Postdoc

Jesper Sandberg Thomsen

Studente:

Fabio Spagnolo 1151903

Anno Accademico 2018/2019

Firma del Relatore:

Padova, lì

Abstract (IT)

Negli ultimi anni, la maggiore consapevolezza del cambiamento climatico e la sempre crescente domanda di energia, hanno favorito un aumento della potenza nominale delle turbine eoliche. Le sempre maggiori dimensioni raggiunte dalle Single Rotor Turbine (SRT) tradizionali comportano diverse sfide tecnologiche, poiché il costo del rotore cresce più velocemente della potenza guadagnata. Al contrario di una Single Rotor Turbine (SRT), una Multi Rotor Turbine (MRT) consente di contenere il costo del rotore, a parità di potenza prodotta, perché la struttura di supporto ospita più SRTs e di minor dimensione. Inevitabilmente, la soluzione multi-rotore ha un impatto negativo sul costo e sulla complessità della struttura di supporto. Risulta di fondamentale importanza, quindi, mitigare gli effetti della fatica, così da estendere la vita della struttura di supporto.
L'obiettivo del progetto è di proporre, testare e valutare una strategia di controllo integrata che, attraverso un'adeguata coordinazione delle SRTs, possa mitigare la fatica strutturale senza compromettere sensibilmente la potenza prodotta. Questo progetto studia una possibile soluzione al problema di coordinazione nell'area dell'ottimizzazione multi-obiettivo e in particolare, utilizzando l'Extremum Seeking Control (ESC). L'ESC è una tecnica di ottimizzazione in grado di stimare il segnale di riferimento che ottimizza una funzione di costo non nota. La tecnica si basa esclusivamente sulla misurazione della funzione di costo.
L'architettura proposta sfrutta l'ESC per stimare il segnale di pitch in ingresso ad ogni SRT nella Full Load Region (FLR). Lo schema non utilizza alcuna misura della velocità del vento e non include alcun modello dinamico del sistema in fase operativa. Alla sintesi del primo ESC segue la simulazione. La comparazione con il Benchmark controller (BMC) evidenzia prestazioni simili in termini di regolazione della velocità del generatore e produzione media di potenza. Tuttavia, lo schema ha chiaramente un impatto negativo sulla fatica. Dall'analisi spettrale si evince che la power density in eccesso introdotta dai segnali di pitch, si propaga attraverso le forze di spinta nella struttura, aumentando così la fatica. Due tecniche di mitigazione sono sviluppate al fine di ridurre l'eccesso di power density. La prima tecnica introduce un filtro passa-basso all'ESC. La seconda, invece, si basa sulla riformulazione del costo misurato, aggiungendo un termine connesso alla fatica. Entrambe le tecniche consentono una riduzione sostanziale della fatica se comparate con il primo ESC. Tuttavia, non è stato possibile ottenere prestazioni simili al Benchmark controller (BMC).
Concludendo, l'ESC è una tecnica model-free efficace nel regolare la velocità del generatore e nel mantenere una adeguata produzione media di potenza. Le simulazioni e le

analisi svolte nell'ambito del progetto, dimostrano che la stima diretta degli angoli di pitch da parte dell'ESC non è efficace al fine di ridurre la fatica strutturale.

Abstract (EN)

In recent years, the increased awareness of climate change and the ever expanding energy demand, boosted a growth in the power rating of wind turbines. The scaling-up of a traditional Single Rotor Turbine (SRT) poses multiple challenges because the cost of the rotor increases faster than the gained power. Compared to the SRT, the Multi Rotor Turbine (MRT) offers a lower rotor cost to produced power ratio because it mounts more SRTs of smaller size on the same support structure. With more rotors being attached, the cost and the complexity of the support structure increases. As a matter of fact, it becomes crucial to mitigate the effect of fatigue in order to extend the life of the support structure.

The goal of the project is to propose, test and evaluate an integrated control strategy that, by proper coordination of the SRTs, is capable to mitigate structural fatigue with little to no impact on produced power. This project investigates a solution to the coordination problem in the area of Multi Objective Optimization and in particular, using ESC. ESC is an optimization technique that estimates the reference set-points to optimize an unknown cost function. The technique relies only on measurements of the cost.

The proposed ESC based architecture estimates the pitch reference set-points of each SRT in Full Load Region (FLR), without any knowledge of the wind speed and of the plant model, during operation. The first ESC design is tuned and compared through simulation against the Benchmark controller (BMC), obtaining comparable performance in terms of generator speed regulation and mean power production. However, the scheme has a clear negative impact on fatigue. In fact, the spectral analysis shows that extra power density is injected by the pitch references, that propagates through the thrust forces into the structure, causing higher fatigue. Therefore, two mitigation strategies are proposed to reduce the extra power density. In the first case, a low pass filter is included in the ESC. Instead, the second approach requires the reformulation of the measured cost to include a fatigue related term. Both strategies achieve substantial fatigue mitigation compared to the first ESC, although it was not possible to mimic the performance of the BMC.

It is concluded that ESC is a powerful model-free technique suitable to achieve generator speed regulation and desired mean power production. However, to the extent of the carried out simulations and analysis, ESC is not suitable to achieve fatigue mitigation by direct estimation of the pitch references.

Preface

The thesis work was carried out at the Department of Electrical Engineering - Automation and Control of Technical University of Denmark, at Vestas Wind System in Århus (Dk) and at the Department of Information Engineering of University of Padova, in partial fulfilment of the requirements for acquiring the M.Sc. in Electrical Engineering and the M.Sc. in Aerospace engineering.

Acknowledgements

I would first like to thank Jesper Sandberg Thomsen, my supervisor at Vestas Wind Systems, for sharing his knowledge and expertise about wind turbines control with me. I would like to thank my supervisors at DTU Prof. Roberto Galeazzi, Dimitrios Papageorgiou Postdoc for their support, whenever I ran into a trouble spot or had a question about my research or writing. I would also like to thank my supervisor at the University of Padova, Prof. Maria Elena Valcher, for the valuable feedback provided during the writing of the thesis.
Last but not least, I am grateful to my parents and my girlfriend Beatrice for providing me with support and encouragement throughout my years of study and through the process of researching and writing this thesis.

Contents

List of Figures

List of Tables

Acronyms

BEM Blade element momentum. 7

BMC Benchmark controller. i, iii, xii–xiv, 3, 5, 18, 46–50, 54–58, 62–64, 68, 69, 73–75, 79, 81–83

DEL Damage Equivalent Load. xii–xiv, 9, 47, 54–59, 62, 63, 67–73, 76, 78, 79

DOF Degree of Freedom. xi, 18

ESC Extremum Seeking Control. i–iii, xii–xiv, xvii, xviii, 2, 3, 5, 9, 10, 12, 19, 21, 22, 24, 27–31, 33–37, 39, 40, 42, 43, 45–48, 52, 58–76, 78, 79, 81, 82, 87

ETM Extreme Turbulence Model. 45

EWS Effective wind speed. xvii, 7

FLR Full Load Region. i, iii, 3, 6, 12, 17, 19, 29, 36, 45, 61, 68, 81, 82

FM Fatigue mitigation. x, xiii, xiv, 70–77, 79, 81, 82

HO Hysteresis operator. 9

LPF low pass filter. x, xii–xiv, 62–65, 70, 73, 76, 77, 79, 81, 82

LQR Linear Quadratic Regulator. 10

LTI Linear Time Invariant. 87

MC Markov chain. 9

MISO Multiple Input Multiple Output. 11, 29

MOOP Multi Objective Optimization Problem. 7

MOOPs Multi Objective Optimization Problems. 5

MPC Model Predictive Control. 9, 10

MPPT maximum power point tracking. 10–12

MRT Multi Rotor Turbine. i, iii, xi, xiv, xvii, 1–3, 5, 10, 12–15, 19, 21, 27–30, 43, 45, 54, 58, 59, 61, 68

NREL National Renewable Energy Laboratory. 14

NTM Normal Turbulence Model. xii, 45, 46

PESC Perturbation Based ESC. x–xiv, 11, 12, 21–23, 27, 30, 31, 33, 35, 37, 39, 41, 45–50, 52, 54–58, 62–65, 70, 72–79, 81, 82

PLR Partial Load Region. 3, 11, 12, 17

PSD Power Spectral Density. xii, xiii, 50, 51, 54–59, 62–64, 69, 71, 73–76, 78

PVC Photovoltaic converters. 11

R&D Research & Development. 1

RFC Rainflow counting. 9

SISO Single Input Single Output. x, xi, 11, 29–31, 33, 35, 81

SM Spectral methods. 9

SRT Single Rotor Turbine. i, iii, xi, 1–3, 6, 9, 10, 12–15, 17–19, 21, 27–30, 34–37, 40–42, 45, 55, 61–63, 65–73, 76, 77, 81, 87

std standard deviation. 8

TOC Traditional Optimal Control. 9, 10

TSR Tip to Speed Ratio. 7

VSVP Variable-Speed Variable-Pitch. xi, 17, 18

WECS Wind Energy Capture System. 10–13

WECSs Wind Energy Capture Systems. 5

WF Wind Farm. 5–8, 10

List of Symbols

The List of Symbols in the following is divided into two sections, namely Model and ESC. Model collects the most relevant symbols regarding the Multi Rotor Turbine (MRT) and its subsystems. Instead ESC collects the most relevant symbols utilized to define Extremum Seeking Control (ESC).

Model

C_p: Power coefficient
C_t: Thrust coefficient
a: Axial induction factor
ρ: air density (kg/m^3)
A: Rotor area (m^2)
R: Rotor radius (m)
λ: Tip-speed ratio
Ω_g: Generator rotational speed (rad/s)
Ω_r: Rotor rotational speed (rad/s)
Ω_N: Generator rated speed (rad/s)
V: Wind speed (m/s)
$\hat{v}_e$: Effective wind speed (EWS) estimation (m/s)
V_{min}: Cut-in wind speed (m/s)
V_{max}: Cut-off wind speed (m/s)
V_{Ω_N}: Wind speed at Ω_N (m/s)
V_N: Rated wind speed (m/s)
V_{rot}: Relative wind speed to the rotor (m/s)
N: Drive-train gear-ratio
τ_g: Generator torque (MNm)
τ_r: Rotor torque (MNm)
P_{nw}: Network power demand (MW)
P_{ref}: Power reference (MW)
$P_{out,i}$: I-th power output (MW)
P_N: Rated Power (MW)
$F_{t,i}$: I-th thrust force (MN)
$V_{y,i}$: I-th nacelle fore-aft (along Y) velocity (m/s)
β: Pitch angle (°)

t_β: Pitch actuator time constant
ϕ: Shaft torsional angle (rad)
K_{shaft}: Shaft torsional spring constant (MNm/rad)
B_{shaft}: Shaft viscous friction constant (MNms/rad)
I_r: Rotor inertia (MNms^2/rad)
I_g: Generator inertia (MNms^2/rad)
ϵ_g: Generator efficiency
t_g: Generator time constant

Extremum Seeking Control (ESC)

$\mathcal{L}$: Laplace transform
$\mathcal{C}^2$: Of class C 2
σ: Standard deviation
σ^2: Variance
θ: Reference set point
θ^*: Optimal reference set-point
y: Measured output
$f(\theta)$: Unknown mapping
f^*: Extremum of the unknown mapping, i.e. $f^* := f(\theta^*)$
f'': Second derivative of the unknown mapping evaluated at θ^*
$\tilde{\theta}$: Estimation error
$\hat{\theta}$: Estimated reference set-point
a_p: Perturbation amplitude
ω_p: Perturbation frequency (rad/s)
$-h$: High pass filter pole (rad/s)
y_{hp}: High pass filter output
ξ: Demodulation output
k: Integrator gain
$F_i(s)$: Input plant dynamics transfer function
$F_o(s)$: Output plant dynamics transfer function
$WF(s)$: Washout filter transfer function
$C_o(s)$: Output compensator transfer function
k_{wf}: Washout filter gain
λ_θ: Gain of the transfer function of $\theta^*(t)$
λ_f: Gain of the transfer function of $f^*(t)$
Γ_θ: Shape of the transfer function of $\theta^*(t)$
Γ_f: Shape of the transfer function of $f^*(t)$
y_{wf}: Washout filter output
$DM(t)$: Demodulation signal
ϕ: Phase of the demodulation signal (rad)

$D(t)$: Dithering signal
$EA(s)$: Estimation algorithm transfer function
$C_i(s)$: Input compensator transfer function
$-p$: Washout filter pole (rad/s)
k_i: Integral gain
k_p: Proportional gain
W_i: I-th trade-off gain
σ_{F_i}: Standard deviation of the fatigue term
σ_{Ω_g}: Standard deviation of the generator speed term

CHAPTER 1

Introduction

1.1 Project in Context

The rural landscape sometimes brings the signs of a pre-industrial past when wind energy used to be exploited in many ways, from water pumping to grain milling. With the advent of the industrial revolution, fossil fuels progressively took over wind energy. The concept of converting wind to electrical power was developed in the 20th century and the first prototypes were utilized mainly to recharge batteries. The oil price crisis in the early 70s acted as a trigger for the development of modern wind turbines. At that time ambitious Research & Development (R&D) programs were promoted in many countries. As a consequence new materials and new designs were developed, marking the rise of large-scale wind turbines. Since then the market has been growing fast, supported by incentives, government policies and reduction in the technology cost [5].
In the past twenty years increased awareness of the climate threat and the goal of differentiating energy provision sources induced a growth in turbine size. The growth rate, once exponential, has leveled nowadays. Nevertheless state-of-the-art onshore wind turbines exceed 4 MW rated power while this value reaches 9 MW for offshore [23].

1.2 Background and Motivation

Improving power ratings was the goal of UPWIND, the Europe's largest wind energy R&D project [13]. It addressed the problem of both offshore and onshore power up-scaling towards >8-10 MW by 2020. The consortium operated to develop reliable tools and component concepts needed to design and manufacture very large turbines.
All commercially successful wind turbines have been horizontal axis Single Rotor Turbine (SRT) with one rotor and nacelle placed on top of a tower. Scaling-up the SRT concept towards higher power ratings poses multiple challenges. In fact the weight of the rotor increases by the cube of the radius while the power does by the square. As such the cost of the rotor material increases faster than the gained power.
An alternative to SRT is the Multi Rotor Turbine (MRT) (Figure 1.1). The MRT [23] offers a lower rotor cost to produced power ratio than the SRT because it mounts more nacelles on the same structure. For example, a 4 rotor MRT would quadruple the power output by quadrupling the rotor cost. Conversely, an SRT would increase the rotor cost by 8 times to achieve the same power output.
The main downside of the MRT is the added complexity and larger cost of the support

structure. Having more rotors and nacelles attached introduces extra excitation to the structural modes and might worsen fatigue [23].

Figure 1.1: The Vestas MRT demonstrator consisting of 4 V29 225 kW nacelles and rotors. Location: DTU Risø in Roskilde Denmark. Image Courtesy Vestas Wind Systems A/S.

1.3 Project Goal

Mitigation of structural fatigue is crucial to extend the operational life of the MRT, which in turn has a positive impact on the total cost per kWh [14]. However, the total cost per kWh [14] might increase, in the case fatigue mitigation coincides with an excessive reduction of the produced power. Consequently, the control challenge described in [23] seeks the minimization of structural fatigue and the maximization of the produced power of the MRT. Based on the control challenge in [23], the goal of the project is to identify, implement and test an integrated control system architecture that by proper coordination of the individual SRTs can decrease support structure loads of the MRT with little to no impact on produced power.

1.4 Project Scope

The project seeks solutions to the SRTs coordination problem in the area of multi-objective optimization by means of Extremum Seeking Control (ESC). The proposed ESC based architecture will provide the existing low level SRT control systems with optimal pitch reference set-points. The ESC will be designed and tuned to operate the

MRT above rated wind speed [1] according to the benchmark weather conditions in [23]. Comparison of the ESC against the Benchmark controller (BMC) from [23] will focus on

1. Generator speed regulation
2. Power production
3. Fatigue on the support structure

As it will be shown, the chosen ESC technique involves demodulation and dithering processes to compute the optimal set-point to each SRT. In doing so, ESC injects sinusoidal perturbations to the set-point that propagate from the blades through the drive train and finally into the structure. The project will also evaluate the impact of the sinusoidal perturbations on fatigue and investigate the effectiveness of mitigation techniques. Comparisons against the ESC introduced above will focus on conditions 1 to 3.

1.5 Thesis Outline

The body of the thesis develops as follows. In Chapter 2 a literature study regarding the topics relevant to the project is carried out. The main contributions of the project to the state of the art are then outlined.
Chapter 3 describes the subsystems of the MRT and their interconnections. The second part of the chapter deals with modelling. At the end of the chapter the operating assumptions are introduced.
Chapter 4 is dedicated to Extremum Seeking Control (ESC). To begin with, an example of ESC applied to a static map is showed to explain the working principle and the advantages of the method. In the following section an ESC based architecture is proposed to compute the pitch reference to each SRT. The relevant theory is presented to support the steps that lead to the design of the ESC loops at the end of the chapter. Chapter 5 opens with the detailed assumptions about the testing scenario, and performance assessment. The ESC is tuned to achieve performance that is comparable to the BMC in terms of generator speed regulation and power production. The second part of the chapter compares the ESC against the BMC in terms of fatigue on the support structure.
Two fatigue mitigation techniques are developed in Chapter 6. The first one implies a new ESC design, whereas the second one requires a change of the measured cost. The updated ESC schemes are compared against the ESC developed in Chapter 5.
Based on the results reported in Chapters 5 and 6, Chapter 7 outlines the main conclusions of the project and elaborates some suggestions for future work.

[1] A formal definition of the terms rated wind speed, Partial Load Region (PLR) and Full Load Region (FLR) is provided in Chapter 3.

CHAPTER 2

Literature Review

The aim of this chapter is to carry out a literature study of the relevant topics to the thesis. The study focuses on methods for the solution of structurally similar problems. Great emphasis is put on power optimization and fatigue mitigation of Wind Farm (WF) as well as on ESC methods for the solution of Multi Objective Optimization Problems (MOOPs). Applications of ESC to Wind Energy Capture Systems (WECSs) are reported. Finally the chapter outlines the main contributions of this project to the state of art.

2.1 Power Optimization and Fatigue Mitigation of Wind Farms

Apart from the BMC approach made by Vestas, to the best knowledge of the author no other attempts have been made to solve the MRT control challenge. An MRT can be thought of as a four-nacelles wind farm, where each rotor is mounted on the same support. Although MRT differs from a Wind Farm (WF) in terms of loads coupling, their structural similarities justify investigating state of the art solutions to the same control challenge applied to WFs. Detailed surveys [21],[22] reference the research work within this field. Section 2.2 is based on both surveys though explicit reference to specific papers is made only when relevant.

2.1.1 Control Objectives

The control problem pertains to generating optimal references to each turbine nacelle as the outcome of a multi-objective optimization problem with a trade-off between power tracking and load mitigation. According to [21],[22] this trade-off is usually expressed by the following cost function

$$J(\mathbf{x}) = c_1(\sum_i P_i - P_{f,ref})^2 + c_2 F(\mathbf{x}) \tag{2.1}$$

$\mathbf{x}$ being the decision vector, i.e. the variables the routine optimizes for. The cost function comprises two terms. $(\sum_i P_i - P_{f,ref})^2$ is the squared difference between the total

produced power by the WF and the required power reference. The power reference is bounded from above by the power curve at the current wind speed. The scalars c_1 and c_2 are the corresponding weights of the two terms. $F(\mathbf{x})$ is a fatigue load dependant term. Common approaches to describe fatigue are described in Section 2.1.3. Typically the aim is to minimize (2.1) for either the steady state and nominal value [20], or the current expected value [24],[6] or even along a finite time horizon [28].
The authors in [22] point out that adopting (2.1) as cost function allows for power deviation from the reference. In FLR such a choice of cost function may even lead to a situation where a turbine exceeds its rated power. This, however, can be avoided by adopting a constrained optimization, i.e. by specifying constraints on the maximum power output.

2.1.2 Control Architectures

As suggested in [22] the word control architecture should be intended as the ensemble of sensors, actuators, controllers and their interconnections.
From a communication perspective three different approaches are described in [22]:

- *Centralized control.* All sensors and actuators communicate directly with one central control. Conceptually the most straightforward, this method increases the complexity of the communication system especially when the WF is made by hundreds of turbines.
- *Distributed control.* Communication is limited to the turbine nearest neighbours. This method provides sub-optimal solutions compared to the *centralized* ones. It works under the assumption that the turbines in a WF are mainly influenced by the closest upwind and downwind neighbours.
- *Cascade control.* The control is centralized but hierarchical. At the WF level a slow controller handles the WF flow and the interactions between the SRTs. This control does not capture any details of the SRT dynamics. Instead at the SRT level a fast controller regulates a detailed dynamical model of the turbine though no interaction effect is captured.

In the literature authors utilize a variety of control input and output. The control architecture should rely on accurate signals already available in commercial WFs or realistic to measure in the future. A design based on uncertain measurements or difficult to obtain signals will likely perform poorly on the real system.

Control Input [22] cites many papers that assume accurate wind speed measurements. This assumption is quite strong because most of the commercial control solutions for

wind turbines do not rely on wind measurements. Instead an EWS estimator is recommended by the authors of [22].
Power is a common input in power tracking applications. This measurement is readily available with the only limitation on communication bandwidth.
Finally mechanical loads need to be measured in a loads mitigating control strategy. Measures of fatigue can be obtained by means of tower accelerometers, available on commercial products.

Control Output It is expected that the WF control can at least regulate the individual power extraction. Different decision variables can be chosen. Some controllers directly set the power reference [24], [6]. Another approach is to compute the power reference based on the axial induction factor a and the results from Blade element momentum (BEM) and actuator disk theory [25],[16]. The power coefficient C_p is conveniently stated as a function of a and it measures the ratio of extracted power to wind power [5]. Knowledge of the wind speed v_e, in fact of the EWS $\hat{v}_e$, is necessary to obtain P_{ref}. The expressions of the power coefficient and of the reference power are reported below in (2.2)

$$C_p = 4a(1-a)^2 \tag{2.2}$$

$$P_{ref} = \frac{1}{2}\rho A C_p \hat{v}_e^3 \tag{2.3}$$

A being the area spanned by the rotor and ρ being the air density.
The pitch angle can be utilized directly as a reference signal [27],[28] or be converted to a power reference. According to [22], the conversion requires measurements of the generator rotational speed Ω_g and an EWS estimate. A C_p look-up table is also necessary. Typically C_p look-up tables are provided as a function of the pitch angle and the Tip to Speed Ratio (TSR) λ [5]. λ is the ratio between the linear velocity at the rotor tip and the wind speed as shown below

$$\lambda = \frac{\Omega_r R}{V} = \frac{\Omega_r R N}{V} \tag{2.4}$$

where Ω_r is the rotor angular velocity in rad/s, R is the rotor radius in m, V is the wind speed acting on the rotor in m/s and N is the gear ratio between the rotor shaft and the generator shaft [5]. λ can also be utilized as decision variable [22] and then converted to a generator speed reference. The conversion can easily be performed by inverting (2.4) and it relies on an EWS estimate.

2.1.3 Description of Fatigue

The line of thought regarding fatigue began with the work of Kazda et al.[21] about WF Multi Objective Optimization Problem (MOOP). The authors highlight the complexity

of describing fatigue for control purposes in WFs. Among the other sources the article points to the Survey Paper from Knudsen et. al. [22]. The damage caused by fatigue on a material accumulates over time. It is caused by structural stress whose intensity is much less than the ultimate tensile stress. Instead, the ultimate tensile stress is the maximum stress level a material can withstand before breaking. Let us assume that the stress history of the structure is sinusoidal with a certain frequency. Then the structure responds to the stress with sinusoidal oscillations whose amplitudes depend on the frequency of the input stress. According to the authors in [22], the accumulated fatigue damage due to the stress history is quantified as the number of cycles multiplied by the amplitude of the oscillations. By the number of cycles it is meant how many times a full oscillation repeats. If more amplitudes are present, the accumulated damage can be summarized as

$$F = \sum_i N_i A_i^m \tag{2.5}$$

A_i being the i-th amplitude, N_i being the number of sinusoidal cycles at that amplitude, m being the Wöhler exponent [22]. Two consequences follow from (2.5)

- constant stress gives zero fatigue;
- non-zero standard deviation (std) on the stress implies non-zero fatigue. However, std alone does not provide any information about the size of fatigue. In fact, that std may stem from both a very low frequency and a very high frequency signal.

Knudsen et al. [22] apply those concepts to the wind turbine tower reaching the following conclusions

- Constant tower thrust of any size gives zero fatigue.
- The fatigue is not monotonic in the tower thrust std vuoi dire: The fatigue is not a monotonic function of the tower thrust std? because the tower response depends on the frequency content of the thrust. For example, a fixed tower thrust std with frequencies below the tower resonance will give medium tower movements. In contrast, large movements will be produced if the frequencies are close to the resonance, and small movements will be produced if the frequencies are quite higher than resonance.
- Even the std of the tower movement does not provide any information about fatigue because the std says nothing about the frequency contents that affect the cycle count.

However, the authors in [22] refer to papers that could reduce fatigue by including thrust related terms in the cost function.

Given an arbitrary stress history, the number of cycles and the amplitudes are estimated by *rainflow counting* [3]. Estimated amplitudes and number of cycles are summed up to generate Damage Equivalent Load (DEL). The same approach is utilized to estimate loads impact in the benchmark model [23].
From a control perspective, it would be desirable to include online estimation of the fatigue loads, possibly based on *rainflow counting*. Though *rainflow counting* is widely accepted and represents a standard in fatigue quantification yet it can be utilized only for post-processing purposes because it is a very non-linear numerical algorithm.
Different options to represent fatigue are compared by Barradas-Berglind and Wisniewski [3]. Specifically the survey compares Rainflow counting (RFC), Spectral methods (SM), Markov chain (MC) and Hysteresis operator (HO) methods. Among them only the last two can be implemented online and, as a result are of interest from a control perspective.
MCs are well studied and have been successfully used in control settings. They can address time-varying loads. A MC is defined based on the intensity or transition matrix Q. Unfortunately the expression of Q is unknown and it depends on the load. This fact makes not convenient to apply MCs in fatigue relieving control techniques.
The approach presented in [3] focuses on HO methods. Based on the conclusions developed in the paper [7] and in the textbook [8]. The authors of [3] formalize the process involved in *rainflow counting* as hysteresis operators. As such, the authors of [3] obtain an online representation of fatigue, that can be incorporated, for instance, in the cost functional of a Model Predictive Control (MPC). Consequently, the MPC would take into consideration the effect of fatigue over time and mitigate it. This method has been successfully applied by Barradas-Berglind and Wisniewski in [4] to mitigate power fluctuations and the incurred fatigue on the rotor shaft of an SRT.

2.2 Control Strategies

This section reviews some of the available methods to solve the optimization problem stated in Section 2.2 and it is mainly based on the surveying work by Zhang et al. [32]. The first chapter proposes a compatible and general formulation of the problem of interest as follows

$$\min J(\mathbf{x}) \text{ subject to } \dot{\mathbf{x}} = f(\mathbf{x}, \mathbf{u}), \tag{2.6}$$

where $\mathbf{x}$ is the state vector. Solving (2.6) constitutes the common thread of three control approaches, namely Traditional Optimal Control (TOC), MPC and ESC. Besides that, ESC solves a different problem compared to TOC and MPC. ESC computes a set of references for the system such that the cost function is minimized. It also relies on a closed-loop controller to steer the system towards the optimal operating reference. Instead TOC and MPC generate an input signal *u(t)* which is valid over some time

interval. In TOC the control input aims at following a trajectory, while in MPC the optimization objective is trying to approximate an optimal trajectory.
References in [22] point to approaches to solve the WF optimization problem as an MPC or a Linear Quadratic Regulator (LQR) (TOC) problem. Both methods are based on convex quadratic optimization, which does not lead to local minima. Furthermore, the resulting controllers are guaranteed to be stable. Despite ensuring optimization convexity and controller stability, the usefulness of those methods is highly dependent on how well assumptions on the model and objectives fit to the real plant.
According to [21], model-free techniques provide the value of the cost function exclusively through measurements. For instance, the authors in [21] refer to a paper that solves the WF power maximization problem utilizing game theory [25]. Data-driven adaptive schemes have also been applied to solve the WF maximum power point tracking (MPPT) problem [16].
In the same fashion ESC does not assume perfect knowledge of the cost function. Instead, it is based on the measurements of the cost function or its derivatives, if available [32]. ESC can track in real time the parameters that optimize the system cost function when off-line computation of the parameters is impractical or there is no reliable model to predict the variation of the cost function. Clearly measurements uncertainty heavily impacts performance [21]. On the one hand performance is more or less independent of the quality of the WF model. On the other hand convergence towards the optimum can be slower than in model-based techniques because in-operational learning requires an initial optimization period.
As stated in Section 1.4 the proposed architecture is meant to eventually provide each SRT with a pitch reference as the result of an optimization process. As a matter of fact the proposed architecture would not focus on the actuation of the reference set-points because each SRT includes already low-level controllers to actuate the pitch and the power references, as it will be explained in Chapter 3. In Wind Energy Capture Systems (WECSs) the pitch angle as well as the generator speed and the produced power change with the wind operating point [5]. Hence, an ESC might be useful to generate the needed time-varying reference set-points without relying on wind speed measurements or on the knowledge of the MRT model. Based on the considerations above the MRT control challenge will be addressed by means of an ESC based scheme.

2.2.1 ESC Literature Overview

This section provides a brief overview of the history of ESC as well as the available methods to implement it. It also refers to real applications with greater emphasis on energy capture systems. The section is based on the survey by Zhang [32] unless a different reference is explicitly cited.
ESC was first proposed by Leblanc in 1922 and became popular already during 1950s and 60s. Since the publication of stability proofs for perturbation-based ESC by Kristic and his team in the early 2000s [1], researchers showed a renewed interest in the topic.
Real applications range from agent and sensor networks to automotive, process control,

flow control, plasma control and PID tuning.

2.2.1.1 Analog Optimization Based ESC (AOESC)

ESC can be based on continuous time implementations of numerical optimization algorithms. Zhang et al. [32] report three approaches, namely Perturbation Based ESC (PESC), sliding-mode ESC (SMESC) and gradient feedback ESC (GESC).
PESC works under the assumption of time scale separation between the plant dynamics and the extremum seeking loop. The basic scheme presented by Kristic in Chapter 1 of [1] optimizes a static mapping by estimation of the relevant reference set-point. The scheme measures the output of the static mapping and applies a high pass filter to it. The resulting signal is unbiased. Then, the product with a sine wave is utilized to demodulate the gradient information. This piece of information is utilized by an integrator to steer the reference estimation towards the optimum. Finally, a sinusoidal perturbation (typically of small amplitude) is added to the estimated reference. The perturbation helps the demodulation, as stated in [1].
The scheme developed in Chapter 2 of [1] can handle slow output dynamics. In turn the high pass filter bandwidth is relatively low and the perturbation frequency should be set high enough. Instead the scheme presented in Chapter 5 assumes fast plant dynamics and relatively slow perturbation frequency. Kristic et al. [1] include stability proof both in the Single Input Single Output (SISO) as well as in the Multiple Input Multiple Output (MISO) case.
The shape of the perturbation signals mainly influence the method performance in terms of accuracy, speed and domain of convergence [26]. The dependency of PESC on the curvature of the objective function can be reduced by adding a Newton-like step [19].
PESC have been successfully applied to MPPT problems. Applications can be found for arrays of Photovoltaic converters (PVC) [18] or WECS in PLR. For example [17] deals with MPPT of an SRT by computing the rotor speed reference based on generator power measurement. The reference is then fed to a low level fast controller that produces the relevant inputs to the WECS. Other sources formulate a MISO problem to either maximize the power [10] or reduce fatigue loads [30]. Both sources generate torque and pitch angle references.
In SMESC a sinusoidal signal is utilized to generate the switching function that steers the controller towards the extremum. Instead, GESC is based on the knowledge of the gradient or its estimation. Guay et al. [11] developed a gradient-based ESC scheme with adaptive design. Guay et al. [12] applied their scheme to power optimization in WFs by computing the optimal axial induction factor. The power reference is computed assuming BEM theory and EWS knowledge.
To conclude, AOESC involves a continuous optimization process in contrast to iterative numerical optimization algorithms. The scheme requires continuous gradient information. As a matter of fact PESC and SMESC are more appealing than GESC because they do not require direct gradient measurement or estimation. AOESC is claimed to be model-free because the required knowledge of the model is limited and it is exploited

only during the design phase. Instead the scheme does not rely on the model, during operations.

2.2.1.2 Numerical Optimization Based Extremum Seeking Control (NOESC)

NOESC developed separately from AOESC. Compared to AOESC, NOESC does not require continuous gradient measurements. Instead, the system might have time to collect enough output samples that can be utilized to estimate the gradient.
A system model is needed to design a state regulator that allows to carry out the dynamic optimization. This however might not be the case if the plant is asymptotically stable.

2.3 Project Contribution

This project evaluates the effectiveness of Perturbation Based ESC (PESC) in addressing the SRTs coordination problem stated in Section 1.4. This thesis work addresses the first application of PESC to the MRT. In particular, the proposed ESC based architecture computes pitch references to each of the SRT in order to regulate the generator speed to 122.9 in rad/s in FLR. The generator power reference of each SRT is fixed to 5 MW instead. Therefore, the scheme satisfies the power requirement by achieving generator speed regulation.
Regarding the application of PESC to Wind Energy Capture System (WECS), there exist some applications [30], [10], [17], that solve a MPPT problem in PLR. However, this thesis represents the first attempt to utilize PESC to regulate the generator speed of a WECS in FLR.
Furthermore, the project investigates the impact of the sinusoidal perturbations and of the demodulation process on fatigue, by operating a spectral analysis of the pitch references, of the thrust forces and of the loads involved in the computation of fatigue. Two mitigation strategies are proposed and tested, in order to relieve the impact of structural fatigue. The first strategy involves the design of a low pass filter, that is included in the ESC loop. Instead, the second strategy requires a new formulation of the measured cost, which is expanded by adding terms that are correlated to fatigue.

CHAPTER 3

The Multi-rotor Wind Turbine

The first part of the chapter deals with the system description of the MRT. The analysis of the building subsystems and their interconnections provides more insights into the MRT working principle. The second part focuses on modelling, specifically of the SRTs and the support structure.

3.1 System Description

A multi-rotor wind turbine is a WECS that mounts more nacelles on the same support structure. The main structural element of the 4 rotor turbine utilized in [23] is the tower. Four arms are attached to the tower, one for each nacelle. The scheme in Figure 3.1 and Table 3.1 outline the configuration and the size of the 4 rotors turbine model utilized in the benchmark paper [23] and during the project.

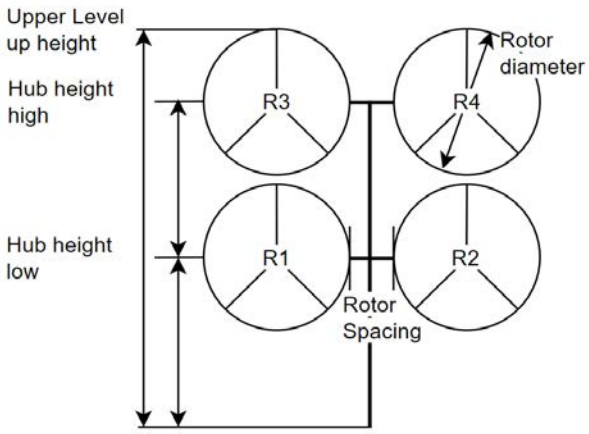

Figure 3.1: Schematic of the 4-rotors turbine, front view. The arms are positioned downwind, namely the wind stream encounters the rotors first and then, the arms of the support structure. Reproduced and adapted from [23].

The rotors are responsible for converting wind energy to mechanical torque. As it can be seen in Figure 3.2 the blades connect to the nacelle shaft through the hub.

The hub hosts the pitch actuator and the mechanism to change the pitch angle and thus the aerodynamic torque. The rotor turns slowly, typically around 20-50 in rpm

Rotor diameter	126 m
Rotor spacing	12.6 m
Hub height low	90 m
Hub height high	228.6 m
Upper level tip height	291.6 m

Table 3.1: Dimensions of the main subsystems labelled in Figure 3.1.

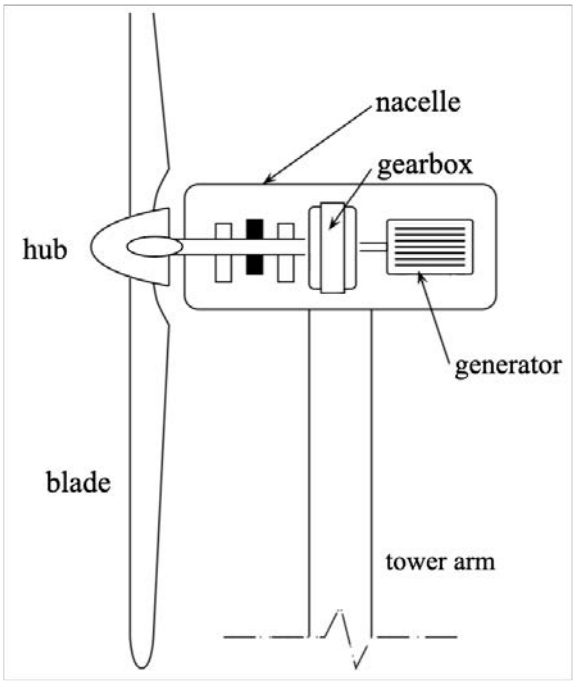

Figure 3.2: Top view of the SRT and of the subsystems involved in energy conversion. Figure adapted from [5], page 30.

[5]. The gearbox increases the rotor speed to values more suitable for the generator. The generator is the place where mechanical power is converted into electricity. The electric terminals of the generator are connected to the network. Details on the generator working principle are available in [5]. Each SRT is rated for 5 MW hence the 4 rotor turbine is capable of producing up to 20 MW.

3.1.1 Signal Routing and Subsystems Interconnection

The Simulink model of the MRT [2] provided with [23] includes four National Renewable Energy Laboratory (NREL) 5 MW SRT blocks. The diagram in Figure 3.3 represents the subsystems of the SRT model as well as the interconnection between them. In Figure 3.3 a lot of new symbols are defined, however it is always possible to access the list of Symbols at the very beginning of the report.

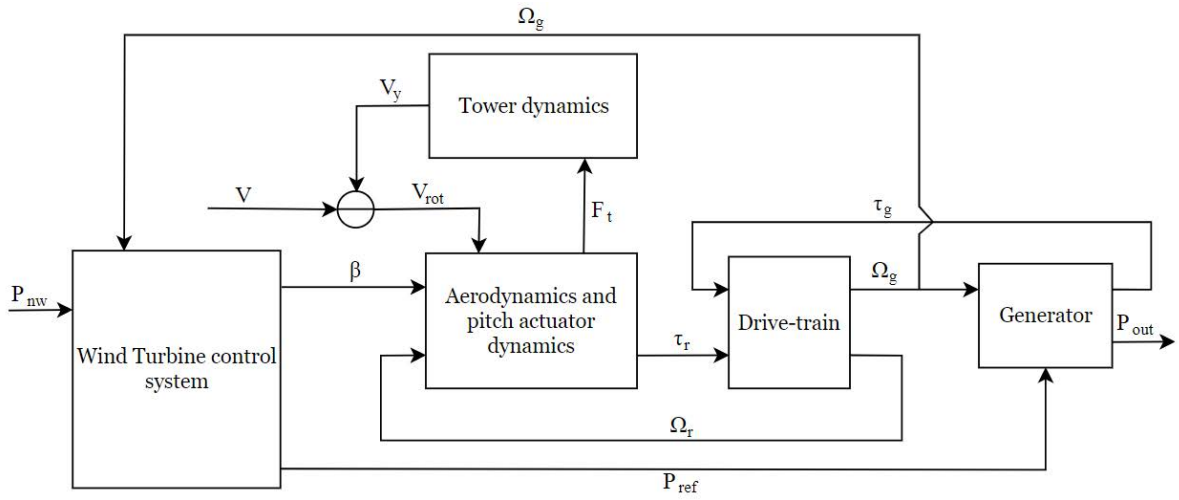

Figure 3.3: Schematic showing the signal routing and the interconnections between each SRT subsystem.

The Wind Turbine control system receives as input P_{nw}, which represents the power demand by the network and the generator angular speed Ω_g. The inputs are used to generate the power set-point P_{ref} to the generator and a pitch set-point β to the aerodynamics subsystem. The aerodynamic subsystem produces the rotor torque τ_r and the thrust force F_t as the combined action of three factors. First, the wind speed relative to the rotor blades V_{rot}. V_{rot} differs from the undisturbed wind speed V due to the nacelle coupling with the tower. In the model it is assumed that the coupling causes a fore-aft nacelle velocity V_y acting along the same direction as the wind. The second factor is the pitch angle β. Increasing the pitch angle reduces the blades angle of attack and, consequently, τ_r [5]. Finally, the rotor speed Ω_r plays an important role, too, as it influences the tip speed ratio λ.
The rotor speed and the generator speed are the outcome of the dynamic torque balance between the rotor side and the generator side in the drive-train. The drive-train includes the gearbox. The power output P_{out} is typically less than P_{ref} as it is scaled by the generator efficiency. Commercial generator solutions have efficiency that varies with the generator speed [29], however the model used here has constant efficiency.

3.2 Modelling

The models of the subsystems in Figure 3.3 have been developed as part of the Aeolus FP7 project [15]. Compared to the turbine model in [15], the tower dynamics has been replaced by the linear model of the MRT support structure developed in [23].

3.2.1 Aerodynamics and Pitch Actuator Dynamics

The rotor aerodynamics is described by means of two static relations

$$\tau_r = \frac{1}{2} V_{rot}^3 \rho A C_p(\lambda, \beta) \Omega_r^{-1} \tag{3.1}$$

$$F_t = \frac{1}{2} V_{rot}^2 \rho A C_t(\lambda, \beta) \tag{3.2}$$

C_p and C_t being the power and the thrust coefficient respectively, provided as look-up tables functions of the pitch angle β and the tip speed ratio $\lambda = \frac{R\Omega_r}{V_{rot}}$. ρ is the air density and A is the rotor disc area. More details are available in [5].
The pitch actuator dynamics is a second order system with time constant t_B and input delay d from input u_β to $\dot{\beta}$. A proportional controller with constant K_β controls the actuator.

$$\ddot{\beta} = \frac{1}{t_\beta}(u_\beta^d - \dot{\beta}) \tag{3.3}$$

$$u_\beta = K_\beta(\beta_{ref} - \beta_{meas}) \tag{3.4}$$

where $u_\beta^d(t) = u_\beta(t - d)$.

3.2.2 Drive-train

The drive-train is modelled as a third order system and it is based on two rotating shafts and a gearbox. The gearbox has torsional spring constant K_{shaft}, viscous friction B_{shaft} and a gear ratio N. We have, therefore, the three differential equations:

$$\dot{\Omega}_r = \frac{1}{I_r}\left(\tau_r - \phi K_{shaft} - \dot{\phi} B_{shaft}\right) \tag{3.5}$$

$$\dot{\Omega}_g = \frac{1}{I_g}\left(-\tau_g + \frac{1}{N}(\phi K_{shaft} - \dot{\phi} B_{shaft})\right) \tag{3.6}$$

$$\dot{\phi} = \Omega_r - \frac{1}{N}\Omega_g \tag{3.7}$$

where ϕ is the shaft torsion angle and I_g,I_r are the generator and rotor inertias, respectively.

3.2.3 Generator

The generator is modelled as a first order system with input P_{ref} and time constant t_g:

$$\dot{\tau}_g = \frac{1}{t_g}\left(\frac{P_{ref}}{\Omega_g} - \tau_g\right) \tag{3.8}$$

The output power P_{out} is obtained as follows

$$P_{out} = \epsilon_g \tau_g \Omega_g \tag{3.9}$$

where ϵ_g is the efficiency of the generator. The efficiency of the generator is assumed constant with respect to the generator speed. However, in real applications the efficiency of the generator speed varies with the shaft speed, with a direct impact on P_{out} [29]. Based on (3.8) a certain power reference P_{ref} can always be achieved as long as the generator speed is greater than zero.

3.2.4 Structural Model

The non-linear equations of motion of the support structure have been derived in the benchmark paper [23] using the Lagrange equations. The equations have been linearized around the equilibrium point of the support structure and then written in state space form. The model does not include gravitational loads, nor aerodynamic stiffening or damping from rotors. Blades are not included and arms are assumed to be very stiff. The inputs to the structure are 4 point thrust forces at the tip of each arm.
The model includes 10 degrees of freedom, whose physical meaning is explained in Figure 3.4.

3.2.5 SRT control strategy

The SRT baseline control strategy is Variable-Speed Variable-Pitch (VSVP) (pitch-to-feather). More details on other SRT control strategies are available in [5]. The Rotational Speed - Torque plan in Figure 3.5 represents the VSVP strategy.

$V_{min} = 2$ and $V_{max} = 20$ in m/s are the cut-in and cut-off wind speeds respectively. V_{Ω_N} is the wind speed at the rated generator speed Ω_N. In the AB range the available wind Power is less than the rated value and the system is said to operate in PLR. The pitch angle is kept at 0 degrees while varying the generator speed in order to maximize the energy capture. At point B the generator reaches its rated rotational speed Ω_N. The rated rotational speed is the upper limit on the generator speed. In the BC wind speed range the generator rotational speed is regulated at its rated value $\Omega_N = 122.9$ in rad/s, by acting only on the power electronics. C is reached when the wind speed equals its rated value, $V_N = 12.4$ in m/s. If V is greater than V_N, the pitch angle is regulated to keep performance at point C, where the produced power is at its rated value P_N and so is the generator speed. The system is now operating in FLR. In the industry [29], the generator speed is not tightly regulated at Ω_N. The aim is to avoid excessive control effort on the pitch actuator as well as to avoid increased fatigue on the support

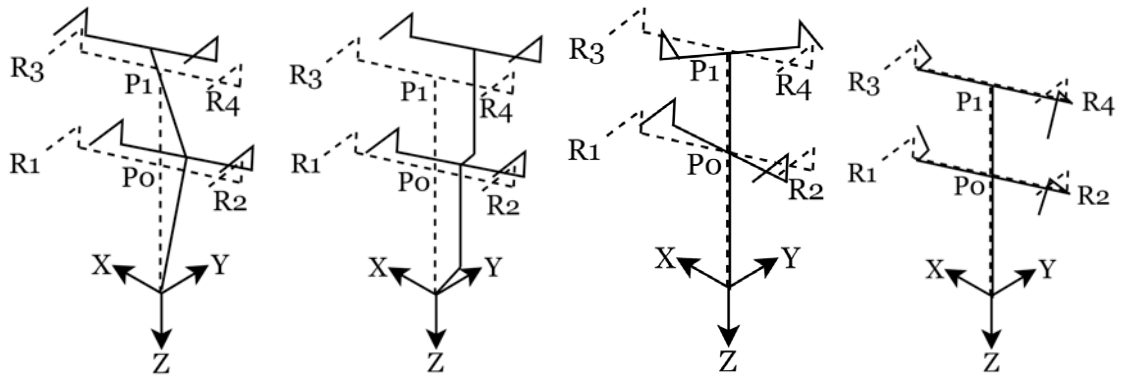

(a) Platforms fore-aft rotation (b) Platforms fore-aft translation (c) Platforms torsion (d) Arms torsion

Figure 3.4: The support structure is divided into two platforms, P0 and P1 respectively. (a) and (b) represent together the two tower sections fore-aft bending along the Y direction and include 4 Degree of Freedom (DOF). (c) shows that each platform can rotate around the Z axis. Two DOF are utilized. Finally, arm torsion is important because the thrust force is not applied directly to the center of the support arm but to a point with offset (d). 4 DOF are utilized.

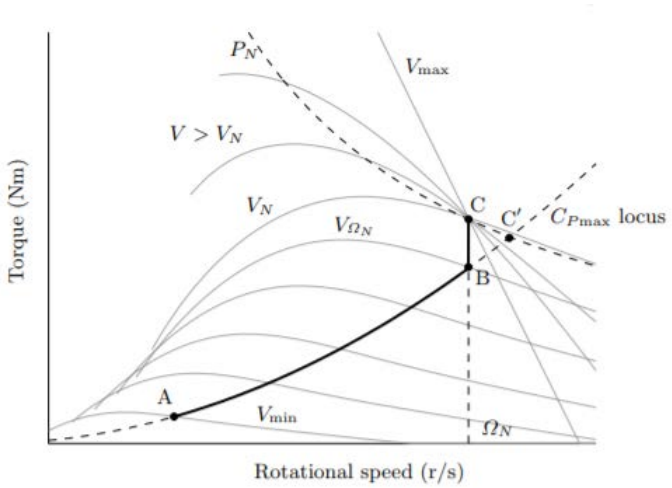

Figure 3.5: VSVP (pitch-to-feather) control strategy. Bianchi et al., page 69 courtesy [5].

structure.
Each SRT block in the Simulink model [2] implements VSVP as the baseline control strategy. Details on the implementation are available in [15]. The BMC control strategy developed in [23] feeds additive pitch signals to the baseline set-points of each SRT. The additive signals are computed based on fore-aft tower velocity and displacement

feedback and they are proven to be beneficial against fatigue. In particular, as stated in the benchmark paper [23], the scheme increases the dampening and the stiffness of the support structure.

3.3 Operative Assumptions

The following operating assumption will be used in the upcoming chapters:

- The Wind Turbine control system in Figure 3.3 is isolated by the remaining subsystems when the ESC is working.
- The new architecture produces pitch and power set-points that are fed to the pitch actuator and the generator of each SRT respectively.
- The generator and the pitch actuator can execute the provided set-points.
- The MRT is set up to operate in FLR.

CHAPTER 4

Extremum Seeking Control

This chapter presents ESC. The method is first introduced to the reader through an example from the textbook [1]. The example is meant to show that ESC computes reference set-points that optimize an unknown static mapping. The method relates to the SRT coordination problem from Section 1.3 because, as it will be shown later in the chapter, each SRT requires power and pitch set-points to be computed. In this project, ESC will compute the pitch set-points without relying on the knowledge of the MRT model during operations. The power reference will be fixed instead. The second part of the chapter introduces an ESC based architecture for the MRT, relying on the theory developed in [1]. Compared to the initial example, the new scheme is capable of dealing with a time varying optimum point in the mapping to be optimized and also to deal with plant dynamics. The added complexity is justified by the fact that the ESC has to operate the dynamics of each SRT under unknown wind conditions, where the pitch angle has to change in order to regulate the generator speed. Greater emphasis is put on the description of the subsystems of the ESC loops and of the relevant assumptions. The assumptions serve as the hypotheses of the local exponential convergence theorem. The theorem clarifies the design guidelines to be followed in order to achieve local exponential convergence of the scheme. Finally, the application of the design assumptions and guidelines to the proposed architecture allows to obtain a preliminary ESC design to achieve generator speed regulation.

4.1 Extremum Seeking for a Static Mapping

The example presented in the following relates to the steps in Section 1.1 from [1]. The diagram of the basic Perturbation Based ESC (PESC) is displayed in Figure 4.1. As stated in Section 2.2, the purpose of ESC is not to regulate a system to known set-points. In some applications the reference to output mapping has an *extremum*. The objective of ESC is to compute the optimal reference set-point θ^* that keeps the output y at the extremum f^*[1]. The exact expression of the static mapping $y = f(\theta)$ is unknown. However, the static mapping $f(\theta)$ is assumed to be $\mathcal{C}^2$. The Plant subsystem in Figure 4.1 includes the reference to the output mapping. As explained by Kristic in [1], the ESC scheme works also for plants with dynamics, even though the Plant in Figure 4.1 does not include any dynamics to keep the analysis simple.

[1]The notation $f^* := f(\theta^*)$ is utilized for brevity.

Despite the expression of $f(\theta)$ being unknown, yet it is possible to write the Taylor approximation of $f(\theta)$ in the neighbourhood of θ^*, as shown in (4.1).

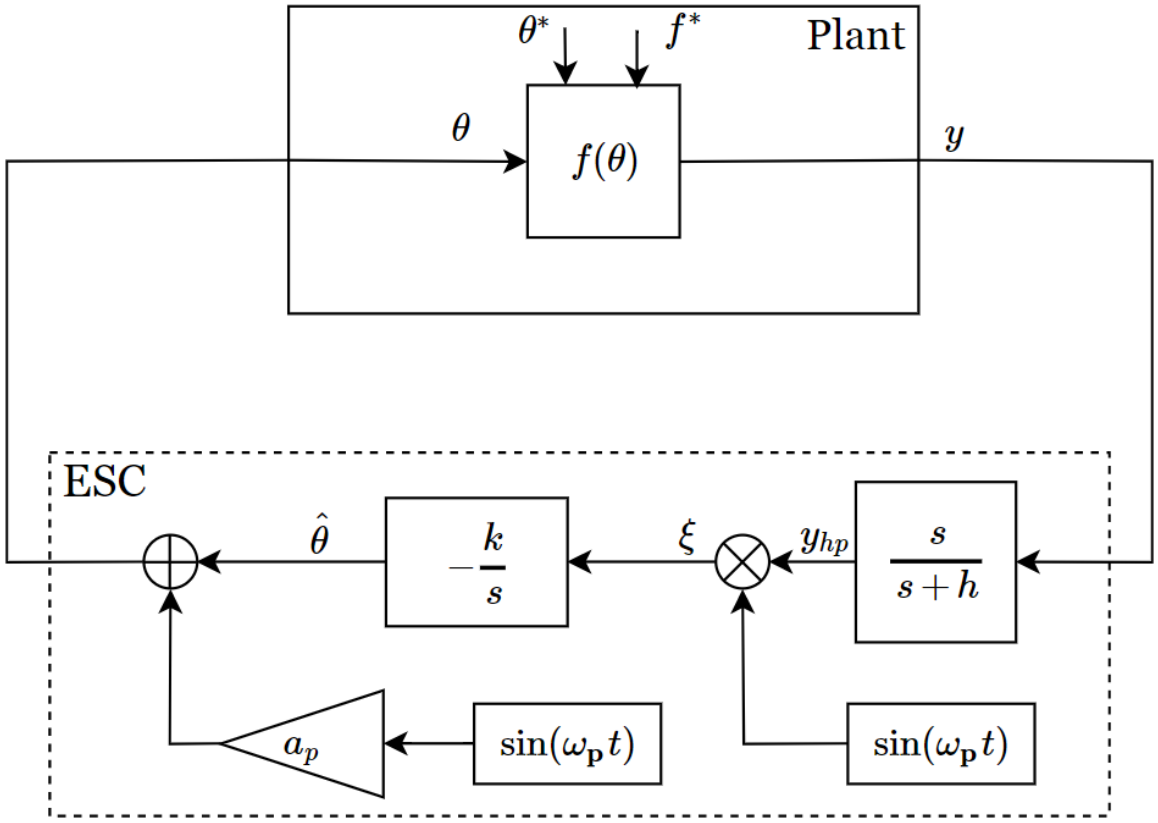

Figure 4.1: Basic extremum seeking scheme, reproduced from [1].

$$f(\theta) \approx f^* + \frac{f''}{2}(\theta - \theta^*)^2 \tag{4.1}$$

where[2] f'' is the second derivative of the mapping evaluated at θ^*. The goal of the ESC subsystem is to find the reference sequence $\theta(t)$ that minimizes the difference $\theta - \theta^*$ and keeps the measured output y at the extremum f^*. In (4.1) the extremum f^*, the second derivative f'' and the optimal reference θ^* are unknown. However, the sign of f'' is assumed to be known and it is either strictly positive or strictly negative. If $f'' > 0$ the ESC seeks a minimum. Instead, if $f'' < 0$ the scheme seeks a maximum. y is the measured output and the input to the ESC subsystem in Figure 4.1. The measured output y and the sign of f'' are the only two pieces of information required by the scheme to operate. The ESC scheme presented in Figure 4.1 is, in fact, a Perturbation

[2]The full notation should be $f''(\theta^*)$, however the notation $f'' := f''(\theta^*)$ is utilized for brevity.

Based ESC (PESC) because it applies sinusoidal signals to reconstruct missing gradient information. A PESC for a static mapping includes 4 main steps:

1. *Washout* filter (high pass filter). The purpose of the high pass filter applied to the measured output y is to highly attenuate the DC component and the bias of the signal.

2. *Demodulation.* Multiplying the output of the high pass filter by the sine wave allows to recover the information of the unknown gradient, as it will be shown later in this section.

3. Integrator. Based on the recovered gradient information, the integrator drives $\hat{\theta}$ in the direction where the gradient becomes smaller. k is the integrator gain, whose sign has to be the same as the sign of $f^{''}$ to ensure convergence of θ to a neighbourhood of θ^*, as it will be clarified in this section.

4. Additive perturbation. The additive sinusoidal perturbation is scaled by the gain a_p, typically small [1]. The additive perturbation propagates through the Plant subsystem and plays a crucial role in the demodulation phase, as it will be clarified further down.

The block diagram in Figure 4.1 is elaborated in the following. As stated by Kristic in [1], the analysis is meant to provide the reader with an intuitive interpretation of the steps outlined before.
The aim is to find the conditions which ensure that the reference signal θ converges to a neighbourhood of θ^*. Let $\hat{\theta}$ in Figure 4.1 be the estimate of the optimal input θ^* and

$$\tilde{\theta} = \theta^* - \hat{\theta} \tag{4.2}$$

the associated estimation error. Then, from the diagram it follows that

$$\theta - \theta^* = a_p \sin \omega_p t - \tilde{\theta} \tag{4.3}$$

The additive sinusoidal perturbation $a_p \sin \omega_p t$ propagates through the plant, here a static mapping, and it is present in the measured output y. By substituting (4.2) and (4.3) in (4.1), the output $y = f(\theta)$ is rewritten as follows

$$y = f^* + \frac{f''}{2}(\tilde{\theta} - a_p \sin \omega_p t)^2 \tag{4.4}$$

The expression is expanded and the trigonometric identity $2\sin^2 \omega_p t = 1 - \cos 2\omega_p t$ is applied

$$\begin{aligned} y &= f^* + \frac{f''}{2}\tilde{\theta}^2 - a_p f''\tilde{\theta}\sin\omega_p t + \frac{a_p^2 f''}{2}\sin^2\omega_p t \\ &= f^* + \frac{a_p^2 f''}{4} + \frac{f''}{2}\tilde{\theta}^2 - a_p f''\tilde{\theta}\sin\omega_p t + \frac{a_p^2 f''}{4}\cos 2\omega_p t. \end{aligned} \tag{4.5}$$

The additive perturbation combined with the Taylor approximation of $f(\theta)$ in the neighbourhood of θ^* produces, among the other things, the term $a_p f''\tilde{\theta}\sin\omega_p t$ that will be important during the *demodulation* phase.
When the output y enters the ESC subsystem, the *washout* filter, i.e. high pass filter, is applied to remove the bias introduced by f^* and $\frac{a_p^2 f''}{4}$. The resulting expression of the output of the high pass filter, y_{hp}, is shown in (4.6):

$$y_{hp} = (w * y)(t) \approx \frac{f''}{2}\tilde{\theta}^2 - a_p f''\tilde{\theta}\sin\omega_p t + \frac{a_p^2 f''}{4}\cos 2\omega_p t. \tag{4.6}$$

where w denotes the impulse response of the high pass filter and the symbol [*] indicates the operation of convolution. The *washout* filter removes the dependence of the signal on the unknown bias terms f^* and $\frac{a_p^2 f''}{4}$, that would appear as sinusoidal terms after the multiplication of y_{hp} by $\sin\omega_p t$. The multiplication step is called *demodulation* and it is meant to recover a DC component from y_{hp} that carries the gradient information. Any other sinusoidal component resulting from the *demodulation* does not support the recovery of the gradient information. The *demodulation* results in the following signal

$$\xi = y_{hp}\sin\omega_p t \approx \frac{f''}{2}\tilde{\theta}^2\sin\omega_p t - a_p f''\tilde{\theta}\sin^2\omega_p t + \frac{a_p^2 f''}{4}\cos 2\omega_p t\sin\omega_p t. \tag{4.7}$$

The *demodulation* effect is made clear with the application of the trigonometric identity $2\sin^2\omega_p t = 1 - \cos 2\omega_p t$ to the sinusoidal quadratic term in (4.7). The trigonometric identity splits $\sin^2\omega_p t$ in to the cosine term $\cos 2\omega_p t$ and the static component 1. The static component results in the term $-\frac{a_p f''}{2}\tilde{\theta}$ which is proportional to the estimation error and represents the recovered gradient information. This term will be crucial at the end of the analysis to show that the estimation error dynamics is stable. Furthermore, applying the identity

$$2\cos 2\omega_p t\sin\omega_p t = \sin 3\omega_p t - \sin\omega_p t$$

allows to rewrite ξ as the sum of trigonometric terms at ω_p, $2\omega_p$ and $3\omega_p$ and the term dependent on the estimation error. The new formulation of ξ will be useful in the following, when commenting on the effect of the integrator on the trigonometric terms.

$$\xi \approx -\frac{a_p f''}{2}\tilde{\theta} + \frac{a_p f''}{2}\tilde{\theta}\cos 2\omega_p t + \frac{a_p^2 f''}{8}(\sin\omega_p t - \sin 3\omega_p t) + \frac{f''}{2}\tilde{\theta}^2\sin\omega_p t \tag{4.8}$$

Since θ^* is constant by assumption because the mapping is static, it holds that

$$\dot{\tilde{\theta}} = -\dot{\hat{\theta}} \tag{4.9}$$

Considering the integrator in Figure 4.1, the following relation holds true

$$\dot{\hat{\theta}} = -k\xi \tag{4.10}$$

Or, combining (4.9) with (4.10), it follows that

$$\dot{\tilde{\theta}} = k\xi \tag{4.11}$$

The full expression of (4.11) is reported in the following. The new expression is an approximation of the estimation error derivative $\dot{\tilde{\theta}}$. Again, the aim is to show that, under the appropriate assumptions, the estimation error has a stable dynamics

$$\begin{aligned}\dot{\tilde{\theta}} \approx & k\left[-\frac{a_p f''}{2}\tilde{\theta} + \frac{a_p f''}{2}\tilde{\theta}\cos 2\omega_p t\right. \\ & \left. + \frac{a_p^2 f''}{8}(\sin\omega_p t - \sin 3\omega_p t) + \frac{f''}{2}\tilde{\theta}^2 \sin\omega_p t\right]\end{aligned} \tag{4.12}$$

At this point of the analysis, the author in [1] first neglects the quadratic term in $\tilde{\theta}$ because the analysis is local, leading to (4.13):

$$\dot{\tilde{\theta}} \approx k\left[-\frac{a_p f''}{2}\tilde{\theta} + \frac{a_p f''}{2}\tilde{\theta}\cos 2\omega_p t + \frac{a_p^2 f''}{8}(\sin\omega_p t - \sin 3\omega_p t)\right] \tag{4.13}$$

The meaning of rewriting (4.7) as (4.8) is clarified in the following. The author assumes that ω_p is chosen relatively large compared to the integrator gain k, the additive perturbation amplitude a_p, h and the second derivative of the static mapping f'' at the optimum. If ω_p is chosen large enough, then the last three terms in (4.13) are high frequency terms compared to the first term, thus they get highly attenuated when the integrator is applied. As a consequence of the attenuation, only the first term in (4.13) is left and the expression is simplified to the following

$$\dot{\tilde{\theta}} \approx -\frac{k a_p f''}{2}\tilde{\theta} \tag{4.14}$$

The dynamics of the estimation error in (4.14) is stable if the following conditions hold. Assuming that the perturbation amplitude a_p is positive, the dynamics of the estimation error in (4.14) is stable if and only if the product kf'' is positive, or equivalently k has the same sign as f''. The author in [1] concludes that the estimation error converges to a

neighbourhood of zero, i.e. $\hat{\theta}(t)$ converges to a ball containing θ^*. However, as reported in another paper [19], the convergence rate depends on the absolute value of f'', whose magnitude is unknown.

4.1.1 Numerical Example

The example presented in the previous Section has been implemented in Simulink, assuming the numerical values in Table 4.1 for the relevant parameters

θ^*	f^*	f''	h (rad/s)	ω_p (rad/s)	a_p	k
2	5	2	1	40	0.1	1

Table 4.1: Numerical values utilized in simulation.

Based on the parameters from Table 4.1, the static mapping (4.1) utilized in simulation is rewritten as follows

$$y = f(\theta) = 5 + 2(\theta - 2)^2 \tag{4.15}$$

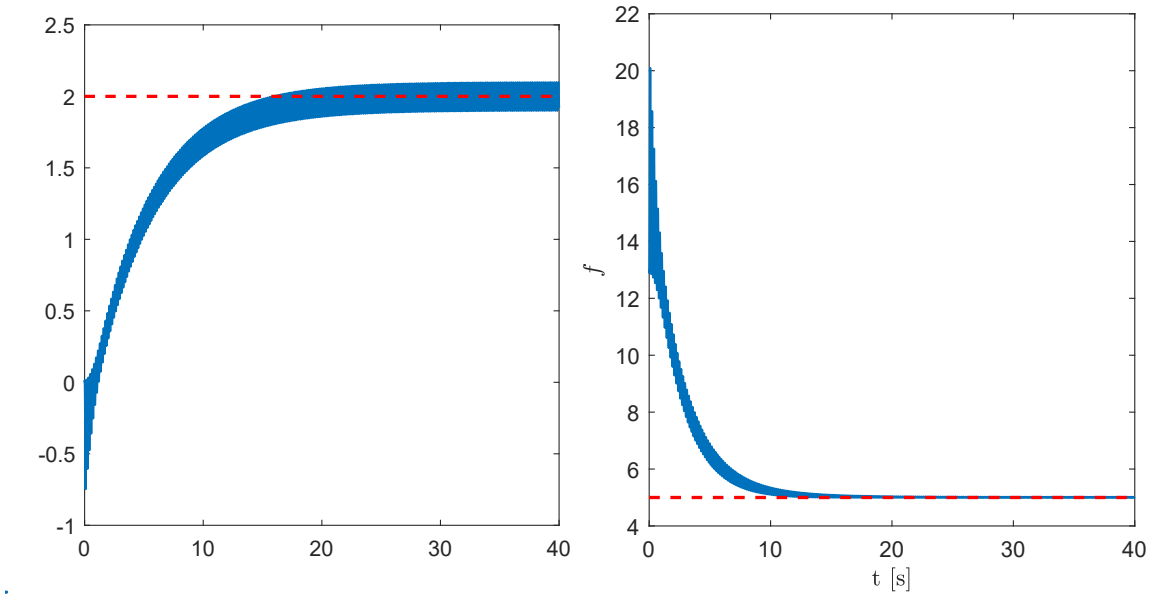

(a) Reference estimate (b) Measured output

Figure 4.2: Both θ and y (blue lines) converge in a neighbourhood of θ^* and f^* (red dashed lines), respectively. The box in (a) magnifies the oscillations of θ around θ^*.

Simulation results are plotted in Figure 4.2 (a) and (b). Despite being initialized to zero, θ settles to a neighbourhood of $\theta^* = 2$ in approximately 15 seconds. y also converges

towards $f^* = 5$, as expected. θ and y keep oscillating around θ^* and f^* due to the additive sinusoidal perturbation (dithering signal). As explained in the previous section, the additive perturbation is crucial during the *demodulation* phase and consequently to recover the gradient information.

The ESC has no knowledge about f^*, θ^* and f'', even though the parameters are included in Table 4.1. The values are utilized just to check that the estimation error actually converges to a small neighbourhood of θ^*. Noticeably, the perturbation frequency is an order of magnitude greater than the other parameters in the system. The results of the numerical example highlight the main strength of the method, i.e. PESC computes optimal reference set-points without assuming any knowledge of the static mapping $f(\theta)$, except for the sign of f''. As such, the performance of the method is virtually uncorrelated to the accuracy of the model of the Plant. As stated in the introduction to this chapter, this feature of ESC is relevant to address the coordination problem outlined in Section 1.3. In fact, the scheme can be utilized to generate the reference set-points to each SRT, without relying on the MRT model.

4.2 Introducing the Control Architecture

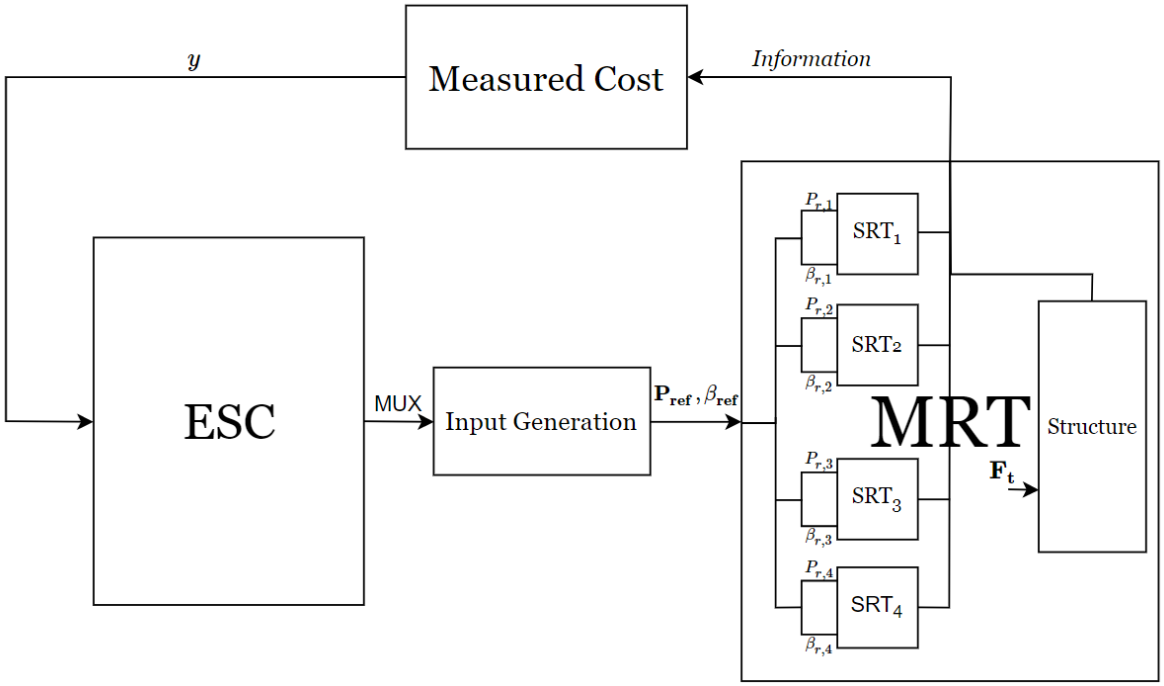

Figure 4.3: High level view of the ESC based control architecture.

The proposed architecture is depicted in Figure 4.3. It has been implemented in Simulink and it encompasses the existing MRT Simulink model [2]. Let us analyze each subsys-

tem moving counterclockwise, beginning from the MRT. More detailed views of the subsystems in Figure 4.3 are given in Figure 4.4.

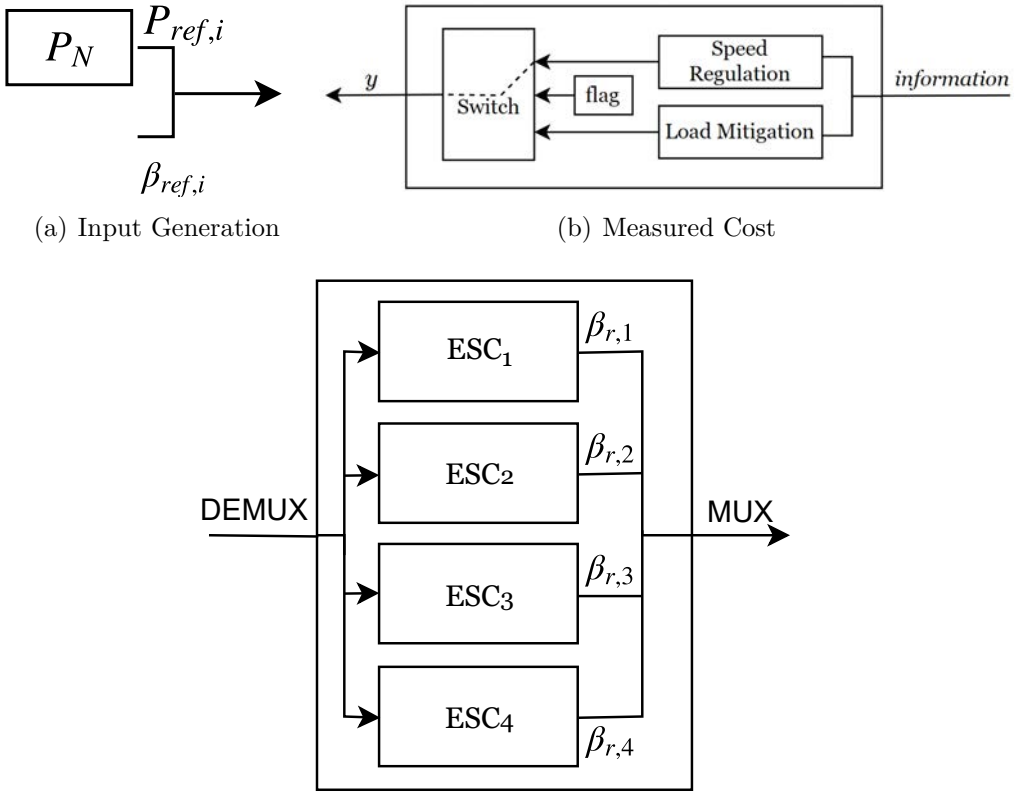

(a) Input Generation

(b) Measured Cost

(c) ESC

Figure 4.4: More detailed view of the relevant subsystems in Figure 4.3.

4.2.1 Measured Cost

As stated in Section 1.4, the designed ESC has to fulfil two objectives: the primary objective is the generator speed regulation, while the secondary is fatigue mitigation. The *Information* vector collects the measured signals that are utilized to define the measured cost. The subsystem in Figure 4.4 (b) includes two expressions for the measured cost, named Speed Regulation and Load Mitigation, respectively. The former is utilized when the aim of the optimization is exclusively generator speed regulation at each SRT. The latter is utilized when the aim of the optimization is both generator speed regulation and fatigue mitigation. The Speed Regulation measured cost will be utilized for simulations in Chapter 5. Instead, the Load Mitigation measured cost will be applied in Chapter 6. The Measured Cost subsystem in Figure 4.4 (b) has been implemented to be modular. Depending on the objectives of the optimization, it is always possible to switch between each of the two measured costs, before the beginning of each simulation, by acting on a flag.

4.2.2 ESC

In this project, the measured cost y is a vector of 4 local costs. The i-th cost is fed to the i-th ESC subsystem in Figure 4.4 (c), whose output is the i-th pitch reference $\beta_{r,i}$. Overall the proposed architecture is made by 4 SISO ESC loops, where the definition of SISO ESC is provided in [1]. Each ESC optimizes a local measured cost and there is no exchange of information between the loops.

In the early stage of the project it was considered to solve the SRTs coordination problem by means of MISO ESC [1]. In that scheme the measured cost y is a scalar that gathers information from all SRTs. The scalar cost is fed to each of the 4 ESC loops to compute the pitch references that optimize y. According to the author of [1], the tuning effort is lower for SISO ESC than for MISO ESC. In the early stage of the project attempts have been made to implement a MISO ESC. However, the effort needed to achieve the appropriate tuning parameters encouraged to search a solution to the SRTs coordination problem through the 4 SISO ESC. The current and the following chapters focus on the design and the evaluation of the 4 SISO ESC. It is relevant to assess whether it is possible to achieve generator speed regulation and fatigue mitigation even when applying a scheme where there is no shared information among the ESC loops.

Earlier in this section, it was stated that each ESC outputs a pitch reference. Looking at the MRT subsystem in Figure 4.3, each SRT requires two references, the generator power $P_{r,i}$ and the pitch reference $\beta_{r,i}$. If the ESC was meant to produce all eight references, eight ESC loops would have been necessary. However, the scheme is meant to operate the MRT in FLR as stated in Section 3.3. In this wind speed range, the pitch reference has a major impact on the regulation of the generator speed [29], [5]. By changing the pitch references, it is also possible to affect the thrust forces $F_{t,i}$ and with them, the structural loads [29]. Instead the generator power reference is usually fixed to the rated P_N, because it does not have a strong impact on speed regulation in FLR [29], [5]. The same approach is investigated in this project, i.e. the ESC loops output only the pitch references. Because the power reference is fixed, the scheme might compromise speed regulation to achieve fatigue mitigation [29]. As a matter of fact, the generator might operate in a range of rotational speed where its efficiency is lower than the rated one [29]. Thus, despite the power being fixed to P_N, there might be sensible power loss in real applications [29]. However, the generator model utilized in the simulator [2] has a constant efficiency, hence the power loss due to variable generator efficiency can not be appreciated.

4.2.3 Input Generation

The Input Generation subsystem acts as a multiplexer between the pitch references produced by the ESC loops and the constant power references. From an implementation perspective, this subsystem helps to keep the diagram neat. The references are distributed to the different SRTs in the MRT subsystem.

4.3 Theoretical Background on SISO PESC

The aim of this section is to describe more in details the subsystems of each SISO ESC loop. With respect to Figure 4.3, the i-th ESC loop includes the following elements:

- the i-th measured cost y_i,
- the i-th ESC subsystem in Figure 4.4 (c) whose output is $\beta_{r,i}$,
- the i-th SRT within the MRT subsystem in Figure 4.3.

As stated earlier in Section 4.1, the ESC block diagram presented in Figure 4.1 works for a static plant where no dynamics affects the loop. However, the ESC loops of the MRT have to deal with the dynamics of the SRTs. For instance, the dynamics of the pitch servo (Section 3.2.1) influences the actuation of the pitch reference. Furthermore, the dynamics of the drive-train (Section 3.2.2) impacts the time it takes for a change in the pitch reference to produce the desired change in the generator speed. As a matter of fact, it is clear that the scheme presented in Section 4.1 does not respond to the challenges introduced by the MRT system, hence it needs to be upgraded. In particular, the design of the ESC subsystems in Figure 4.4 (c), should take into consideration the fact that plant dynamics is included in the loop. However, as stated by the authors in [1], this does not mean assuming that the system model during operations is known. Instead, the approximate knowledge of the plant dynamics is meant to be used during the design of the ESC. A possible updated version of the scheme analyzed in Section 4.1 is presented by Kristic in Section 1.2 of [1]. This source is taken as reference to develop the discussion about ESC in the remaining part of the chapter.

The scheme utilized in the following is reported in Figure 4.5. The Plant subsystem consists by three elements, i.e. the relevant SRT dynamics $F_i(s)$ and $F_o(s)$ expressed as rational transfer functions, and the unknown mapping $f(\theta)$. In the centre, there is the mapping $f(\theta)$. As clarified in the following, the mapping has time varying f^* and θ^*. This is already a clear difference compared to the scheme in Section 4.1 where f^* and θ^* were assumed constant. The input to the mapping θ is the result of applying the input dynamics $F_i(s)$ to the reference set-point computed by the ESC subsystem $\hat{\theta}$. Instead, to obtain the measured output y, the output dynamics $F_o(s)$ is applied to the output of the mapping $y_{f(\theta)}$. The assumptions made by the authors in [1] with respect to the expected time variations of f^* and θ^* and with respect to the plant dynamics are reported in Section 4.3.2 and Section 4.3.3, respectively. A qualitative description of the unknown mapping $f(\theta)$ is provided in Section 4.3.2. The same section also clarifies which signal is utilized as measured output y to address each of the objectives outlined in Section 4.2.
Additive noise n could possibly affect the measured output y. However, following the assumption in Section 1.2 of [1], measurement noise is neglected. The measured output is fed as input to the ESC subsystem. Each of the four ESC in Figure 4.4 (c) could be

expanded as the ESC subsystem in Figure 4.5. The ESC for plants with dynamics works similarly to the ESC for a static mapping, although there are some differences that are clarified in Section 4.3.1.

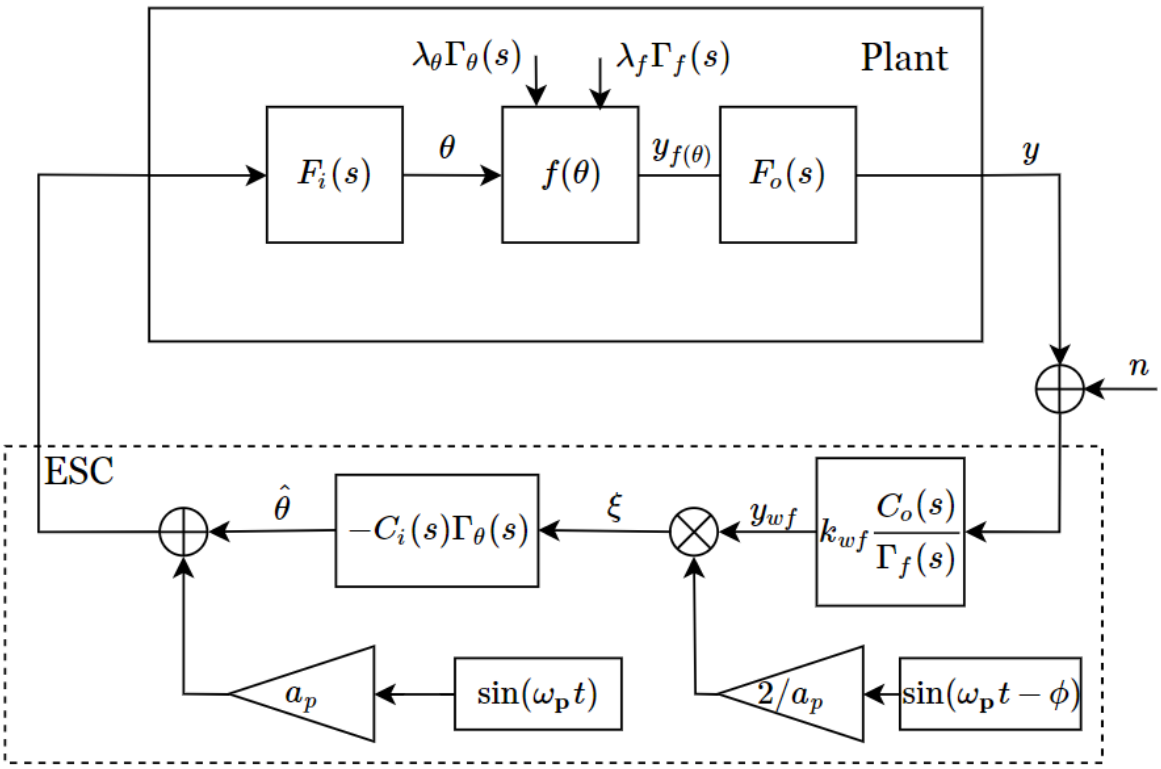

Figure 4.5: The figure shows the block diagram of SISO PESC according to [1] with a small change. In the original version the demodulation sine has unitary gain. Similarly to [19], the version presented here scales the sine wave by $2/a_p$ instead, a_p being the gain of the dithering signal. Reproduced and adapted from [1].

4.3.1 Introducing the ESC Subsystem

Recalling the 4 steps enumerated in Section 4.1, the measured output y is fed to the *washout* filter, first, whose transfer function is:

$$WF(s) = k_{wf}\frac{C_o(s)}{\Gamma_f(s)} \tag{4.16}$$

where k_{wf} is the gain of the filter, $C_o(s)$ is referred to by the author in [1] as output compensator. The design guidelines regarding $C_o(s)$ are defined in Section 4.4.6. Finally,

$\Gamma_f(s)$ is the shape of the transfer function that captures the expected variations of f^* over time. For instance, if step variations are expected in f^*, $\Gamma_f(s)$ would be set equal to $\frac{1}{s}$. More details about $\Gamma_f(s)$ are available in Section 4.3.3. $WF(s)$ is assumed to be proper, which ensures that the filter is implementable. The purpose of the *washout* filter is the same as in the case of a static mapping, i.e. highly attenuating the DC component and the bias of the signal. The output of the *washout* filter y_{wf} is multiplied by the sine wave

$$DM(t) = \frac{2}{a_p} \sin(\omega_p t - \phi) \tag{4.17}$$

where ω_p is the perturbation frequency, ϕ is phase of $DM(t)$ and a_p is the amplitude of the perturbation frequency. This step is called *demodulation* and it works qualitatively in the same fashion as explained in Section 4.1. As shown already in Section 4.1, the effectiveness of the *demodulation* depends on the additive sinusoidal perturbation in Figure 4.5. The signal

$$D(t) = a_p \sin(\omega_p t) \tag{4.18}$$

is also called dithering signal and it propagates through the plant together with the estimated reference signal $\hat{\theta}$. Differently from Section 4.1, the propagation through the plant does not only change the amplitude of $D(t)$ and introduce some other oscillatory terms, but also modifies the phase of $D(t)$. The phase shift is due to the effect of the input and output dynamics. The aim of the *demodulation* is to recover the amplitude change in $D(t)$ because it carries information about the partial derivative of the mapping $f(\theta)$ with respect to the reference set-point θ. The smaller the phase shift between $DM(t)$ and the dithering signal (after propagation through the plant), the higher the performance of the *demodulation*. Hence, ϕ should be chosen to minimize such a phase shift. The information regarding the amplitude change in $D(t)$ is utilized by the estimation algorithm to steer the estimated reference $\hat{\theta}$ towards the direction that reduces the partial derivative of $f(\theta)$ with respect to θ. The estimation algorithm generalizes the integrator in Figure 4.1 to plants with dynamics. The estimation algorithm has the following expression

$$EA(s) = C_i(s)\Gamma_\theta(s) \tag{4.19}$$

where $C_i(s)$ is called input compensator by the author in [1]. The design guidelines regarding $C_i(s)$ are described in Section 4.4.7. Instead, $\Gamma_\theta(s)$ is the shape of the transfer function that captures the expected variations of θ^* over time. As before, if step variations are expected in θ^*, then $\Gamma_\theta(s)$ would be set equal to $\frac{1}{s}$. More details about $\Gamma_\theta(s)$ are available in Section 4.3.3. $EA(s)$ is assumed to be proper, which ensures that the filter is implementable.
Section 4.3.2 focuses on the description of the mapping $f(\theta)$ and on the choice of the

measured cost y. Given the fact that the mapping is unknown by assumption, the description will focus on which input θ should be provided to $f(\theta)$ and on which signal $y_{f(\theta)}$, θ is mapped to. Finally, the choice of each of the measured costs is motivated by the objectives to be fulfilled.

4.3.2 Introducing the Unknown mapping and the Measured Cost

In this section the unknown mapping is described for each of the optimization objectives outlined in Section 4.2. Regarding the first objective, the aim of each ESC loop is to generate the adequate pitch reference that regulates the generator speed to its rated speed Ω_N, under unknown wind conditions. A graphic representation of the unknown mapping is provided in Figure 4.6. The input to the mapping is a pitch reference β. The reference is converted to the generator speed Ω_g. Ideally, if the pitch reference estimated by the ESC would be the optimal pitch reference β^* at that time instant, the generator speed would be mapped to its rated value Ω_N. The instantaneous optimal β^* is a function g of the current wind speed V, which is unknown. The quality of the regulation will depend on how well the ESC can track the variations in β^*.

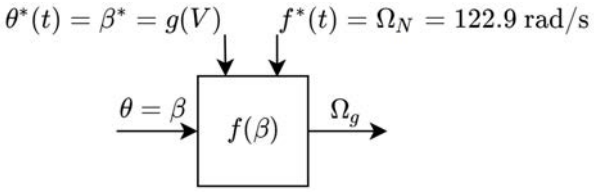

Figure 4.6: Graphic representation of the unknown mapping when the optimization objective is the generator speed regulation. The variations in the wind speed cause the optimal pitch reference β^* to change over time. Instead, the optimal f^* remains constant at $\Omega_N = 122.9$ in rad/s. Detailed view reproduced and adapted from [1].

At this point, it is possible to describe the unknown mapping $f(\theta)$ when the optimization goals are generator speed regulation and fatigue mitigation. As it can be seen in Figure 4.7, the input to the mapping is once again a pitch reference. The pitch reference tracks an unknown variation in β^* due to the combined effect of wind changes V and fatigue F. It is expected that the optimal generator speed Ω_g^* also changes over time to mitigate fatigue.

Both the unknown maps fulfil the following assumptions, as stated by the author of [1].

Assumption 4.1 The scheme does not require the exact knowledge of the mapping $f(\theta)$. However, the mapping is $\mathcal{C}^2$ with respect to θ.

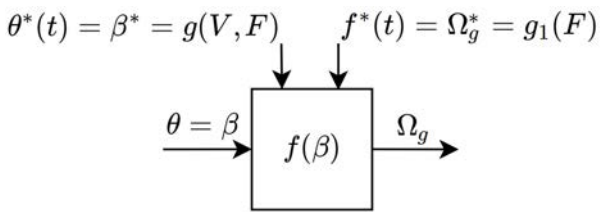

Figure 4.7: Graphic representation of the unknown mapping when the optimization objectives are generator speed regulation and fatigue mitigation. Wind speed changes and fatigue cause the optimal pitch reference β^* to change over time. f^* is also changing over time due to fatigue. Detailed view reproduced and adapted from [1].

Assumption 4.2 The sign of the second derivative f'' is known and determines whether the extremum is a minimum or a maximum.

ESC works in a neighbourhood of θ^*. Assumption 4.1 ensures that the Taylor approximation up to the second derivative exists in a neighbourhood of the extremum. In the following, it is assumed that $f'' > 0$, i.e. the scheme solves a minimization problem. Section 4.3.2.1 and Section 4.3.2.2 introduce the proposed measured costs to achieve the optimization objectives described in Section 4.2.

4.3.2.1 Speed Regulation ESC

In this case the objective of the ESC is exclusively the generator speed regulation. Hence, the measured output should provide a quantitative estimation of the quality of the generator speed regulation. The measured cost y_i in (4.20) is proposed to measure the quality of the generator speed regulation at SRT i:

$$y_i = (\Omega_{g,i} - \Omega_N)^2 \quad i = 1, ..., \ 4 \tag{4.20}$$

where $\Omega_{g,i}$ is the measured generator speed at SRT i and $\Omega_N = 122.9$ in rad/s is the rated generator speed. The measured cost is the square of the generator speed regulation error. The reason for squaring the regulation error is to ensure that the measured cost is continuously differentiable with a global minimum at $\Omega_{g,i} = \Omega_N$. The i-th ESC loop would then compute the reference pitch set-points to minimize the square of the measured generator speed regulation error.

4.3.2.2 Speed Regulation & Fatigue Mitigation ESC

When the optimization objectives are generator speed regulation and fatigue mitigation, the measured cost has to be adapted to include a term that quantifies fatigue. The proposed formulation of the measured cost is showed in (4.21):

$$y_i = y_{gr,i} + y_{fm,i} \tag{4.21}$$

$$y_{gr,i} = \frac{W_i}{\sigma^2_{\Omega_g}}(\Omega_{g,i} - \Omega_N)^2 \tag{4.22}$$

$$y_{fm,i} = \frac{1 - W_i}{\sigma^2_{F_i}} F_i^2 \quad i = 1, ..., \ 4 \tag{4.23}$$

The i-th measured cost consists of two terms, i.e. $y_{gr,i}$ and $y_{fm,i}$. The former deals with the first objective, i.e. generator speed regulation. The latter deals with the second objective, i.e. fatigue mitigation. W_i is a weight such that $W_i \in [0, 1]$. The gain allows the trade-off between fatigue mitigation and generator speed regulation. $W_i = 1$ means no fatigue mitigation at all. $y_{gr,i}$ is scaled by the variance of the generator speed, $\sigma^2_{\Omega_g}$. F_i is the description of fatigue at the i-th SRT. The expression of the fatigue term is defined later in Chapter 6. $y_{fm,i}$ is also scaled by its variance, $\sigma^2_{F_i}$. The variances $\sigma^2_{\Omega_g}$ and $\sigma^2_{F_i}$ are estimated in simulation and they are meant to normalize the cost to 1. Furthermore, the normalization makes the size of $y_{gr,i}$ and $y_{fm,i}$ comparable. The i-th ESC loop would then compute the reference set-point that minimizes the cost, which represents a compromise between the two objectives. The lower W_i the less relevant is the effect of $y_{gr,i}$ on y_i. As a matter of fact, reducing W_i is expected to worsen generator speed regulation. Actually this behaviour will be confirmed by simulation in Chapter 6.

4.3.3 Input and Output of the Unknown Mapping

As anticipated in Section 4.3.1, the unknown mapping $f(\theta)$ has time-varying f^* and θ^*. The author of [1] associates to each of the expected time variations of f^* and θ^* a transfer function as shown in the following.

$$\mathcal{L}(\theta^*) = \lambda_\theta \cdot \Gamma_\theta(s) \tag{4.24}$$

$$\mathcal{L}(f^*) = \lambda_f \cdot \Gamma_f(s) \tag{4.25}$$

where λ_θ and λ_f are unknown gains. Instead, $\Gamma_\theta(s)$ and $\Gamma_f(s)$ are the shapes of the transfer functions of θ^* and f^*, respectively. For instance, if step changes occur in f^* and θ^* the shape of both transfer functions is $\frac{1}{s}$. The author of [1] makes the following assumption on $\Gamma_\theta(s)$ and $\Gamma_f(s)$.

Assumption 4.3 $\Gamma_f(s)$ and $\Gamma_\theta(s)$ are known, strictly proper and rational transfer functions. Moreover unstable poles of Γ_θ are not zeros of $F_i(s)$.

By Assumption 4.3 the qualitative shape of the transfer functions is known. Instead λ_f and λ_θ are unknown. f^* is expected to be constant if the optimization pursues only

speed regulation because the speed reference is fixed at Ω_N. Instead, step changes of f^* are expected when fatigue mitigation is also considered. θ^* is expected to respond to unknown wind speed variations, hence it is reasonable to assume step changes in the pitch angle, i.e. $\Gamma_{\theta,f}(s) = \frac{1}{s}$.

4.3.4 Input and Output Dynamics

As it will be clarified in Section 4.4.6 and Section 4.4.7, the input and the output dynamics, $F_i(s)$ and $F_o(s)$ respectively, have a direct impact on the input and output compensators design. The author of [1] clarifies that the design steps require only an approximate knowledge of the plant dynamics. He also states that the expression of the plant dynamics could be obtained through step experiments. The following assumption holds regarding the plant dynamics.

Assumption 4.4 The input dynamics $F_i(s)$ and output dynamics $F_o(s)$ are assumed to be BIBO stable and proper transfer functions.

Following the reasoning in Section 4.3.2, $F_o(s)$ should be the transfer function from the generator speed Ω_g, as output of the mapping $f(\beta)$, to the measured cost y_i. However, it is not easy to measure the output of the unknown map. Instead, it is more convenient to merge the mapping with the output dynamics and to compute $F_o(s)$ as the transfer function from the i-th pitch angle to y_i. Due to the drive train dynamics, a set-point change in the pitch angle does not produce instantaneous changes in the measured cost. $F_o(s)$ is estimated by means of step experiments on one nacelle while the others are turned off. Each experiment is run at a fixed wind speed in the interval 14 to 20 m/s to cover the whole FLR. The power is kept at P_N and β is initialized at the angle needed to keep the generator speed at its rated value. Introducing ± 1 deg steps in the pitch angle causes the generator speed to settle at new steady state values. The measured cost follows approximately the behaviour of a first order system. The average response among all experiments is

$$F_o(s) = \frac{121}{7s + 1} \tag{4.26}$$

In the provided Simulink model [2], the blocks of the SRTs are identical to each other, hence the same output dynamics is assumed in each of the ESC loops. This assumption might have a positive impact on the tuning effort because it increases the degree of similarity between the ESC loops. Instead $F_i(s)$ is the dynamics of the pitch actuator. As stated in Section 3.2.1 the pitch actuator is a second order system, whose dynamics can be approximated as follows

$$F_i(s) = \frac{200}{s^2 + 2 \cdot \frac{\sqrt{2}}{2} 14.142 s + 200} \tag{4.27}$$

The parameters are obtained directly from the simulator [2]. For design purposes it is relevant to compute the time constants of the plant dynamics. The task is trivial in the case of $F_o(s)$ because it is a first order system. Instead $F_i(s)$ is an underdamped second order system. As such, the system does not have a time constant. However, the rise time of the step response of (4.27) can be utilized to approximate the time constant of an *equivalent* first order system. An approximation of the system in (4.27) is given by

$$F_i(s) \approx \frac{1}{0.13s + 1} \tag{4.28}$$

Even if it does not account for the 4 % overshoot in (4.27) step response, yet (4.28) captures the most relevant dynamics of the pitch actuator as shown in Figure 4.8.

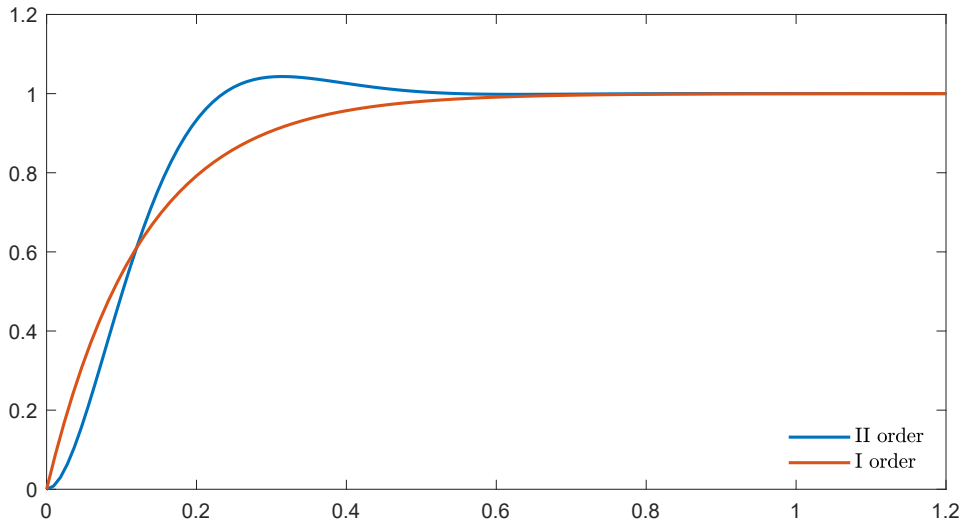

Figure 4.8: Step response of (4.27) in blue and (4.28) in red. The red response capture the most relevant dynamics..

As in the case of $F_o(s)$, also $F_i(s)$ is kept the same for every SRT, provided that in the Simulink model [2] the SRTs block diagrams are all equal. The selection of both $F_i(s)$ and $F_o(s)$ does not violate Assumption 4.4. The resulting plant is displayed in Figure 4.9. The following sections deal with the design steps of PESC for generator speed regulation.

4.4 PESC Design for Speed Regulation

This section opens with the Local Exponential Convergence Theorem, the design tool developed by the author of [1]. The results of the theorem will be extensively utilized in this section to achieve a preliminary ESC design for generator speed regulation.

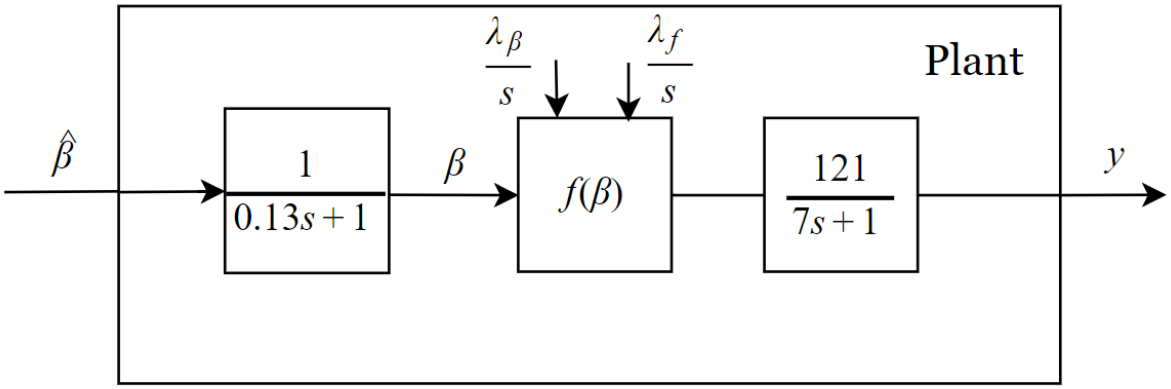

Figure 4.9: Detailed view of the Plant subsystem after every block has been defined. $\hat{\beta}$ is the ESC pitch angle before entering $F_i(s)$. The particular view of Figure 4.5 is adapted from [1].

4.4.1 Local Exponential Convergence Theorem

Theorem 1.8 from [1] ensures local exponential convergence of the output error $\tilde{y} = y - f^*$ in Figure 4.5. The proof is available in [1]. The theorem is quoted from the source textbook [1] in the following.

Theorem For the system in Figure 4.5, under Assumptions 4.1 to 4.6, the output error $\tilde{y}$ achieves local exponential convergence to an $\mathcal{O}(a_p^2 + \delta^2)$ neighbourhood of the origin, where $\delta = 1/\omega_p + 1/M$, provided that $n = 0$ and:

1. Perturbation frequency ω_p is sufficiently large, and $\pm j\omega_p$ is not a zero of $F_i(s)$.
2. Unstable zeros of $\Gamma_f(s)$ are also zeros of $C_o(s)$.
3. Unstable poles of $\Gamma_\theta(s)$ are not zeros of $C_i(s)$.
4. $C_o(s)$ and $\frac{1}{1+L(s)}$ are BIBO stable where

$$L(s) = \frac{a_p f''}{4} \mathrm{Re}\{e^{j\phi} F_i(j\omega_p)\} H_i(s) \tag{4.29}$$

Conditions 1 to 4 define design guidelines and steps to obtain local exponential convergence. Considerations about a_p are left out of the theorem. Later in the chapter, the author from [1] suggests to choose a_p so as to obtain a small steady state output error $\tilde{y}$. Exponential convergence is local, meaning that the system has to be initialized close enough to the origin $\tilde{y} = 0$.

4.4.2 Design Assumptions

In Section 4.3 some assumptions were made regarding the plant dynamics, the unknown mapping input and output and the measured cost. However, those assumptions are not sufficient to meet the hypotheses of the local exponential convergence theorem in Section 4.4.1. The missing assumptions, defined in [1], are restated here and their meaning is explained. The following notation is introduced to simplify the statement of the first assumption

$$H_o(s) = k_{wf}\frac{C_o(s)}{\Gamma_f(s)}F_o(s) = k_{wf}C_o(s)\frac{F_o(s)}{\Gamma_f(s)} = H_{o,sp}H_{o,bp} \tag{4.30}$$

where $H_{o,sp}(s) = k_{wf}C_o(s)$ is the strictly proper part of $H_o(s)$ and $H_{o,bp}(s) = \frac{F_o(s)}{\Gamma_f(s)}$ is the biproper part of $H_o(s)$. The output compensator $C_o(s)$ is one of the outputs of the design procedure. The design of $C_o(s)$ is meant to separate the slow output dynamics $F_o(s)$ from the fast dynamics in the ESC loop, in order to use a singular perturbation reduction of the output dynamics [1]. The following assumption provides qualitative conditions that allow to apply the singular perturbation reduction.

Assumption 4.5 Let $a.$ denote the smallest in absolute value among the real parts of all the poles of $H_{o,sp}(s)$ and let b, denote the largest among the moduli of all the poles of $F_i(s)$ and $H_{o,bp}(s)$. The ratio $M = a/b$ is sufficiently large.

In the case of strictly proper $F_o(s)$ with slow poles, *introducing a biproper* $\frac{C_o(s)}{\Gamma_f(s)}$ *with an equal number of fast poles* to the number of slow poles of $F_o(s)$, helps fulfilling Assumption 4.5. The second assumption is stated below.

Assumption 4.6 The transfer function

$$H_i(s) \triangleq C_i(s)\Gamma_\theta(s)F_i(s) \tag{4.31}$$

$H_i(s)$ is strictly proper.

Assumption 4.6 is made in [1] to simplify the proof of the theorem in Section 4.4.1. However, it would be possible to prove the theorem even without Assumption 4.6, as stated in [1].

4.4.3 Preliminary Design

In this section a preliminary design to achieve generator speed regulation is developed, following the steps in Section 4.4.1. Each step also fulfils Assumption 4.5 and 4.6.

4.4.4 Perturbation Frequency

Condition 1 in Section 4.4.1 does not specify how large ω_p can be chosen. As a general rule, the author in [1] suggests to pick ω_p much larger than other ESC and plant parameters. Further in [1] it is stated that, in fact, it might be possible to choose ω_p only slightly greater than the plant time constants. In the case of the MRT the plant time constants are respectively $\tau_i = 0.13$ for $F_i(s)$ and $\tau_o = 7$ for $F_o(s)$. The lower bound on ω_p is set to 7 rad/s. $\omega_p = 7$ rad/s would be much greater than $\omega_o = 1/\tau_o = 0.14$ rad/s but smaller than $\omega_i = 1/\tau_i = 7.7$ rad/s. Then ω_p is increased to 8.5 rad/s, slightly greater than ω_i. The perturbation frequency is the same for every SRT. In this early stage the phase shift ϕ is kept equal to zero.

4.4.5 Perturbation Amplitude

When it comes to the perturbation amplitude, there are no precise design guidelines in the textbook [1]. The only suggestion in [1] is to choose a_p large enough, such that it affects the estimated reference set-point. a_p has been fixed to 0.2 for every SRT in this preliminary phase. If necessary, the value will be adjusted during the tuning phase in Chapter 5.

4.4.6 Output Compesator

The design of the Output Compensator $C_o(s)$ is made according to Assumption 4.5 and Condition 1 in Section 4.4.1.
$H_o(s)$ can be rewritten as follows

$$H_o(s) = k_{wf}\frac{C_o(s)}{\Gamma_f(s)}F_o(s) = k_{wf}C_o(s)\frac{121s}{7s+1} \tag{4.32}$$

where the biproper part of $H_o(s)$ is

$$H_{o,bp}(s) = \frac{121s}{7s+1} \tag{4.33}$$

The largest pole of $F_i(s)$ is 7.7 rad/s and the largest pole of $H_{o,bp}(s)$ is 0.14 rad/s. According to Assumption 4.5, b should be chosen as the pole of $F_i(s)$, i.e. b = 7.7. The strictly proper part of H_o instead is

$$H_{o,sp}(s) = k_{wf}C_o(s) \tag{4.34}$$

meaning that $C_o(s)$ is strictly proper. Since the demodulation signal is multiplied by the gain $2/a_p$, k_{wf} is set to 1. The washout filter is chosen biproper with one fast pole to compensate for the relatively slow dynamics in $F_o(s)$. The fast pole is provided by $C_o(s)$. A general expression for $WF(s)$ is

$$WF(s) = k\frac{C_o(s)}{\Gamma_f(s)} = \frac{s}{s+p} \tag{4.35}$$

In this design phase p is set to 7 rad/s, much faster than the pole of F_o. According to Assumption 4.5, $p = a$, which corresponds to M = 0.91.

4.4.7 Input Compensator

According to the author in [1], $C_i(s)$ should be designed to ensure minimum relative degree of the estimation algorithm $EA(s) = \Gamma_\theta C_i(s)$. As such, $C_i(s)$ would ensure better phase margins [1]. A PI compensator is chosen as $EA(s)$ candidate because it has relative degree zero

$$EA(s) = C_i(s)\Gamma_\theta(s) = \frac{k_p s + k_i}{s} \tag{4.36}$$

Assumption 4.6 also holds. In fact $H_i(s)$ would be

$$H_i(s) = \frac{k_p s + k_i}{s(0.13s+1)} \tag{4.37}$$

k_p and k_i are chosen such that $\frac{1}{1+L(s)}$ is BIBO stable. Assuming for the time being $\phi = 0$ in rad/s, the general expression for $L(s)$ is

$$L(s) = \frac{a_p f''}{4}\mathrm{Re}\{e^{j\phi}F_i(j\omega_p)\}H_i(s) = 0.023f''\frac{k_p s + k_i}{s(0.13s+1)} \tag{4.38}$$

where f'' is assumed to be always positive. Computing $\frac{1}{1+L(s)}$ leads to

$$\frac{1}{1+L(s)} = \frac{0.13s^2 + s}{0.13s^2 + (1 + 0.023f''k_p)s + 0.023f''k_i} \tag{4.39}$$

The transfer function is BIBO stable if $k_p > -1/(0.023f'')$ and $k_i > 0$. Thus, choosing k_p and k_i greater than zero guarantees that $\frac{1}{1+L(s)}$ is BIBO stable. As shown in Figure 3.1, each platform mounts two nacelles with equal hub height. For design purposes, the same mean wind speed is assumed to act on both rotors of a platform. Following this assumption, it is chosen to set the same control gains in both SRTs of a platform. The baseline control strategy computes the pitch reference by means of a PI regulator with gain scheduling [15]. The implemented gain scheduling in [2] decreases the control gains as the wind speed increases. Due to the shear effect, the top platform is likely to experience higher wind speed than the bottom one [23]. Following the baseline implementation, it is chosen to set lower integral gains in the top platform than in the bottom one. The integral gains have the same order of magnitude as the baseline integral gain

(before gain scheduling). The baseline integral gain is 0.08. In this preliminary design the integral gains are set 25 % of the baseline integral gain for the top platform SRTs and 50 % for the bottom platform SRTs, respectively. Instead, the proportional gains are set one order of magnitude smaller than the integral gains. The choice is meant to avoid amplification of high frequency terms that are carried with the demodulation process. In Chapter 5, the control gains and the pole of the washout filter will be tuned to ensure appropriate regulation of the generator speed. Table 4.2 outlines the chosen preliminary gains.

Gains	Values
k_p	10^{-3}
k_i (bottom)	0.04
k_i (top)	0.02

Table 4.2: The table collects the preliminary control gains.

The ESC loop is defined. The resulting diagram is presented in Figure 4.10.

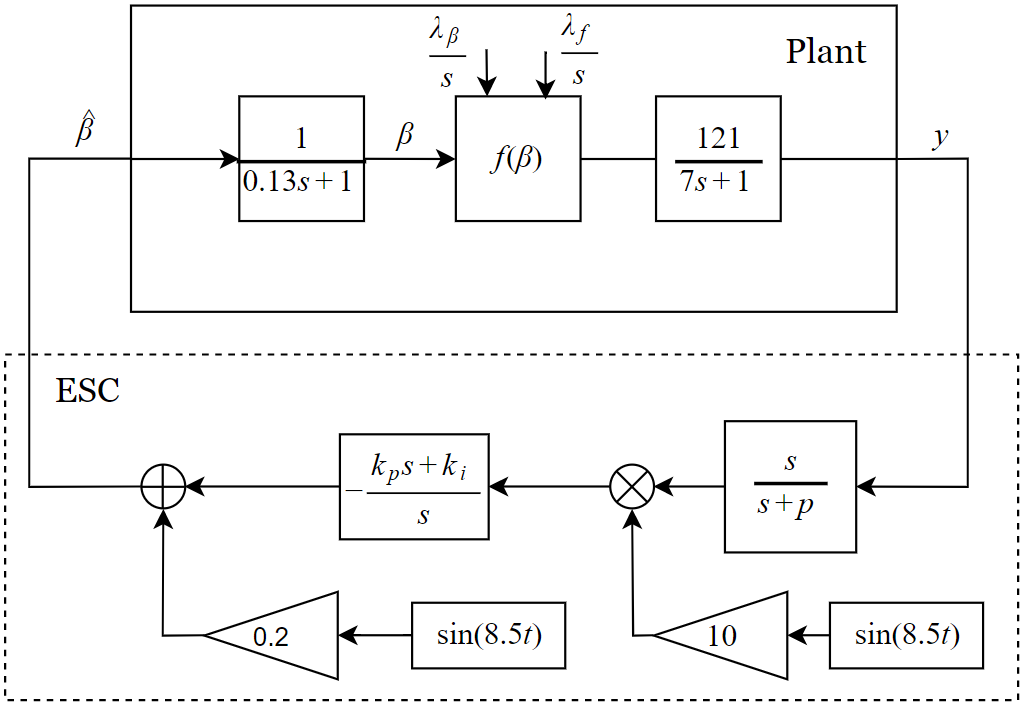

Figure 4.10: ESC block diagram after the design steps, reproduced and adapted from [1].

4.5 Chapter Summary

This chapter dealt with Extremum Seeking Control (ESC) and proposed a preliminary design to achieve generator speed regulation. The introductory example, proposed in Section 4.1, served the purpose to highlight the strength of the method. In particular ESC has been able to estimate the reference set-point that optimizes an unknown static mapping. Based on the outcome of the motivating example, an ESC based architecture has been tailored to the MRT system in Section 4.2. Section 4.3 clarified the relevant theoretical aspects of the updated ESC scheme, which can handle time varying f^* and θ^*, and also deal with unknown plant dynamics. The assumptions stated in Section 4.3 allowed to define each of the Plant subsystems in Figure 4.5. Finally, Section 4.4 dealt with the design steps to achieve local exponential convergence of the output error. The design guidelines have been applied to the system in use and a preliminary design to achieve generator speed regulation has been carried out.

CHAPTER 5

Performance Evaluation of PESC for Speed Regulation

This chapter assesses the performance of the PESC for speed regulation. First, the benchmark wind conditions and the success criteria are defined. Then the PESC is tuned to satisfy the stated requirements on speed regulation and mean power production. The limitations of the scheme regarding speed regulation are analyzed with the support of the closed loop frequency response. Finally, the chapter evaluates the impact of PESC on structural fatigue.

5.1 Wind Scenario and Evaluation Criteria

5.1.1 Benchmark Weather Conditions

According to the authors of the MRT control challenge paper [23], two environmental weather conditions are relevant for testing, namely Normal Turbulence Model (NTM) and Extreme Turbulence Model (ETM). The former is the weather the turbine is likely to experience during most of its lifetime. The latter is a rare weather event occurring on a 50-year cycle. The European regulation on wind turbine design IEC 61400-1 [9], provides more details about these weather models. In the MRT paper [23], the baseline controller is compared to the benchmark based on NTM weather conditions. 9 test scenarios cover the wind speed interval $V_{in} = 4$ in m/s, $V_{out} = 20$ m/s. Each scenario has 4 different wind profiles, one for each SRT. The shear effect is included in the model, hence top SRTs experience higher average wind speed than bottom ones. The test scenarios are available in the simulation environment [2] and differ each other in average wind speed. This project evaluates the ESC in FLR. The scenario with average wind speed at 18 m/s is utilized for performance assessment as it ensures that the wind speed is never below rated one, especially in the bottom SRTs. If the wind speed would be lower than rated, the available wind energy would not be enough to keep power production at P_N and the ESC would fail to regulate the generator speed. The benchmark wind scenario is depicted in Figure 5.1. In the same way as the control challenge paper [23], the simulation lasts for 200 s. Within the simulation time the average wind speed is above 18 m/s, as the red dashed lines in Figure 5.1 highlight. However, the ESC has to

compensate for up to 5 m/s wind speed changes, occurring in less than 20 seconds

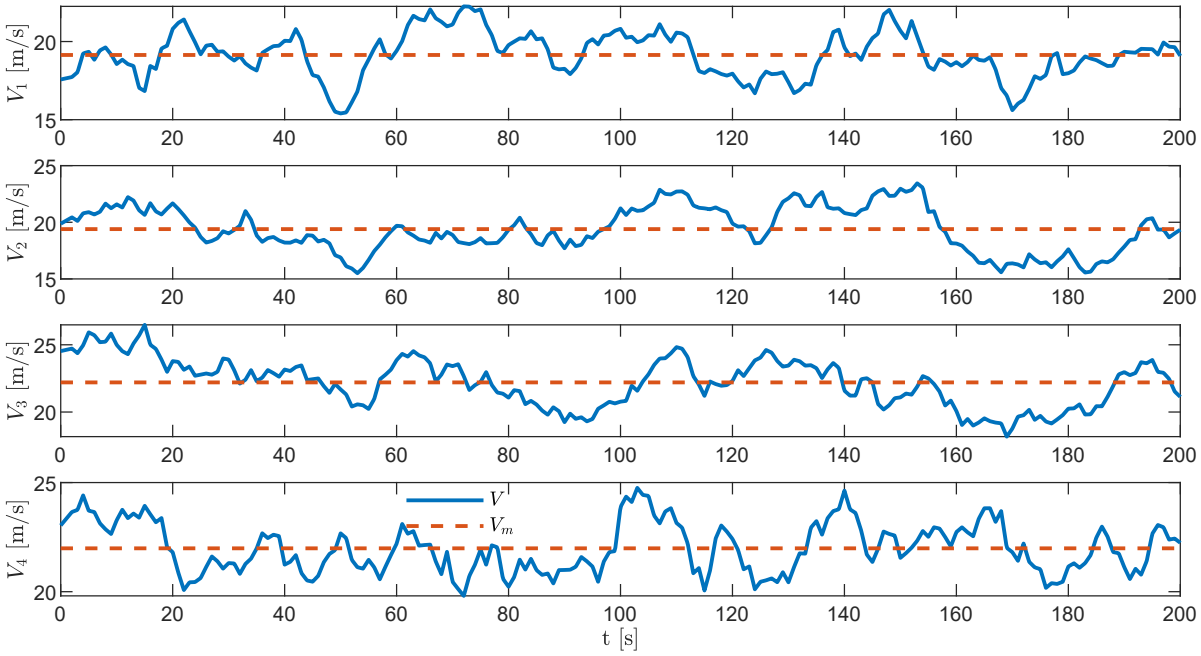

Figure 5.1: Benchmark NTM wind scenario. The scenario has been generated considering average wind speed $V_m = 18$ in m/s.

5.1.2 Success Criteria

The simulation environment [2] comes with a post-processing routine to compare two control designs and architectures at a time. The outcome of the routine is a table whose contents are relevant performance indices, typically the ratios of relevant parameters. The parameters provide information, among other things, about generator speed regulation, mean power production and structural fatigue, whereas the ratios indicate which control system performs best. The ratios are computed as Index(ESC) / Index(BMC). Generator speed regulation is quantified in terms of the generator speed mean and variance. A close mean to the reference generator speed indicates that the signal oscillates around the reference and the bias is limited. A small generator speed variance shows the capability of the control system to compensate quickly for wind speed variations. The BMC is already improving the mean and the variance of the generator speed compared to the baseline control strategy available in the simulator [2]. In the following it is assumed that the PESC achieves good speed regulation if the ratio of the means is as close as possible to one and the ratio of the variances is smaller than or equal to one. The ratios of the means and variances are computed for every nacelle to assess the performance individually. Mean power production is a relevant parameter. The authors of [23] state that a new control strategy must at maximum loose 3 % of the produced

power compared to the baseline control. Simulations show that the BMC is satisfying this requirement at $V_m = 18$ m/s. Hence, power production should be kept al least unchanged.

Structural fatigue is measured by means of DELs, as anticipated in Section 2.1.3. The benchmark paper [23] computes 7 DELs overall, including the tower root moment, yaw moments and arm torsion moments. Recalling Figure 3.4, the tower root moment is related to the modes in (a) and (b). Yaw moments cause platforms torsion, around the z axis (c). The arm torsion moments are responsible for the arms rotation around the x axis (d). Fatigue is mitigated compared to the BMC if the DELs ratios are smaller than 1. Evaluation parameters and success criteria are summarized in Table 5.1.

Index	Parameter	Method	Success Criteria
1	Generator Speed (Ω_g)	Ratio of the Mean of Ω_g	Ratio ≈ 1
2	Generator Speed	Ratio of the Variance of Ω_g	Ratio ≤ 1
3	Power Production	Ratio of the Mean Power	Ratio ≥ 1
4	Tower Root Moment (Mxy)	Ratio of DELs	Ratio ≤ 1
5	Yaw 1 Moment (Mz)	Ratio of DELs	Ratio ≤ 1
6	Yaw 2 Moment (Mz)	Ratio of DELs	Ratio ≤ 1
7	Arm 1 Root Moment (Mx)	Ratio of DELs	Ratio ≤ 1
8	Arm 2 Root Moment (Mx)	Ratio of DELs	Ratio ≤ 1
9	Arm 3 Root Moment (Mx)	Ratio of DELs	Ratio ≤ 1
10	Arm 4 Root Moment (Mx)	Ratio of DELs	Ratio ≤ 1

Table 5.1: The first column collects the evaluation parameters. The method to compute the parameters is outlined in the second column. Finally the third column shows the success criteria. By Ratio it is meant Index(ESC)/Index(BMC).

5.2 Tuning Process

At the end of the tuning process the appropriate k_i, k_p and p will enable every PESC loop to fulfil the requirements on power production and generator speed regulation. In fact, once speed regulation is achieved, so is the desired power production because the power reference is fixed to P_N. Hence, the aim of the tuning process is to fulfil the first two requirements in Table 5.1. The impact of PESC on fatigue is separately evaluated later in the chapter. The first step of the tuning process is to simulate the preliminary design developed in Chapter 4, according to the benchmark wind conditions defined in Section 5.1.1. The relevant performance indices as well as the preliminary ESC gains are reported in Table 5.2. Despite leading to comparable in mean generator speed outputs, yet the ratios of the variances is 3 on average. Further tuning is needed to improve the second performance index from Table 5.1. In order to do so, the integral

and proportional gains are gradually increased to reduce the variance ratio in Table 5.1, until no further improvement is obtained. The resulting gains and relevant performance indices are listed in Table 5.3.

Nac	$\overline{\Omega_g}$ Ratio	Var(Ω_g) Ratio	PESC Gains
1	0.99	3.1	$k_i = 0.04$ (bottom)
2	0.98	2.7	$k_i = 0.02$ (top)
3	0.98	3.7	$k_p = 10^{-3}$
4	0.99	3.0	$p = 7$

Table 5.2: Preliminary design, PESC vs Vestas BMC. The second and the third columns list the first two performance indices in Table 5.1. The fourth column reports the preliminary control gains.

Nac	$\overline{\Omega_g}$ Ratio	Var(Ω_g) Ratio	PESC Gains
1	0.99	1.5	$k_i = 0.065$ (bottom)
2	0.99	1.4	$k_i = 0.035$ (top)
3	0.99	2.0	$k_p = 5 \cdot 10^{-3}$
4	0.99	1.9	$p = 7$

Table 5.3: k_i and k_p tuning (Tuning 1), PESC vs Vestas BMC. The second and the third columns list the first two performance indices in Table 5.1. The fourth column reports the resulting control gains.

At this point the pole of the washout filter $-p$ is changed to further improve the second performance index. The pole should be selected to limit the phase shift introduced by the washout filter at frequencies close to the perturbation $\omega_p = 8.5$ rad/s. This action is beneficial to the demodulation process because it limits the phase difference between $DM(t)$ and the output of the washout filter, in a neighbourhood of the perturbation frequency. The pole p has to be reduced in order to limit the phase shift, as it can be seen in Figure 5.2. Specifically, p is set to 3 rad/s which reduces the phase shift from 45° to approximately 15°. The drawback is the reduction of the M ratio, as defined in Assumption 4.6 and with that, the distance between the pole of the washout filter and the slow pole of $F_o(s)$.

Simulation with the new parameters produces the performance indices in Table 5.4. The tuning of the washout filter allowed a reduction of the integral gain of the bottom platform. The proportional gains have been modified to respect the requirements on the generator speed variance. The chosen parameters allow to fulfil the requirements on generator speed regulation and mean power production. The time evolutions of the pitch references are compared in Figure 5.3. The references produced by the PESC follow the overall behaviour of the BMC reference. As expected, the ESC pitch continuously oscillates around the instantaneous value. The oscillations become wider when large changes in the pitch angle are required. That happens for example at around 55 seconds, in

$\beta_1(t)$. This behaviour has two side effects. On the one hand, it increases the activity of the pitch actuator with a direct impact on the actuator life. On the other hand it may affect fatigue. Section 5.4 investigates the correlation between the oscillations of the pitch reference and fatigue.

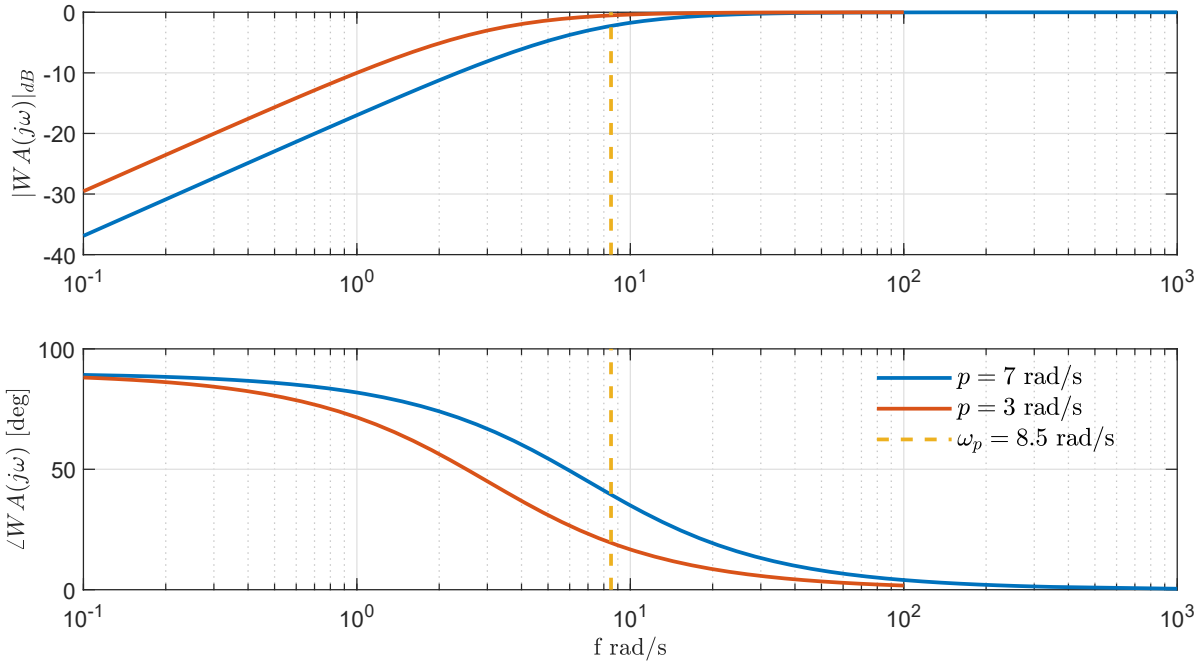

Figure 5.2: Bode diagram of both washout filters designs. The second design.

Nac	$\overline{\Omega_g}$ Ratio	Var(Ω_g) Ratio	$\overline{P}$ Ratio	k_p	k_i	p
1	0.99	1	1	$6 \cdot 10^{-4}$	0.05	3
2	0.99	1	1	$1.2 \cdot 10^{-3}$		
3	0.99	1	1	$2.5 \cdot 10^{-3}$	0.035	
4	0.99	1	1	$6.5 \cdot 10^{-3}$		

Table 5.4: Final Tuning (Tuning 2), PESC vs Vestas BMC. The second and the third columns list the first two performance indices in Table 5.1. The fourth column shows the ratios of mean power production. The last three columns reports the resulting control gains.

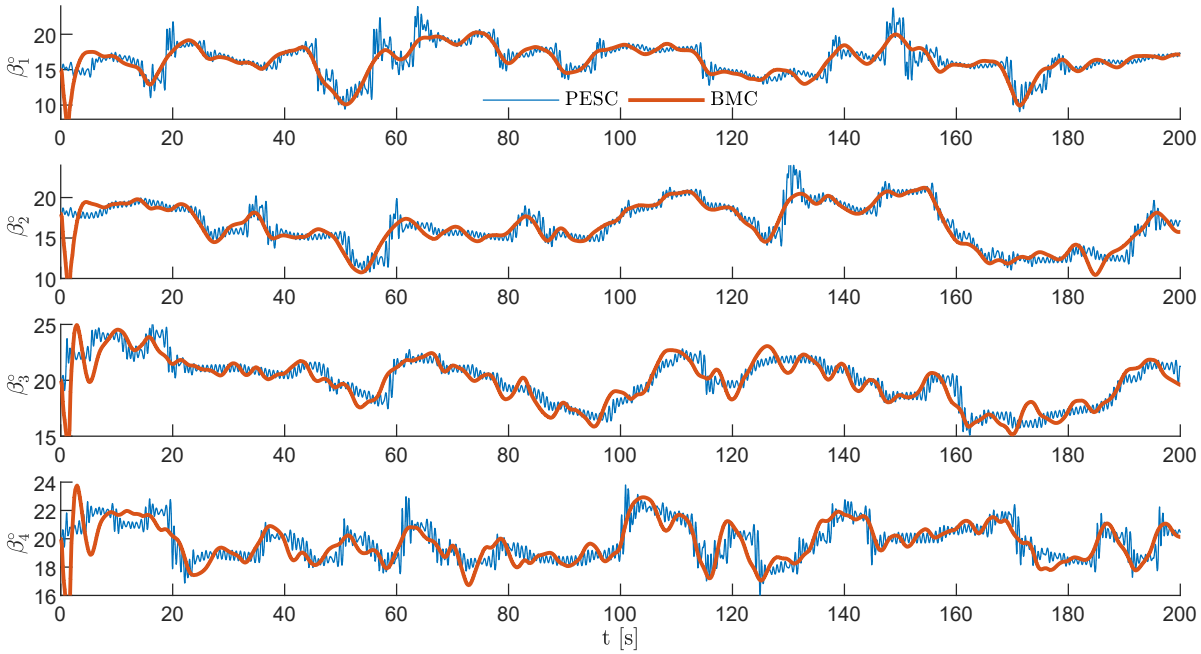

Figure 5.3: PESC vs Vestas BMC. Pitch references compared.

5.3 Wind to Pitch Reference Frequency Response

The wind to pitch reference frequency response carries information on the bandwidth of the closed loop system. In other words, it is related to the frequency range where the closed loop system is effective against wind variations. Analytical methods are not applicable. In fact, the transfer function is not available due to the non-linearity introduced by the demodulation and dithering signals. Running time domain simulations with sinusoidal wind inputs can be helpful to obtain an estimation of the frequency response. The Fourier series of the pitch reference carries information about amplitude and phase of the frequency response, as shown in Appendix A.

5.3.1 Simulations Set-up

Only one nacelle is active during each experiment and the same simulations are run for each of the tuning steps in Table 5.2, 5.3 and 5.4. The wind input is described by 1 m/s amplitude sinusoidal wind profiles spanning the frequency range 0.05 - 1 rad/s. Such frequency range is chosen because it carries most of the wind power density. Within the frequency range, the Power Spectral Density (PSD) is persistently greater than 0 in dB s/rad. For higher frequencies it is always below 0 in dB s/rad. Figure 5.4

shows the PSD of $V_1(t)$ from the benchmark wind scenario in Figure 5.1. Figure 5.4 highlights the upper bound on the frequency range for the computation of the frequency response. The interval has been divided in 10 frequency samples. The frequency response is approximated by its value at each sample. The sine waves are biased to 18 m/s. For each frequency the active nacelle has been initialized to $\Omega_N = 122.9$ rad/s and $\beta = 18°$. The coupling between the nacelle fore - aft velocity and the wind speed, as shown in Figure 3.3, is disabled during the simulations. This prevents unrealistic nacelle movements to influence the local wind speed V_{rot}. The movements are expected to be unrealistic because during normal operations all nacelles are active and interact with the support structure at the same time.

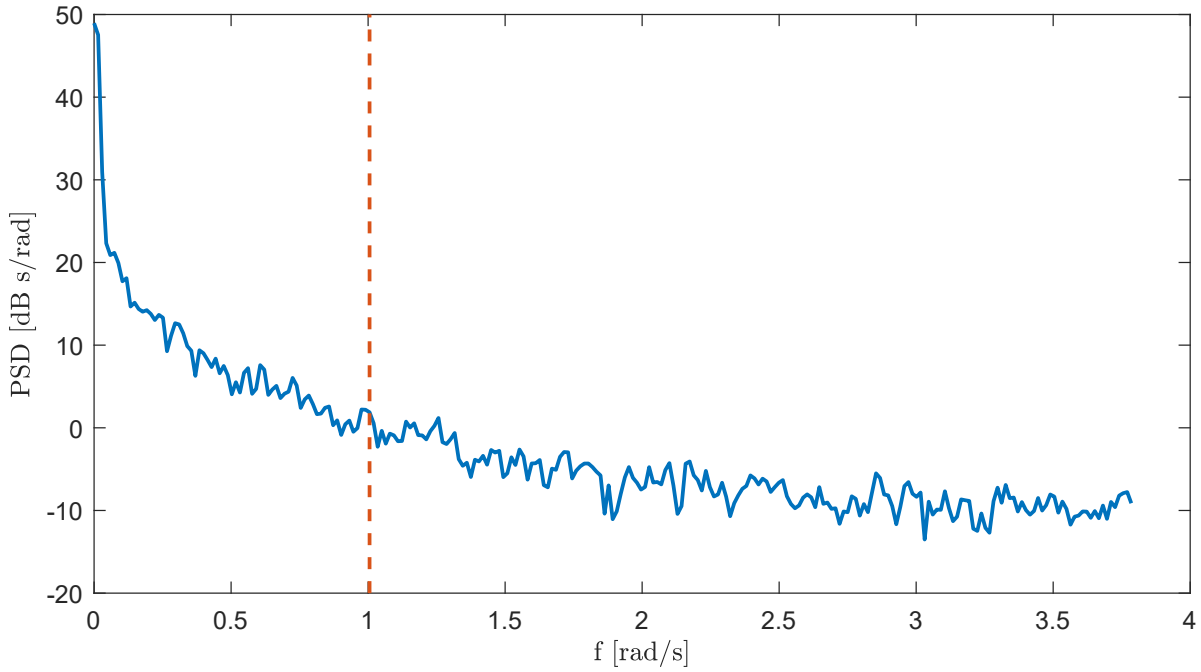

Figure 5.4: PSD of $V_1(t)$ from the benchmark wind scenario in Figure 5.1. The wind scenario shown here acts on the bottom left rotor. However, the frequency content does not change much for the other rotors. The dashed line is the upper bound on the frequency range that carries most of the wind power density.

5.3.2 Simulations Results

Figure 5.5 compares the obtained Bode diagrams. The tuning process sensibly widens the -3 dB bandwidth. In particular, the bandwidth of Tuning 2 is 0.7 rad/s for Nacelle 1 and 2, approximately. It is around 0.6 rad/s for Nacelle 3 and 4. Indeed, further tuning might lead to even wider bandwidth. However, since the drive train is also in the closed

loop, its dynamics influence the bandwidth. The PESC rejects wind changes to keep the generator speed as close as possible to the reference. Given the i-th measured output

$$y_i = (\Omega_{g,i} - \Omega_N)^2$$

the PESC changes the pitch reference only if the wind produces large enough deviations in the generator speed. Given a constant pitch reference, a change in the wind speed produces a change in the generator speed, driven by the drive-train dynamics. $\frac{\Omega_g(s)}{V(s)}$ defined in (5.1) is the transfer function from the wind speed to generator speed, around $V = 18$ m/s, when the pitch angle is fixed

$$\frac{\Omega_g(s)}{V(s)} = \frac{20}{6s+1} \tag{5.1}$$

The first order system in (5.1) has a -3 dB bandwidth of 0.17 rad/s. Above that frequency, (5.1) attenuates the changes in the wind speed, as the amplitude of the Bode plot decreases by 20 dB per decade. However, the attenuation effect is limited as long as the changes in the generator speed due to the wind are large enough to be captured by the PESC. The closer the frequency of the wind change to the upper bound in Figure 5.4, the higher the attenuation. At 1 rad/s the amplitude of the frequency response of (5.1) is 9.6 dB. Equivalently, 1 m/s wind change at that frequency produces 3 rad/s change in the generator speed, provided the pitch is constant. As such the change to be captured is less than 3 % of the generator speed reference.
To conclude, the drive train dynamics give a positive contribution to speed regulation at higher frequencies, as it filters the wind fluctuations. On the other hand, it limits the performance of the ESC because the smaller the generator speed deviations from the reference, the weaker the ESC action to compensate for them. The results highlight a direct correlation between the increment of the closed loop bandwidth and the reduction of the generator speed variance.

5.3.3 Nacelle Fore - Aft Velocity Variance and Closed Loop Bandwidth

Each tuning step tightens the control action over the generator speed and increases the bandwidth of the closed loop system. It also increases the variance of the nacelles fore-aft velocity, as reported in Table 5.5. There might be a direct correlation between the closed loop bandwidth and nacelle fore-aft velocity variance, as the pitch reference drives both the rotor torque and the thrust force [29]. The thrust and the torque act on the support structure and the larger the closed loop bandwidth is the wider the frequency spectrum of the excitation, with the possibility of hitting structural resonance frequencies. As stated in Section 2.1.3, when resonance frequencies are hit, larger tower movements should be expected. In the specific case, the bandwidth of Tuning 2 ESC

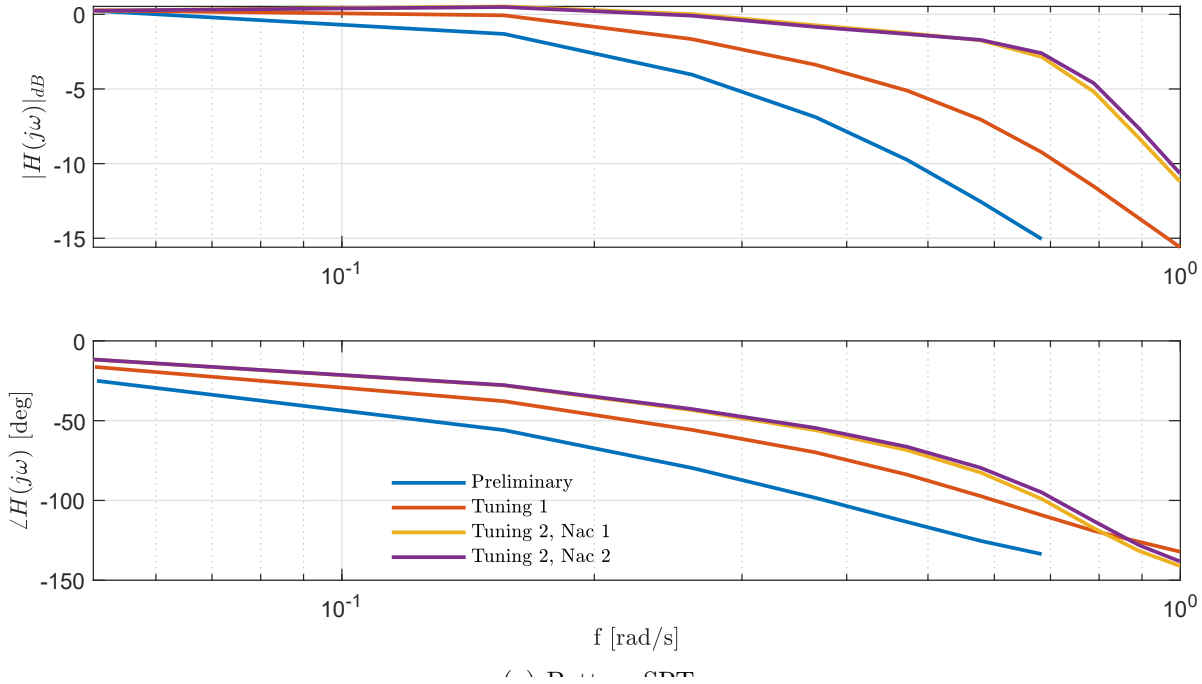

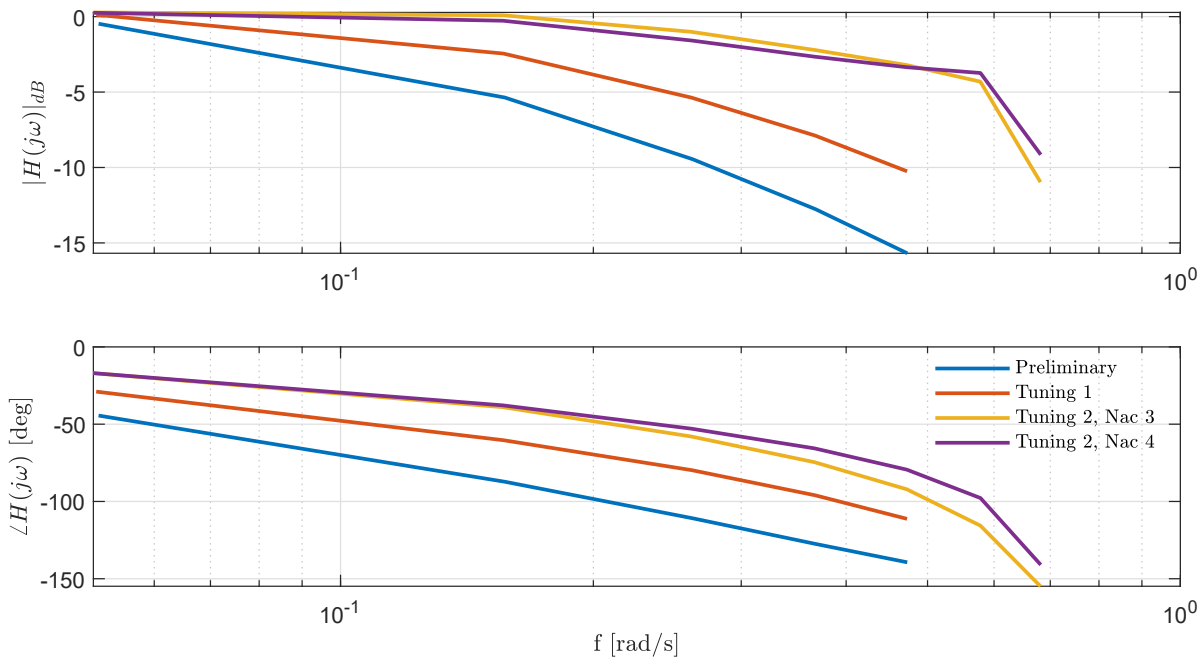

(b) Top SRTs

Figure 5.5: Bode diagrams of the closed loop system. Bandwidth increases moving from the preliminary tuning to Tuning 2.

is 0.7 rad/s in the bottom nacelles while it is 0.6 rad/s in the top ones. Indeed, the bandwidth chases the frequency of the first tower fore - aft mode shape, i.e. 0.75 rad/s

and of the symmetric yaw mode shape, i.e. 0.82 rad/s. The full set of the MRT mode shapes is available in Table 5.7.

5.4 Impact of PESC on Structural Fatigue

This section quantifies and compares the structural fatigue caused by the PESC and the BMC. The performance indices are the ratios of the DELs, following the guidelines in Table 5.1. The comparison against the BMC is made considering only the gains in Table 5.4. The results of the DELs test are shown in Table 5.6. All indices are far above one, clearly showing that this PESC design worsens fatigue compared to the BMC.

The block diagram developed in Chapter 3 is shown in Figure 5.6, as it supports the fatigue analysis in the frequency domain. The interconnections between the subsystems are recalled briefly before choosing the signals relevant to the frequency analysis. The analysis is based on the inspection of the PSDs.

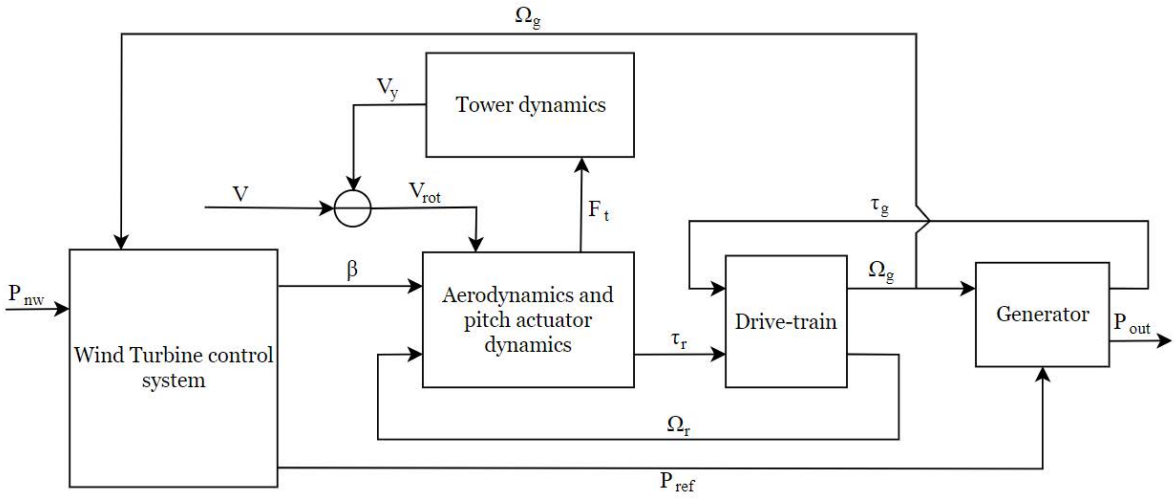

Figure 5.6: The diagram shows the signal routing and the interconnections between the subsystems.

Nac	Preliminary	Tuning 1	Tuning 2
1	0.4	0.4	0.8
2	0.4	0.5	0.7
3	0.6	0.6	0.9
4	0.6	0.7	0.9

Table 5.5: PESC vs BMC. Nacelle fore-aft velocity variance ratios. Tuning steps are shown from the left to the right.

DEL	Ratio
Tower Root Moment (Mxy)	5.75
Yaw 1 Moment (Mz)	5.35
Yaw 2 Moment (Mz)	4.35
Arm 1 Root Moment (Mx)	4.76
Arm 2 Root Moment (Mx)	4.69
Arm 3 Root Moment (Mx)	3.64
Arm 4 Root Moment (Mx)	3.86

Table 5.6: PESC vs BMC, DELs test. PESC is increasing structural fatigue compared to the BMC.

The PSDs of the moments in Table 5.6 depends directly on the thrust forces from each SRT. In turn, the PSD of the thrust forces is the result of the coupling between the PSDs of V_{rot}, of the pitch reference β and of the rotor speed Ω_r. The PSD of the rotor speed is the result of the dynamic interaction between the aerodynamic torque τ_r and the generator torque τ_g within the drive train. τ_r is one of the outputs of the aerodynamic subsystem. As such, its PSD also depends on the coupled actions of β, Ω_r and V_{rot}.
The aim of the PSD analysis is to evaluate the effect of PESC on fatigue in the frequency domain. The PSDs of the pitch references are shown because the pitch references are the outputs of the PESCs. The PSDs of the moments in Table 5.6 are also shown, as they are utilized to compute DELs ratios. However, it has been shown that the pitch references do not impact directly the PSDs of the moments, whereas it is the thrust forces that do. It is therefore relevant to show the PSDs of the thrust forces too.
The analysis begins with the pitch references, whose PSDs are available in Figure 5.7. Compared to the same plot for the BMC, the PESC power spectrum has two visible peaks, around ω_p and $2\omega_p$, respectively. The former peak is due to the combined action of the demodulation process and the dithering signal. The latter is due to the demodulation process, exclusively and in particular of the $\cos 2\omega_p t$ term shown in Section 4.1. Overall, the PESC is injecting more power than the BMC in the frequency range where the peaks arise. As expected, the power spectrum of the thrust forces in Figure 5.8 show a clear coupling with the pitch action. Similarly to the pitch, the PESC PSDs of the thrust forces exhibit an excess of power density around ω_p and $2\omega_p$. The power spectrum of the thrust forces directly impacts the PSDs of the loads, as shown in Figure 5.9. The support structure does not attenuate the excess of power density present in the thrust force. It does not because the excess of power density is in the same frequency range as many of the structural mode shapes.

As a consequence, the extra power density is visible in the PSDs of the loads. The mode shapes are specified in Table 5.7 and each of them is marked with a different colour. The same colours are utilized in Figure 5.8 to locate the frequencies of the mode shapes in the spectrum.
The formula for fatigue damage (2.5) assumes that the stress history is made by the sum of sinusoidal cycles with different amplitudes. As explained in Section 2.1.3, the

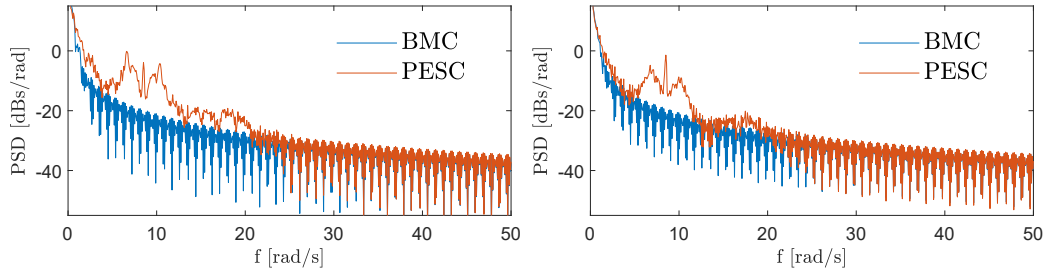

(a) Pitch Reference 1 (b) Pitch Reference 2

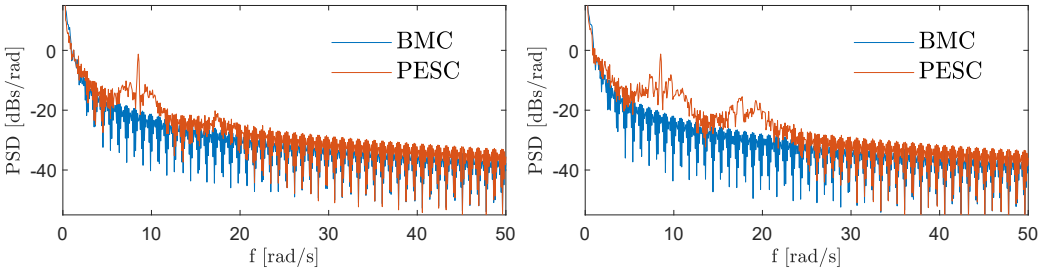

(c) Pitch Reference 3 (d) Pitch Reference 4

Figure 5.7: BMC vs PESC. The plots compare the PSDs of the pitch references.

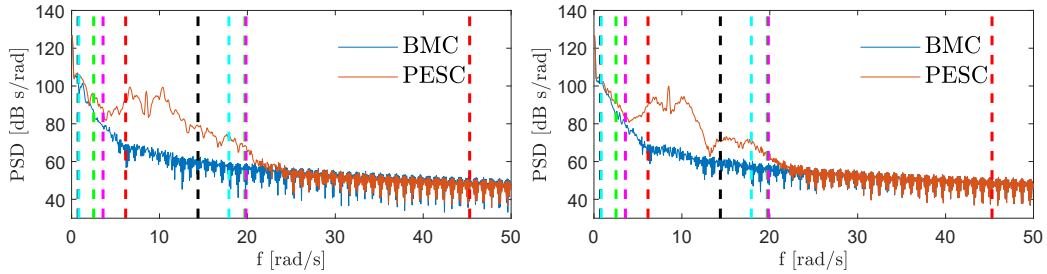

(a) Thrust Force 1 (b) Thrust Force 2

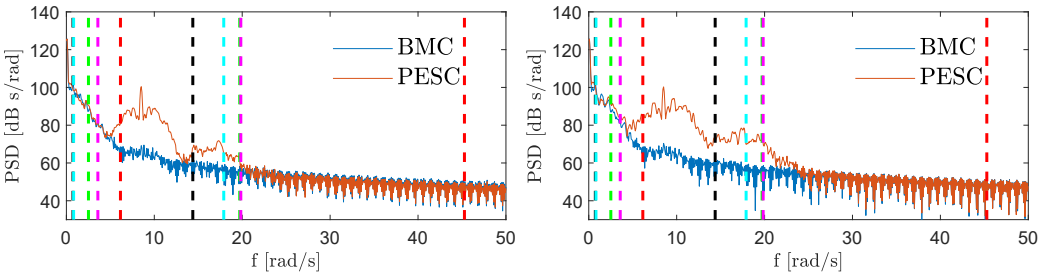

(c) Thrust Force 3 (d) Thrust Force 4

Figure 5.8: BMC vs PESC. The plots compare the PSDs of the thrust forces.

rainflow counting algorithm counts how many full cycles occur at a given amplitude. The algorithm outputs a vector of amplitudes A_i and the corresponding number of cycles N_i that are combined in the formula that defines the DEL [3]

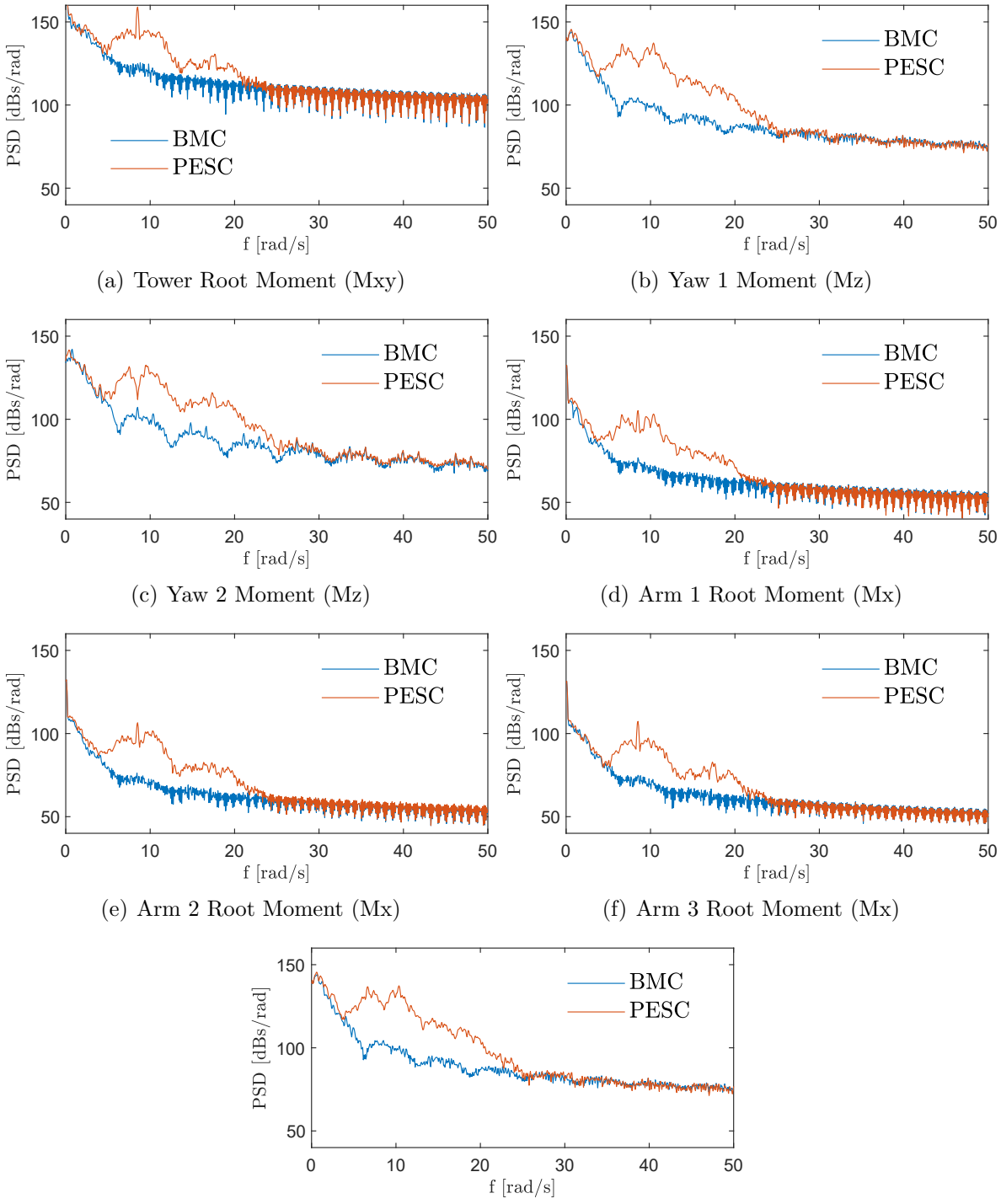

(a) Tower Root Moment (Mxy)

(b) Yaw 1 Moment (Mz)

(c) Yaw 2 Moment (Mz)

(d) Arm 1 Root Moment (Mx)

(e) Arm 2 Root Moment (Mx)

(f) Arm 3 Root Moment (Mx)

(g) Arm 4 Root Moment (Mx)

Figure 5.9: BMC vs PESC. The plots compare the PSD of the moments utilized to compute DELs .

Mode	Description	Freq. (rad/s)
1	First tower fore - aft	0.75
2	Symmetric yaw	0.82
3	Second tower fore - aft	2.51
4	Asymmetric yaw	3.58
5	II tower fore - aft coupled with arm torsion	6.15
6	Symmetric arm torsion of upper platform	14.38
7	Symmetric arm torsion of lower platform	17.90
8	Asymmetric arm torsion of upper platform	19.72
9	Asymmetric arm torsion of lower platform	19.84
10	Arm torsion coupled with rotational tower	45.28

Table 5.7: Mode shapes and frequencies for the MRT [23]. The colours correspond to the dashed lines in Figure 5.8.

$$DEL = \sum_i N_i A_i^m$$

The PESC PSDs in Figure 5.9 are greater than the BMC PSDs in a wide range of frequencies. It may be the case that more cycles are happening in a certain range of amplitudes. This fact would explain the increased DELs.

5.5 Chapter Summary

The aim of this chapter was to assess the performance of the PESC for speed regulation, designed in Chapter 4. The ESC scheme has been compared against the BMC in terms of generator speed regulation, mean power production and finally fatigue. To the extent of the simulations carried out with the benchmark wind scenario, Tuning 2 ESC achieved as good performance as the BMC in terms of generator speed regulation and mean power production. However, ESC worsened structural fatigue. With respect to this outcome, the PSD analysis highlighted the presence of peaks in the ESC power density of the thrust forces, in the neighbourhood of the probing frequency ω_p and $2\omega_p$, respectively. Hence, the support structure was subject to higher excitation in the frequency range where most of the mode shapes are. In this frequency range, the structure was not expected to attenuate the power density from the thrust forces, which in turn was visible in the loads PSDs. Finally, it was concluded that the excess of power density in the loads might have been related to the increased structural fatigue.

CHAPTER 6

Fatigue Mitigation Approaches

The chapter investigates two methods for addressing the problem of fatigue caused by the ESC developed in Chapter 4 and 5. A new design of the input compensator is proposed in the first approach to remove part of the extra power density present in the PSDs of the pitch references. The second approach does not change the design of the ESC. However, it requires to expand the measured cost to include fatigue related terms. The results of applying the two approaches are first discussed individually and then comparatively, in terms of fatigue mitigation and generator speed regulation.

6.1 Fatigue Mitigation by New Design of the Input Compensator

In this section, the design of the input compensator developed in Section 4.4.7 is modified to include a first order low pass filter. The low pass filter is meant to remove the extra power density introduced by the demodulation and the additive perturbation in the pitch reference. As explained in Section 4.1, the demodulation introduces a $\cos(2\omega_p t)$ that is clearly visible in the PSDs of the pitch references, Figure 5.7.
Many references [1], [30], [31], [17], [18] propose to utilize a first order low pass filter to deal with $\cos(2\omega_p t)$, a signal that does not contribute to the demodulation. In fact, this signal is one of the factors that worsen fatigue in the MRT. The main downside of this approach is that it attenuates the effect of the probing signals, hence stability is more difficult to achieve [1].

6.1.1 Success Criteria

The tuning of the newly designed input compensator $C_i(s)$ is successful if it can alleviate the excess of power density in the neighbourhood of $2\omega_p = 17$ rad/s. The new ESC scheme is tested in the benchmark weather conditions defined in Section 5.1.1 and compared against Tuning 2 ESC in Table 5.4 in terms of DELs and generator speed regulation.

6.1.2 Design of the new Compensator

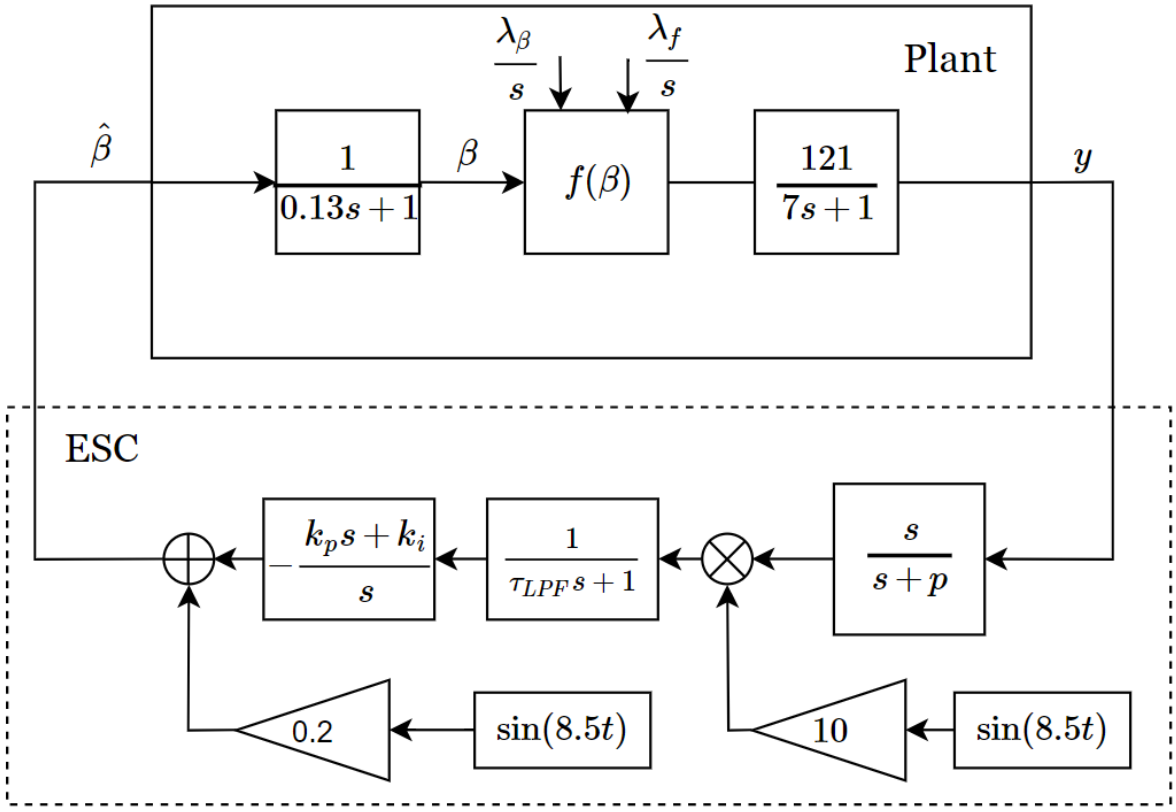

Figure 6.1: ESC block diagram after introducing the low pass filter. Adapted and reproduced from [1].

The new block diagram of the ESC is depicted in Figure 6.1. Compared to the scheme shown in Figure 4.10, the new design includes a low pass filter before the PI regulator. Thus, no changes occur in any of the steps outlined in Section 4.4.3, but in the design of the input compensator $C_i(s)$. The estimation algorithm EA(s) is rewritten as follows

$$EA(s) = C_i(s)\Gamma_\theta(s) = \frac{k_p s + k_i}{s}\frac{1}{\tau_{LPF}s+1} \tag{6.1}$$

The new design must ensure BIBO stability of $\frac{1}{1+L(s)}$. The expression of $\frac{1}{1+L(s)}$ is reported in the following.

$$\frac{1}{1+L(s)} = \frac{s(0.13s+1)(\tau_{LPF}s+1)}{0.13\tau_{LPF}s^3 + (0.13+\tau_{LPF})s^2 + (1+0.023f''k_p)s + 0.023f''k_i} \tag{6.2}$$

where f'' is the second derivative of the unknown mapping evaluated at θ^*. As stated in Section 4.3.2, only the sign of f'' is known, whereas its value is unknown. Instead, τ_{LPF},

k_p and k_i result from the ESC tuning, hence they are known. The missing knowledge about f'' does not allow to prove local exponential convergence of the scheme, according to the theorem in Section 4.4.1. However, it is possible to find the range of f'' in which the chosen parameters τ_{LPF}, k_p and k_i ensure BIBO stability of (6.2). This analysis is performed in Section 6.1.2.1.

6.1.2.1 Compensators Tuning

At the beginning, the gain values k_p and k_i are the same as in Tuning 2 ESC (Table 5.4). At the same time, τ_{LPF} is increased gradually. When τ_{LPF} reaches 0.1 in s/rad, stability issues arise, in particular the pitch references of SRT 1 and 2 become unstable. τ_{LPF} is then kept constant at 0.1 in s/rad while the integral gain is reduced until the stability issues disappear. Setting k_i of the bottom nacelles to 0.035 solves the stability issues. At this point, τ_{LPF} is increased until most of the extra power density in the neighbourhood of $2\omega_p$ is removed. As shown in Figure 6.2, the new $C_i(s)$ filters away the extra power density in the desired frequency interval. However, the peak in the neighbourhood of $\omega_p = 8.5$ in rad/s can not be completely filtered away, else the ESC would incur into stability issues. The resulting parameters are presented in Table 6.1. Using the tuning parameters in Table 6.1, (6.2) is rewritten as

$$\frac{1}{1+L(s)} = \frac{s(0.052s^2 + 0.43s + 1)}{0.052s^3 + 0.43s^2 + (1 + 9.2 \cdot 10^{-5} f'')s + 8.05 \cdot 10^{-4} f''} \tag{6.3}$$

To find in which range of f'' the transfer function in Eq. (6.3) is BIBO stable, f'' is varied from 10^{-5} to a very big value, here set to 10^9. The three poles of (6.3) are then computed. It has been found that the real parts of the poles are always strictly negative, hence (6.3) is BIBO stable, at least for $f'' \in [10^{-5};\ 10^9]$. Furthermore, simulations of the closed loop system with the benchmark wind conditions show a clearly stable behaviour. However, it is not possible to conclude on the BIBO stability of the closed loop system in all FLR wind scenarios because the value of f'' is unknown. An approach could be to numerically estimate f'' or to exploit extra knowledge about the MRT system.

Gains	Values
k_p	$4 \cdot 10^{-3}$
k_i	0.035
τ_{LPF}	0.4 s/rad

Table 6.1: New input compensator design, tuning parameters. The same parameters are chosen for each nacelle.

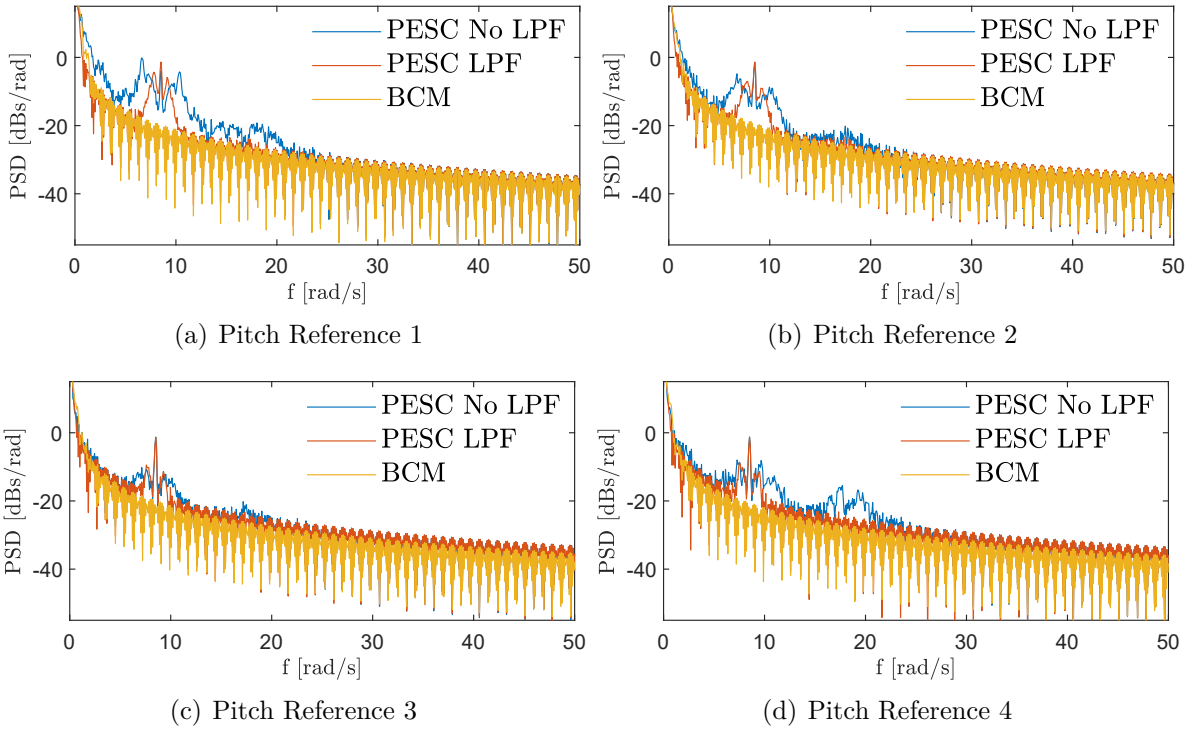

(a) Pitch Reference 1

(b) Pitch Reference 2

(c) Pitch Reference 3

(d) Pitch Reference 4

Figure 6.2: PSDs of the pitch references. The blue line refers to Tuning 2 from Table 5.4. The red line refers to the ESC that includes a low pass filter. The yellow line is the PSD of the benchmark.

6.1.3 Impact on Fatigue and Generator Speed Regulation

Computing the DELs ratios between the new ESC design including the low pass filter (from now on PESC LPF) and Tuning 2 ESC is the first step to assess the impact of the new input compensator design on fatigue. In fact, the new design and tuning proves useful in mitigating fatigue, as all the DELs ratios in Table 6.2 are smaller than 1.
In the same fashion as in Section 5.4, the inspection of the PSDs helps clarifying the effect of the LPF on the power spectrum. For instance, the power density of the thrust forces in Figure 6.3 is attenuated in the frequency range where most of the mode shapes are. As a matter of fact the power density of the loads in Figure 6.4 is also attenuated in the same frequency range, which in turn, has a positive effect on fatigue. The PSD of the BMC is always plotted to highlight the difference between Tuning 2 ESC and PESC LPF.

PESC LPF mitigates fatigue but also increases the variance of the generator speed. The second column of Table 6.3 quantifies this effect and actually shows that bottom SRTs suffer the effect the most. The behaviour of the generator speed along the wind scenario in Figure 6.5 confirms the tendency introduced in Table 6.3. Figure 6.5 at page 63 plots

DEL	Ratio
Tower Root Moment (Mxy)	0.90
Yaw 1 Moment (Mz)	0.62
Yaw 2 Moment (Mz)	0.63
Arm 1 Root Moment (Mx)	0.79
Arm 2 Root Moment (Mx)	0.75
Arm 3 Root Moment (Mx)	0.85
Arm 4 Root Moment (Mx)	0.84

Table 6.2: ESC LPF vs Tuning 2 ESC (Table 5.4), DELs ratios test.

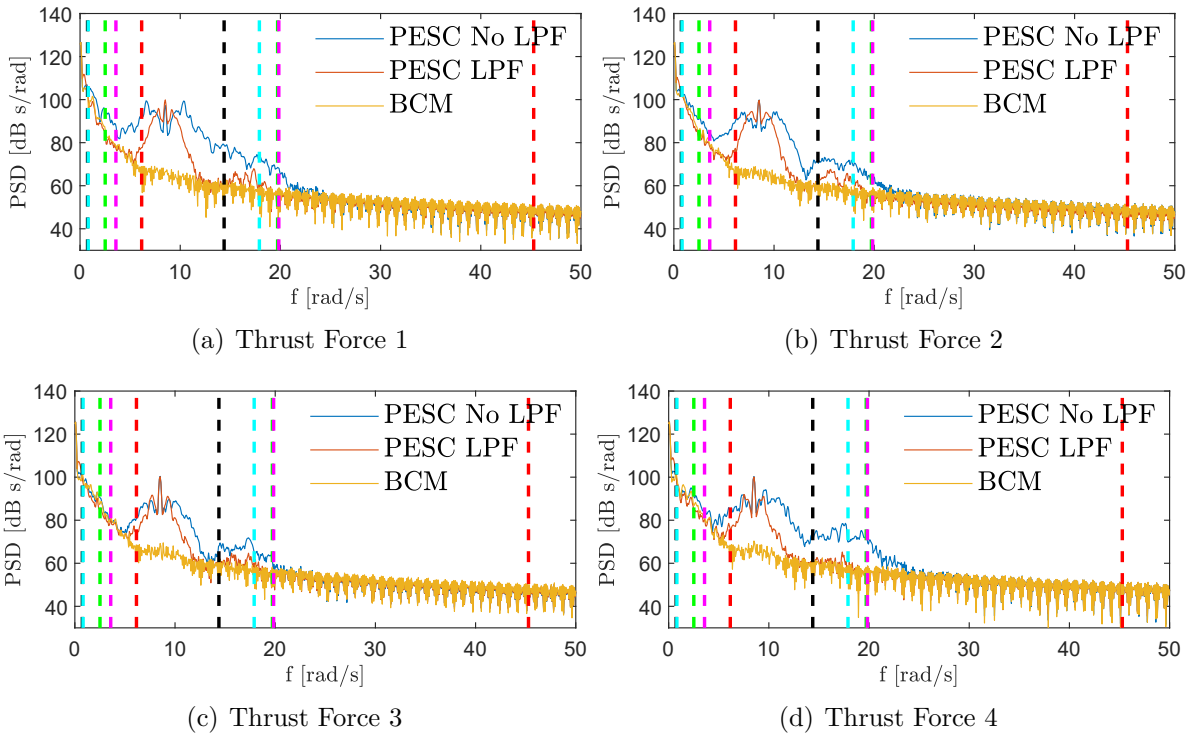

(a) Thrust Force 1

(b) Thrust Force 2

(c) Thrust Force 3

(d) Thrust Force 4

Figure 6.3: PESC LPF vs Tuning 2 ESC, PSD of the thrust forces compared. In yellow the PSD of the BMC. The dashed lines represent the frequencies of the mode shapes following the definition and the colour codes in Table 5.7.

the generator speed of each SRT followed by the corresponding benchmark wind scenario. The generator speed plot refers to both Tuning 2 ESC and PESC LPF. Clearly bottom SRTs experience harsher wind conditions compared to the top ones and this influences generator speed regulation. For instance, at around 50 seconds from the beginning of the simulation, SRT 1 experiences a wind speed drop from 20 m/s to 15 m/s followed by a sudden increment up to 22 m/s. The whole event happens in less than 20 seconds and here the PESC LPF struggles to regulate the generator speed. Again, a wind drop at around 150 seconds causes the generator speed of SRT 2 to become lower than the

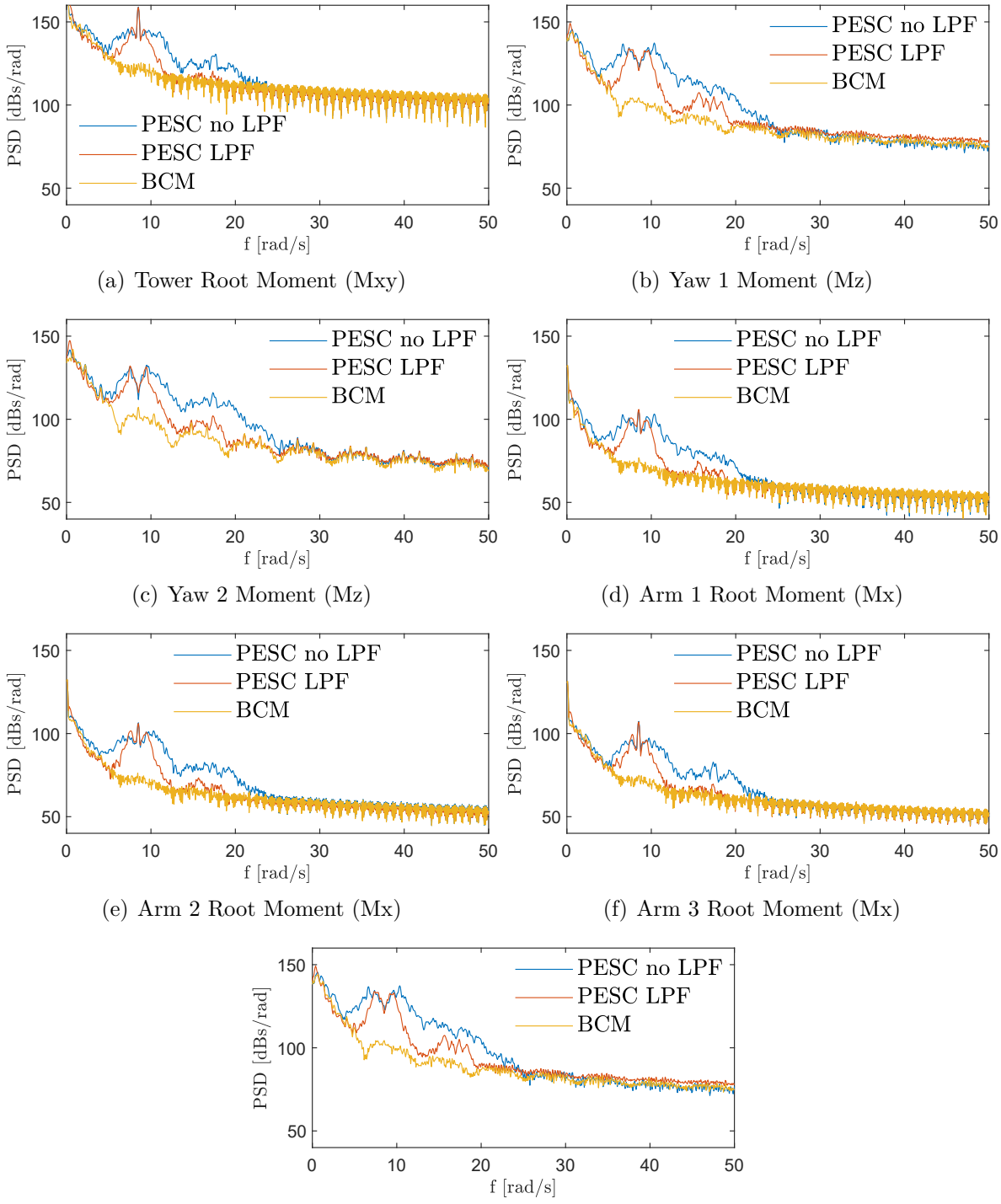

(a) Tower Root Moment (Mxy)

(b) Yaw 1 Moment (Mz)

(c) Yaw 2 Moment (Mz)

(d) Arm 1 Root Moment (Mx)

(e) Arm 2 Root Moment (Mx)

(f) Arm 3 Root Moment (Mx)

(g) Arm 4 Root Moment (Mx)

Figure 6.4: PESC LPF vs Tuning 2 ESC, PSD of the loads compared. In yellow the PSD of the BMC.

reference value, fixed at 122.9 rad/s. Speed regulation is better in the top SRTs, instead. Despite experiencing drops and sudden increments, the wind speed is almost never below 20 m/s. This fact might help speed regulation.

Nac	$\overline{\Omega_g}$ Ratio	Var(Ω_g) Ratio
1	1.00	5.3
2	1.00	4.2
3	1.00	2.5
4	1.00	3.5

Table 6.3: PESC LPF vs Tuning 2 ESC, ratios of the mean and the variance of the generator speed.

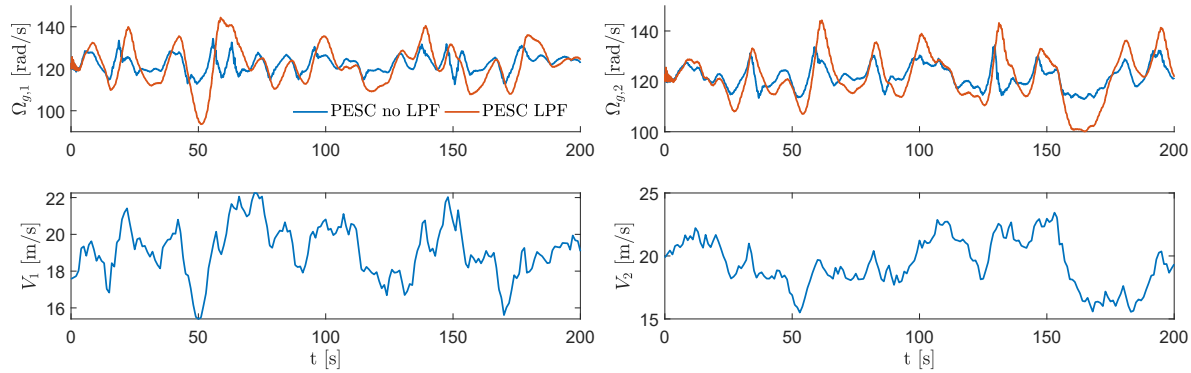

(a) SRT 1

(b) SRT 2

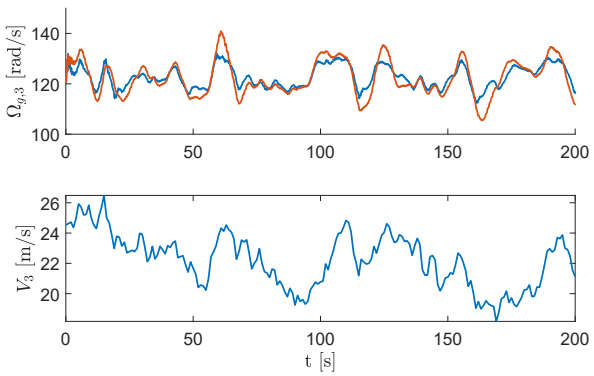

(c) SRT 3

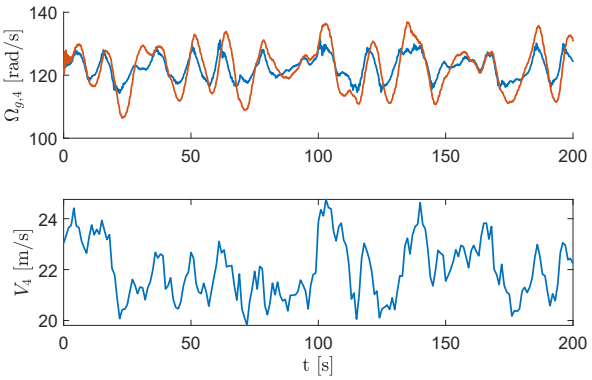

(d) SRT 4

Figure 6.5: PESC LPF vs Tuning 2 ESC, plots of the generator speed at nacelle i, followed by the benchmark wind scenario at nacelle i.

6.2 Fatigue Mitigation by Modification of the Measured Cost

The fatigue mitigation strategy developed in Section 6.1 requires a new design of the input compensator. Differently, the strategy developed in this Section attempts to achieve fatigue mitigation acting on the measured cost. Up to this point the measured cost at nacelle i has been

$$y_i = (\Omega_{g,i} - \Omega_N)^2 \tag{6.4}$$

as defined in Section 4.3.2.1. It is possible to include a term related to fatigue to the measured cost, as showed in Section 4.3.2.2. The expression of the measured cost at SRT i proposed in Section 4.3.2.2 is showed here

$$y_i = y_{gr,i} + y_{fm,i} \tag{6.5}$$

$$y_{gr,i} = \frac{W_i}{\sigma^2_{\Omega_g}}(\Omega_{g,i} - \Omega_N)^2 \tag{6.6}$$

$$y_{fm,i} = \frac{1 - W_i}{\sigma^2_{F_i}} F_i^2 \quad i = 1, ..., \ 4 \tag{6.7}$$

The measured cost is made by two terms, i.e. $y_{gr,i}$ and $y_{fm,i}$. The former deals with the first objective, i.e. generator speed regulation. The latter deals with the second objective, i.e. fatigue mitigation. W_i is a weight such that $W_i \in [0, 1]$. The gain allows the trade-off between fatigue mitigation and regulation of the generator speed. $W_i = 1$ means no fatigue mitigation at all. $y_{gr,i}$ is scaled by the variance of the generator speed, $\sigma^2_{\Omega_g}$. F_i is the description of fatigue at the i-th SRT. $y_{fm,i}$ is also scaled by its variance, $\sigma^2_{F_i}$. The variances $\sigma^2_{\Omega_g}$ and $\sigma^2_{F_i}$ are estimated in simulation and they are meant to normalize the cost to 1. Furthermore, the normalization makes the size of $y_{gr,i}$ and $y_{fm,i}$ comparable. This aspect is helpful when tuning W_i.
The choice of F_i is operated in the following. Quantification of fatigue is not a trivial task as stated in Section 2.1.3. As a matter of fact, the process of finding an expression for F_i that could reduce fatigue instead of worsening it, required a lot of attempts that did not produce the expected results. Each attempt, including the successful one, can be summarized through the following common steps

1. Simulate using Tuning 2 ESC. Estimate $\sigma^2_{\Omega_g}$ and $\sigma^2_{F_i}$ that normalize the measured cost to 1 and make $y_{gr,i}$ and $y_{fm,i}$ of comparable size.

2. Set $W_i = 1$ for $i = 1, ..., \ 4$. Tune the ESC to regulate the generator speed according to the new measured cost. The ESC is tuned to increase the generator speed variance compared to Tuning 2 ESC in Table 5.4.

3. Assess the impact of the tuning on fatigue by computing the DELs ratios against tuning 2 ESC.
4. Reduce one W_i at a time to include fatigue mitigation in the ESC loops.
5. Evaluate the impact of W_i tuning on fatigue and generator speed regulation. Make the comparisons against Step 3 tuning. Utilize the success criteria in Table 5.1.
6. Inspect the behaviour of the pitch reference and the generator speed at each nacelle.

Before focusing on the successful attempt, it is worth summarizing briefly the most relevant attempts that failed to mitigate fatigue and, in fact, threatened stability.

6.2.1 Review of the Unsuccessful Attempts

Platforms' fore - aft displacements and velocities are utilized in the benchmark paper [23] to produce two extra pitch signals that, once added to the baseline SRT pitch, contribute to mitigating fatigue. Instead, nacelle fore - aft movement is utilized here to represent F_i. The reason not to choose platform fore - aft movement is that it does not provide local information about nacelle i. In fact it is the result of the interaction between two SRTs in a platform. In a preliminary phase, nacelle fore - aft displacement has been ignored because it was desired to leave some flexibility in the tower fore - aft deflection. In fact, if the fore - aft displacement of all nacelles' is minimized, then the tower would experience small deflection. Instead, minimizing nacelles fore - aft velocities, or both velocities and accelerations would leave more flexibility to the tower displacement. Specifically, the tower would experience a static deflection, while the oscillations around this static deflection would be reduced. Based on these considerations, the following F_i candidates have been proposed and tested according to the steps enumerated in Section 6.2:

1. $F_i = V_{y,i}$ for $i = 1, ..., 4$, where $V_{y,i}$ is the instantaneous fore - aft velocity of nacelle i.
2. $F_i = V_{y,i} + \dot{V}_{y,i}$ for $i = 1, ..., 4$, where $\dot{V}_{y,i}$ is the instantaneous fore - aft acceleration of nacelle i.

A common behaviour has been observed in both approaches. W_i has been gradually reduced, first on one measured cost at a time, then on some of measured costs and finally on all the measured costs. To the author's knowledge, in none of the analyzed cases it was possible to reduce the DELs ratios. In fact, the smaller W_i the larger the ratios were. Below a certain threshold, $W_i = 0.8$ for bottom SRTs and $W_i = 0.9$ for top SRTs, the closed loop system even became unstable. A last attempt has been made to mitigate fatigue using nacelle fore - aft velocity. This time F_i was chosen as $V_{y,1} - V_{y,2}$ for nacelle 1 and 2 and $V_{y,3} - V_{y,4}$ for nacelle 3 and 4. The reason to choose this representation was that minimizing the fore - aft velocities difference would reduce

the torsional oscillations (see Figure 3.4 (c)) of a platform and, eventually, fatigue. The observed behaviour is similar to that in the previous attempts. Decreasing W_i would increase the DELs ratios first and then induce closed-loop instability.
According to [29], the MRT support structure might be considered as a *soft tower*. In the technical jargon, a tower is said to be *soft* if its fore - aft resonance frequency is low enough. As shown in Table 5.7, the MRT support structure has three fore - aft mode shapes. The first one occurs at 0.75 rad/s, which is low frequency enough to consider the MRT support structure *soft*, according to [29]. A *soft tower* has a relatively low damping. Then, the goal of a fatigue relieving control strategy is to increase the damping of the tower. This is also how the BMC operates and mitigates fatigue. As a matter of fact, the three attempts were unsuccessful possibly because the control action was removing damping, rather than increasing it.

6.2.2 Including Nacelle Fore - Aft Displacement to the Measured Cost

In some industry applications [29], it has already been possible to mitigate fatigue in *soft towers* of SRTs, by means of nacelle fore - aft displacement feedback. Based on this information, it was decided to include nacelle i fore - aft displacement $u_{y,i}$ to the i-th measured cost. The expression of the i-th measured cost would then be

$$y_i = \frac{W_i}{\sigma^2_{\Omega_g}}(\Omega_{g,i} - \Omega_N)^2 + \frac{1 - W_i}{\sigma^2_{u_y}} u^2_{y,i} \quad i = 1, ..., \ 4 \tag{6.8}$$

In the following, the i-th ESC loop minimizes the i-th measured cost in (6.8) to regulate the generator speed in FLR and achieve fatigue mitigation compared to Tuning 2 ESC in Table 5.4. Before tuning the scheme it is worth introducing some assumptions that are meant to deal with some limitations of the scheme.

6.2.2.1 Limitations and Assumptions

The main downside of having four ESC loops running independently, is that there is no shared information among them. In principle, the loops might compete against each other to achieve the local optimal compromise between minimization of nacelle displacement and generator speed regulation. As a matter of fact, the movement induced on one nacelle by the pitch action to achieve the local trade-off might disturb the action of another ESC loop, especially on the same platform.
In Section 3.2.4 it is assumed that arms are very stiff. Hence, the main motion around the Z axis is platform torsion, as shown in Figure 6.6 (a). The following assumptions are adopted.

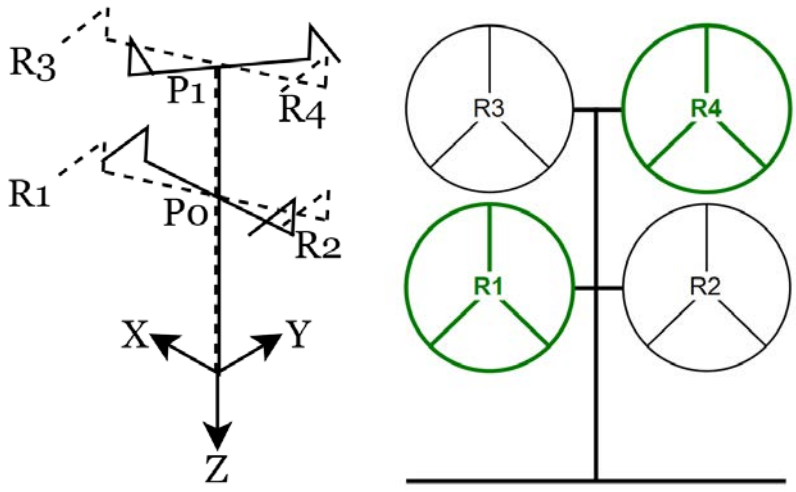

(a) Platforms torsion (b) Trade off Configuration

Figure 6.6: The platforms torsion is depicted in (a). (b) shows the configuration of the optimization routines. The rotors labelled in green include nacelle fore - aft displacement compensation.

Assumption 6.1 Regarding platforms torsion, it is assumed that when one nacelle is moving forward, the other one is moving backward and the other way around.

If Assumption 6.1 holds, then one ESC per platform compensating for nacelle fore - aft displacement is enough to reduce platform torsion and possibly Yaw i DEL, as defined in Table 5.1. Instead, the positive action on Arms DELs needs to be verified with testing.

Assumption 6.2 The structural coupling between nacelles mounted on opposite sides of two different platforms is lower than the coupling between nacelles mounted on the same side of the platforms.

If Assumption 6.2 holds, then the risk of competition between the optimization routines can be mitigated if compensation of the fore - aft displacement happens in SRT mounted on the opposite sides of two different platforms. The configuration of the resulting optimization routines is shown in Figure 6.6 (b). The rotors labelled in green measure the cost in (6.8) with $W_i < 1$, hence reduce nacelle fore - aft displacement. The rotors labelled in black simply regulate generator speed. The measured cost is again given by (6.8), with the difference that W_i is set to 1.
As shown in Figure 6.6 (b), rotors 1 and 4 reduce fore - aft displacement. This choice is operated considering the PSDs of the pitch references in Figure 5.7. To mitigate fatigue, the technique is expected to reduce the excess of power density in the neighbourhood of $\omega_p = 8.5$ in rad/s and $2\omega_p = 17$ in rad/s, especially in those SRT where the trade - off is enabled. In Figure 5.7, the ESC loops 1 and 4 introduce more power density compared to the BMC than ESC loops 2 and 3 do. Then, it is convenient to enable fore - aft

displacement compensation in SRTs 1 and 4, where there is more power density to be removed.

6.2.2.2 Success Criteria

The new strategy (from now on PESC FM) will be tested according to the benchmark weather conditions defined in Section 5.1.1. PESC FM is compared against Tuning 2 ESC following the success criteria in Table 5.1. PESC FM is expected to relieve fatigue while increasing generator speed variance. Finally, PESC FM is compared against PESC LPF in terms of generator speed regulation and fatigue mitigation. The goal is to assess which of the two techniques achieves better fatigue mitigation with the lowest degradation of the generator speed regulation.

6.2.2.3 Tuning Procedure

The tuning procedure follows the six steps listed in Section 6.2. To begin with, $\sigma^2_{\Omega_{g,i}}$ and $\sigma^2_{u_{y,i}}$ have to be estimated. In order to do so, Tuning 2 ESC is simulated and the estimated variances are listed in Table 6.4

Nac	1	2	3	4
$\sigma^2_{\Omega_{g,i}}$	24.6^2	24.6^2	24.6^2	24.6^2
$\sigma^2_{u_{y,i}}$	0.75	0.75	10	10

Table 6.4: Experimental variances of the generator speed and of the fore - aft nacelle displacement.

Next, W_i for $i = 1, ..., 4$ is set to 1 and the PESC FM is tuned to work with the new measured cost. The goal in this phase is to assess whether it is possible to achieve fatigue mitigation by loosening the control action on the generator speed. At the end of phase 1, the variance of the generator speed will be higher than in Tuning 2 ESC (Table 5.4) but fatigue will possibly be mitigated. The order of magnitude of $\sigma^2_{\Omega_g}$ can be utilized as scaling factor for the PI gains. Given that the order of magnitude of $\sigma^2_{\Omega_g}$ is 10^2, the measured cost is 100 times smaller than before. Hence, the PI gains should be scaled up by a factor of at least 100. The gains are chosen so that the interval spanned by the generator speed during the simulation is doubled. With Tuning 2 ESC the generator speed never exits the interval 122.9 ± 7 in rad/s. The interval spanned with the new gains is ± 15 in rad/s. The resulting ESC parameters are listed in Table 6.5.

Increasing the variance of the generator speed proves useful to mitigate fatigue compared to Tuning 2 ESC as the DELs ratios in Table 6.6 indicate. The correlation between closed loop bandwidth and generator speed regulation found in Section 5.3.2 could be used to explain this behaviour. A milder control action is probably moving the closed loop bandwidth to the left of the smaller mode shapes frequencies, thus reducing the excitation caused by the control action on the mode shapes frequencies listed in Table 5.7.

Gains	Values
k_p	1.2 (All SRTs)
k_i	13.5 (bottom)
k_i	10.5 (top)
p	3 s/rad (All SRTs)

Table 6.5: ESC FM, tuning parameters after Step 2 from the procedure defined in Section 6.2.

The excitation has a direct impact on fatigue because it influences the amount of extra power density in the PSDs of the loads, as documented in Section 5.4. In particular, the higher the excitation at those frequencies the more the induced fatigue.

DELs	Ratios
Tower Root Moment (Mxy)	0.90
Yaw 1 Moment (Mz)	0.68
Yaw 2 Moment (Mz)	0.67
Arm 1 Root Moment (Mx)	0.78
Arm 2 Root Moment (Mx)	0.75
Arm 3 Root Moment (Mx)	0.84
Arm 4 Root Moment (Mx)	0.82

Table 6.6: ESC FM vs Tuning 2 ESC, DELs ratios test, after Step 2 from the procedure defined in Section 6.2.

Finally, the gains W_i can be gradually reduced to include the compensation of the fore - aft nacelle displacement in the ESC loop. The following procedure is utilized:

1. Reduce W_1 gradually. Check the generator speed variance and the DELs against Tuning 2 ESC, every time W_1 is modified. The lower bound on W_1 is when 1 % reduction in the DELs ratios can be achieved only by large increment of the interval spanned by the generator speed.

2. Keep W_1 constant. Reduce W_4 gradually. Act as in step 1.

The resulting W_i gains are collected in Table 6.7

Gain	W_1	W_2	W_3	W_4
Step 1	0.75	1	1	1
Step 2	0.75	1	1	0.8

Table 6.7: W_i for $i = 1, ..., 4$ after Step 1 and Step 2.

The DELs ratios against Tuning 2 ESC are showed in Table 6.8, comparing the results in Table 6.6 with Step 1 and Step 2. As expected, the main result of the scheme is the

reduction of fatigue due to platforms torsion (Yaw 1 and 2 Moments). On top of that, the scheme slightly mitigates fatigue due to Arms torsion. The scheme neither improves the Tower Root Moment, at least when testing in the benchmark wind conditions, nor worsens that fatigue index.

DELs	Ratios Step 0	Ratios Step 1	Ratios Step 2
Tower Root Moment (Mxy)	0.90	0.90 (=)	0.90 (=)
Yaw 1 Moment (Mz)	0.68	0.64 (-4 %)	0.63 (-1 %)
Yaw 2 Moment (Mz)	0.67	0.67 (=)	0.64 (-3 %)
Arm 1 Root Moment (Mx)	0.78	0.77 (-1 %)	0.77 (=)
Arm 2 Root Moment (Mx)	0.75	0.75 (=)	0.74 (-1 %)
Arm 3 Root Moment (Mx)	0.84	0.84 (=)	0.84 (=)
Arm 4 Root Moment (Mx)	0.82	0.82 (=)	0.81 (-1 %)

Table 6.8: PESC FM vs Tuning 2 ESC, DELs ratios test. The table compares the ratios in Table 6.6 (Step 0) with Step 1 and Step 2. The ratios improvements brought by Step 1 and Step 2 are highlighted in green.

DELs	Ratios Step 2	Ratios Step 3	Ratios Step 4
Tower Root Moment (Mxy)	0.90	0.90 (=)	0.90 (=)
Yaw 1 Moment (Mz)	0.63	0.63 (-1 %)	0.65 (+2 %)
Yaw 2 Moment (Mz)	0.64	0.61 (-3 %)	0.61 (=)
Arm 1 Root Moment (Mx)	0.77	0.76 (-1 %)	0.75 (-1 %)
Arm 2 Root Moment (Mx)	0.74	0.73 (-1 %)	0.72 (-1 %)
Arm 3 Root Moment (Mx)	0.84	0.84 (=)	0.84 (=)
Arm 4 Root Moment (Mx)	0.81	0.81 (=)	0.81 (=)

Table 6.9: PESC FM vs Tuning 2 ESC, DELs ratios test. The table compares the Step 2 ratios with Step 3 and Step 4 . Highlighted in green are the ratios improvements brought by Step 3 and Step 4. In red are marked the DELs ratios are worsened..

The consequent step is to investigate whether it is possible to obtain even more fatigue mitigation, by enabling the trade-off in SRT 2 and 3. The gains W_i are gradually lowered until no further improvement is achieved in the DELs ratios. First, W_3 is reduced (Step 3). The lower bound on W_3 is found to be 0.8. As showed in Table 6.9 the new tuning allows to relieve fatigue due to Yaw 2 Moment and Arm 1 and Arm 2 Moments. Finally, W_2 is reduced (Step 4). No improvement is obtained until the lower bound $W_2 = 0.75$ is reached. At that point, fatigue due to Arm 1 and Arm 2 Moments is slightly relieved. However, fatigue due to Yaw 1 Moment is increased. This fact suggests that, at least in the simulated scenario, the ESC loops in the bottom SRTs might be competing against each other, thus worsening fatigue due to platform torsion. The final W_i gain configuration is summed up in Table 6.10. Step 3 will be utilized in

the following to study PESC FM in the frequency domain and to make comparisons against PESC LPF, because it does not worsen any of the DELs ratios.

Gain	W_1	W_2	W_3	W_4
Step 3	0.75	1	0.8	0.8
Step 4	0.75	0.75	0.8	0.8

Table 6.10: W_i for $i = 1, ..., 4$ after lowering W_3 and finally W_4.

The price to be paid to achieve fatigue mitigation is an increased generator speed variance, as shown in Table 6.12. This is quite expected because the tuning achieved in Step 0 already reduced the action of the generator speed controller. Furthermore the lower W_i the smaller impact of $y_{gr,i}$ on the measured cost (6.5) is expected.

Nac	$\overline{\Omega_g}$ Ratio	Var(Ω_g) Ratio
1	1.00	4.4
2	1.00	2.5
3	1.00	2.9
4	1.00	2.4

Table 6.11: Tuning 2 ESC vs PESC FM, generator speed mean and variance ratios test.

6.2.2.4 Frequency Analysis

In Section 6.2.2.1 it was argued that the ESC loops 1 and 4 introduce more power density, compared to the BMC, than ESC loops 2 and 3 do. Then, it was decided to enable fore - aft displacement compensation in SRTs 1 and 4, where there was more power density to be removed. The combined action of the tuning Steps 0 to 3 proves to be useful to attenuate the PSDs of the pitch references 1 and 4, as shown in Figure 6.7. The attenuation happens especially in the frequency range where the dithering and the demodulation process impact the PSD the most, i.e. around $\omega_p = 8.5$ in rad/s and $2\omega_p = 17$ in rad/s. Pitch 2 experiences also some power attenuation, especially in the neighbourhood of ω_p. Apparently the attenuation at SRT 2 is more due to Step 0 than Steps 1 to 3. In fact, $W_2 = 1$, i.e the measured cost in SRT 2 does not compensate for nacelle fore - aft displacement. The mitigation influences also the PSDs of the thrust forces, as Figure 6.8 shows clearly. Similarly to the pitch references, attenuation happens mainly on thrust 1 and 4.

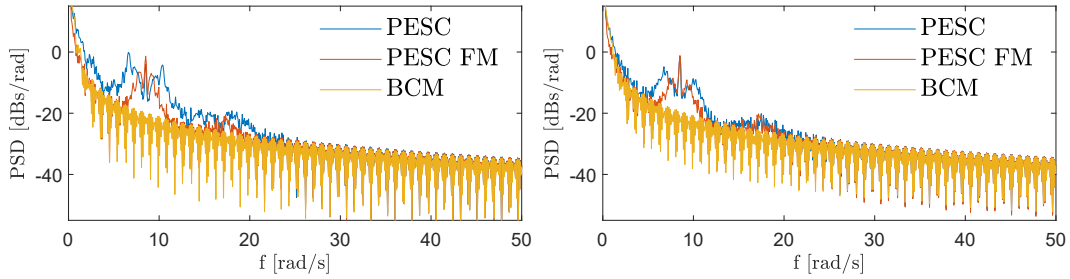

(a) Pitch Reference 1 (b) Pitch Reference 2

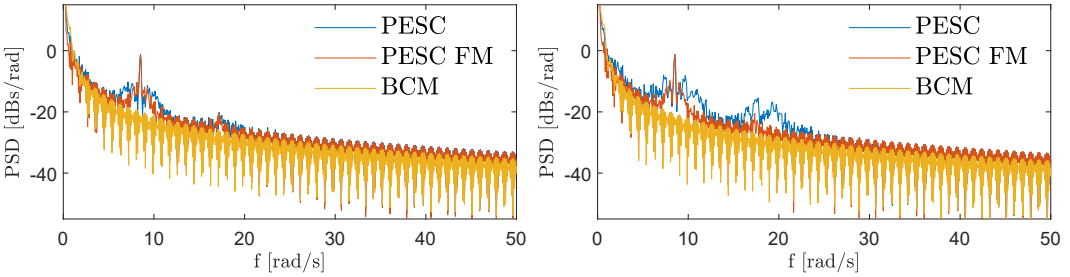

(c) Pitch Reference 3 (d) Pitch Reference 4

Figure 6.7: PESC FM Step 3 vs Tuning 2 ESC, PSDs of the pitch references compared. In yellow is the PSD of the BMC pitch references.

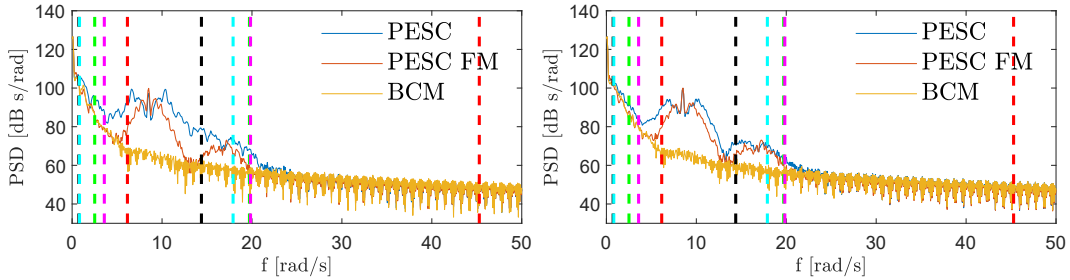

(a) Thrust Force 1 (b) Thrust Force 2

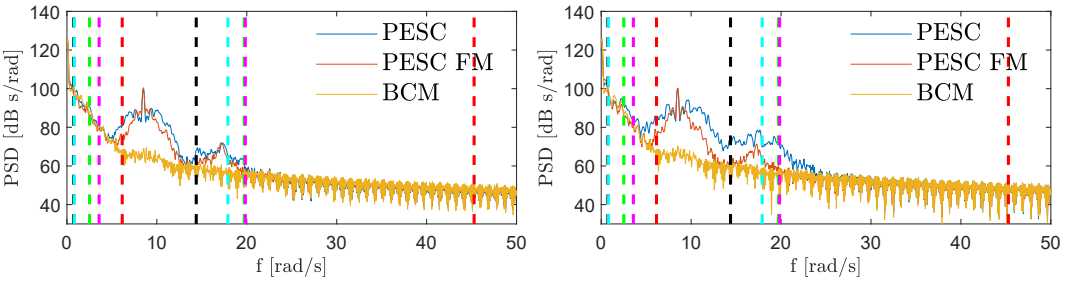

(c) Thrust Force 3 (d) Thrust Force 4

Figure 6.8: PESC FM Step 3 vs Tuning 2 ESC, PSDs of the thrust forces compared. In yellow is the PSD of the BMC thrust forces. The dashed lines are the frequencies of the mode shapes listed in Table 5.7.

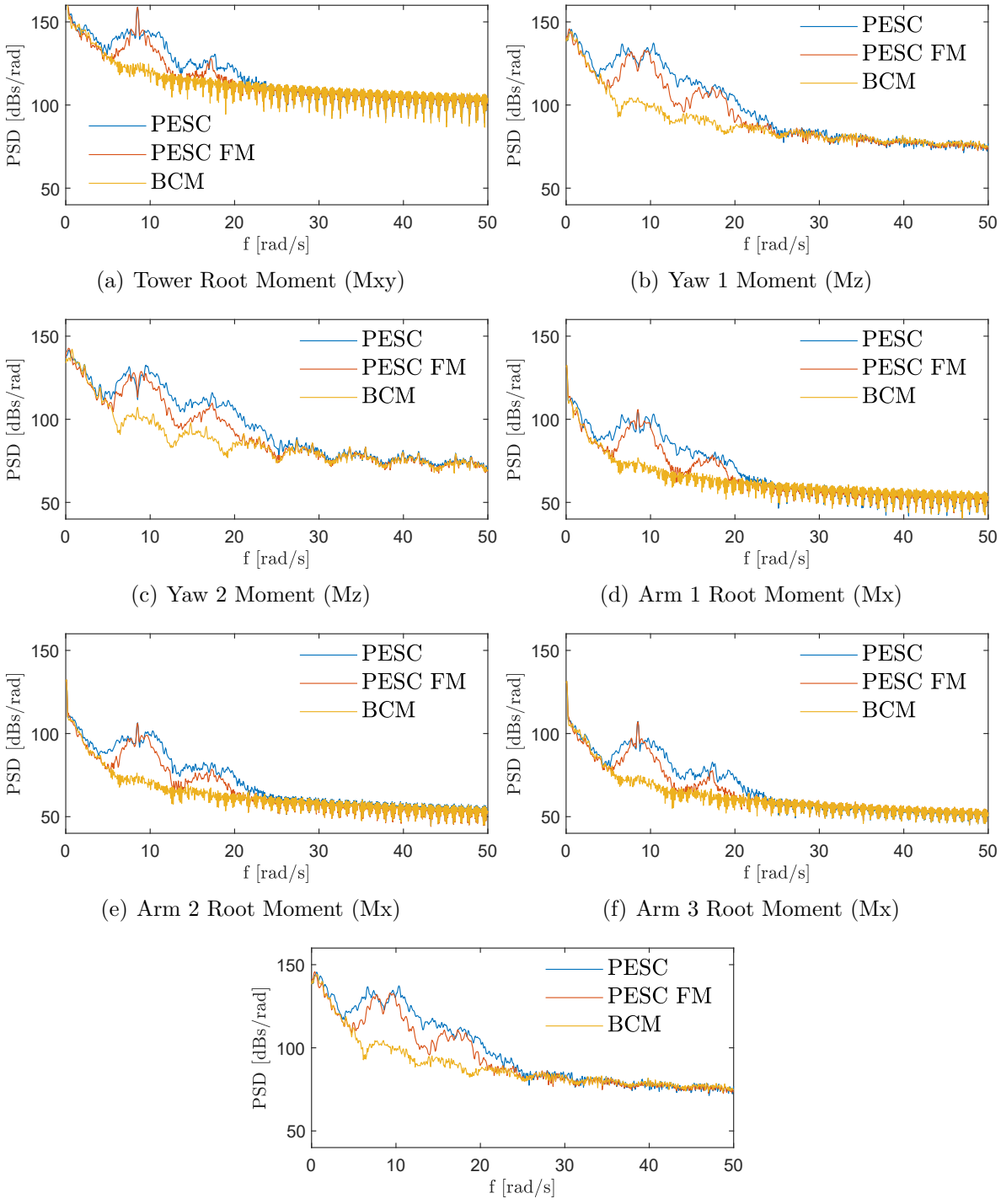

(a) Tower Root Moment (Mxy)

(b) Yaw 1 Moment (Mz)

(c) Yaw 2 Moment (Mz)

(d) Arm 1 Root Moment (Mx)

(e) Arm 2 Root Moment (Mx)

(f) Arm 3 Root Moment (Mx)

(g) Arm 4 Root Moment (Mx)

Figure 6.9: PESC FM Step 3 vs Tuning 2 ESC, PSDs of the loads compared. In yellow is the PSD of the BMC loads.

Following the interpretation given in Section 5.4, the lower power density is injected

in the frequency range where most of the mode shapes are, the lower power excess is expected in the loads that are utilized to evaluate fatigue. This is actually confirmed by inspecting Figure 6.9.

6.3 Discussion about PESC LPF and PESC FM

The comparison between PESC LPF and PESC FM (Step 3) will be carried out based on two criteria:

- achieved fatigue mitigation compared to Tuning 2 ESC
- widening of the generator speed variance compared to Tuning 2 ESC

First, the DELs ratios, listed in Table 6.2 and in the third column of Table 6.9, are compared in Table 6.12. PESC FM improves all the ratios except for Yaw 1 Moment, which in fact is worsened by 1 % and the Tower Root Moment, which remains unchanged. To the extent of the simulations with the benchmark wind scenario, PESC FM (Step 3) produces slightly lower structural fatigue than PESC LPF.

DELs	Ratios PESC LPF	Ratios PESC FM	Improvement
Tower Root Moment (Mxy)	0.90	0.90	(=)
Yaw 1 Moment (Mz)	0.62	0.63	+1 %
Yaw 2 Moment (Mz)	0.63	0.61	-2 %
Arm 1 Root Moment (Mx)	0.79	0.76	-3 %
Arm 2 Root Moment (Mx)	0.75	0.73	-2 %
Arm 3 Root Moment (Mx)	0.85	0.84	-1 %
Arm 4 Root Moment (Mx)	0.84	0.81	-3 %

Table 6.12: PESC LPF vs PESC FM, DELs ratios compared.

The ratios of the generator speed variances obtained with the two fatigue mitigation approaches are compared in Table 6.13. PESC FM reduces the variances ratios in all SRTs except for SRT 3, which is slightly worsened. It is also possible to compare speed regulation performance by plotting the generator speed of each SRT followed by the local wind speed, as done in Figure 6.10. PESC FM reacts faster to sudden drops in the wind speed, especially in bottom SRTs. For instance, this happens at around 50 seconds in the first SRT or at around 150 seconds in the second one. As shown in Figure 6.10 (c), the small increase in the variance ratio of SRT 3 does not lead to degradation of the generator speed regulation.

Finally, the PSDs of the loads are compared for PESC FM and PESC FM, to assess which strategy is attenuating the extra power density the most. Figure 6.11 shows that PESC LPF have a more aggressive attenuation effect than PESC FM, especially in the

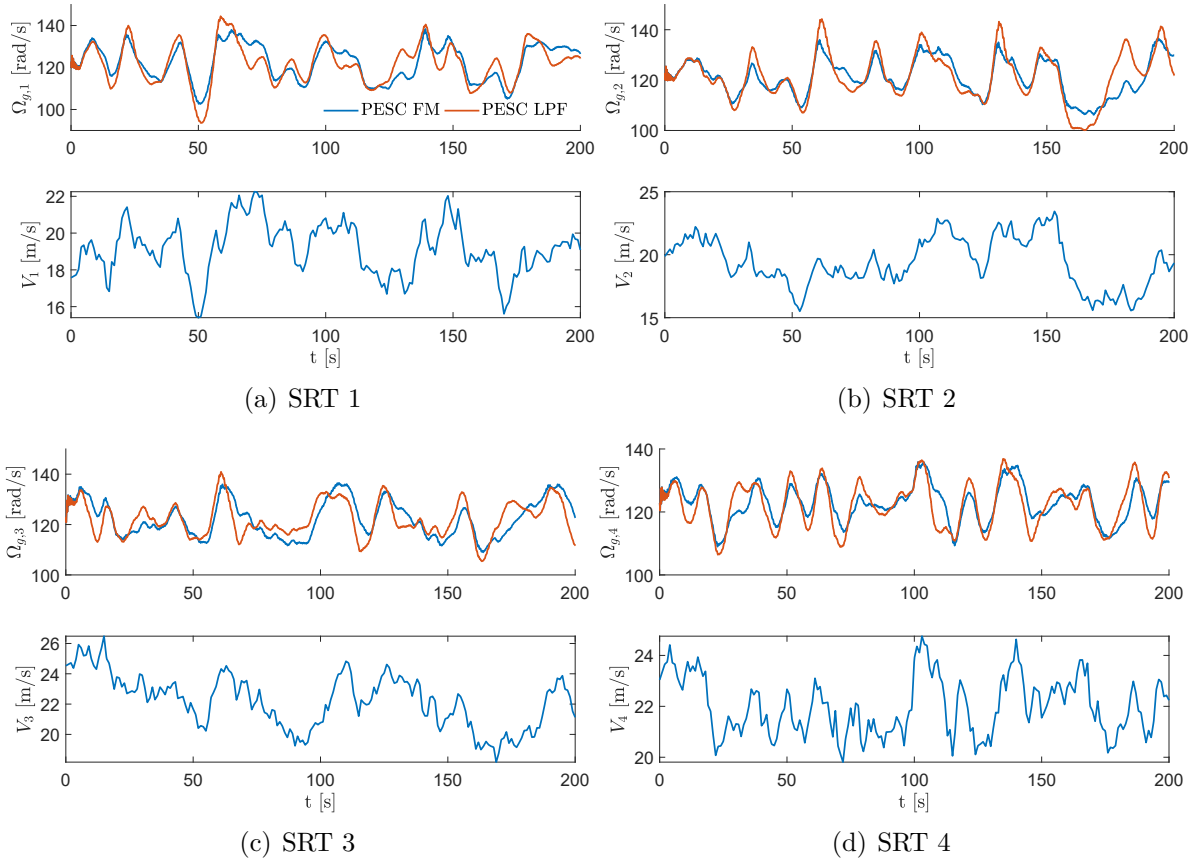

(a) SRT 1 (b) SRT 2

(c) SRT 3 (d) SRT 4

Figure 6.10: PESC FM vs PESC LPF, plots of the generator speed at nacelle i, followed by the benchmark wind scenario at nacelle i.

Nac	PESC LPF	PESC FM
1	5.3	4.4
2	4.2	2.5
3	2.5	2.9
4	3.5	2.4

Table 6.13: PESC LPF vs PESC FM, generator speed variance ratios compared.

frequency range around $2\omega_p$. To the extent of the simulations with the benchmark wind scenario, this behavior does not imply better performance in terms of fatigue mitigation and generator speed regulation, as reported in Table 6.12 and 6.13 respectively. However, it is not possible to conclude that PESC FM is always a more suitable approach than PESC LPF to mitigate fatigue. In fact, such a statement should be supported by simulations at different average wind speed scenarios. Moreover, increasing the order of the low pass filter might improve performance of PESC LPF, thus reducing the variance of the generator speed and obtaining further fatigue mitigation. Some unsuccessful attempts to increase the order of the filter were made during the project.

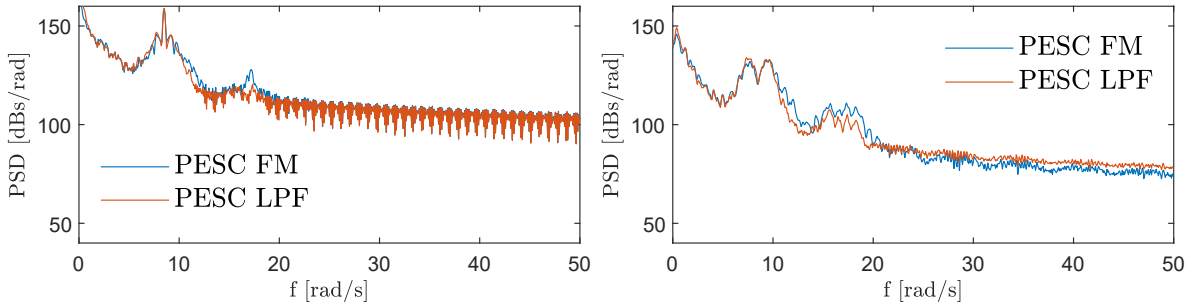

(a) Tower Root Moment (Mxy)

(b) Yaw 1 Moment (Mz)

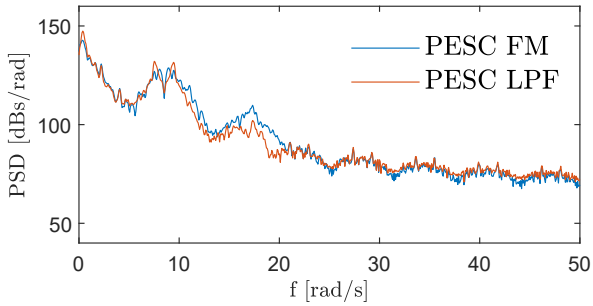

(c) Yaw 2 Moment (Mz)

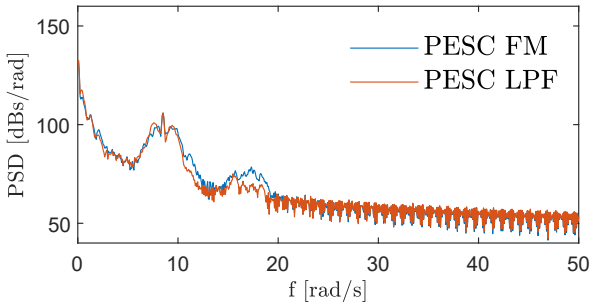

(d) Arm 1 Root Moment (Mx)

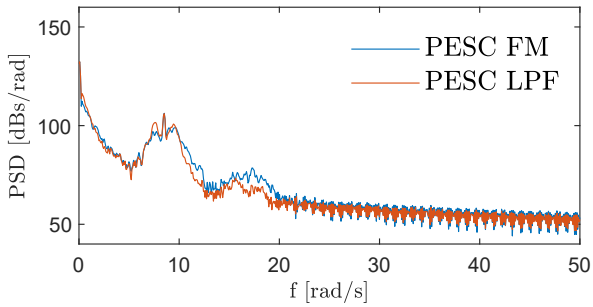

(e) Arm 2 Root Moment (Mx)

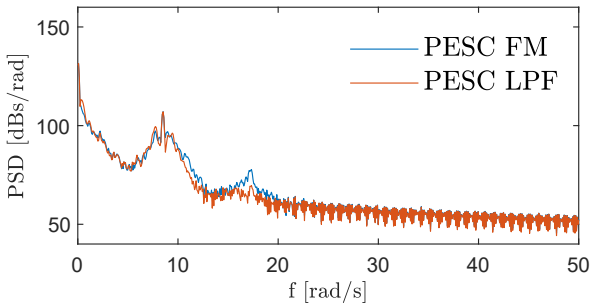

(f) Arm 3 Root Moment (Mx)

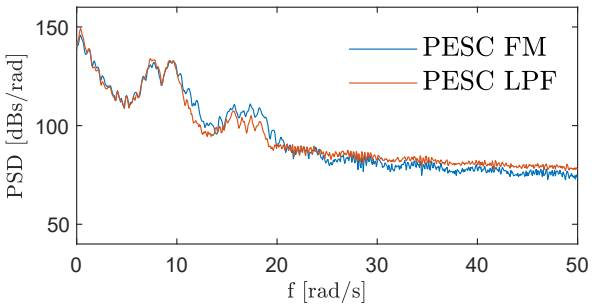

(g) Arm 4 Root Moment (Mx)

Figure 6.11: Comparing the PSDs of the moments utilized to compute the DELs. The blue line refers to the PESC without low pass filter. The red line is the PSD of the ESC including the low pass filter design.

The main challenge was to achieve more aggressive attenuation within the relevant frequency range, while limiting the phase shift introduced by the filter that could destabilize the closed-loop system. None of the proposed fatigue mitigation strategies outperforms the BMC, at least in the short simulation time horizon and in the benchmark wind conditions. In fact, the reduction of the DELs ratios with respect to Tuning 2 ESC showed in Table 6.12, are not enough to cover the gap with the BMC reported in Table 5.6. As witnessed by the extent of the carried out simulations, it is evident that the PESC is not suitable for handling fatigue mitigation, despite being able to stabilize the generator speed by generating pitch references without knowledge of the wind speed. In particular, letting the PESC directly regulate the pitch references, proved to inject a lot of extra power density to the structure, that sensibly exacerbates fatigue. A potential way to reduce this effect could be to prevent the PESC from directly regulating the pitch references. Instead, the PESC could be integrated into the baseline PI controllers for pitch regulation and be utilized to dynamically tune the proportional and integral gains during operations.

CHAPTER 7

Conclusions and Future Work

This chapter elaborates the conclusions of the project based on the results of the analysis developed in the previous chapters. The conclusions are utilized to provide some suggestions for future work.

7.1 Conclusions

In fulfilment to the Scope Statement elaborated in Section 1.4, the project proposed a 4 SISO ESC based architecture to provide each SRT with an optimal pitch reference. With the system operating in FLR, the generator power reference has been fixed to its rated value P_N. The first ESC design developed in Chapter 4 was tuned to achieve generator speed regulation in the benchmark wind scenario (Tuning 2 ESC). The fatigue mitigation strategies described in Chapter 6 required a new design of the input compensator (PESC LPF) and the modification of the measured cost (PESC FM), respectively. As observed by the extent of the simulations and the analysis carried out in Chapter 5 and 6, the following conclusions are made with respect to conditions 1 to 3 from Section 1.4:

Generator speed regulation Each of the three ESC schemes proved suitable to regulate the generator speed of each SRT, without relying on the knowledge of the wind speed and of the plant model during operations. In particular, Tuning 2 ESC allowed to achieve as good speed regulation as the BMC. However, both (PESC LPF) and (PESC FM) worsened generator speed regulation, by increasing the variance of the generator speed, whenever fatigue mitigation was attempted.

Power production The proposed schemes were all suitable to generate the expected power output, even when the ESC was causing degradation of generator speed regulation to achieve fatigue mitigation. Based on the industry experience [29], it is concluded that in a real application power production might be affected by the quality of the generator speed regulation.

Fatigue on the support structure The pitch references produced by Tuning 2 ESC in Chapter 5 showed an oscillatory behaviour during the whole simulation. The oscilla-

tions were introduced by the probing signals and were needed by the ESC to estimate the pitch references. However, such a behaviour had two negative side effects. On the one hand it increased the pitch activity, which in turn might shorten the actuator life in the long run. On the other hand, the spectral analysis of the pitch references in Chapter 5 showed an increased power density, which propagated through the thrust forces into the support structure. This fact explained the higher structural fatigue caused by Tuning 2 ESC compared to the BMC. The mitigation techniques developed and tested in Chapter 6, namely PESC LPF and PESC FM, considerably reduced fatigue compared to Tuning 2 ESC, by acting on the extra power density. However, it was never possible to mimic the performance of the BMC. To the extent of the simulations and analysis carried out in this project, it is concluded that letting the ESC loops directly compute the pitch references is not a suitable strategy to achieve fatigue mitigation.

ESC is a powerful model-free technique suitable to achieve the generator speed regulation and mean power production objectives of the project. However, the ESC is not suitable to achieve fatigue mitigation by computation of the pitch references, because the oscillations needed to keep the estimation of the references operative has a clear negative impact on fatigue. The conclusions outlined in this section are utilized to elaborate on the future work.

7.2 Future work

The work carried out during this project constitutes the baseline for future work. Some suggestions are elaborated in the following, based on the conclusions presented in Section 7.1:

1. The behaviour of the BMC and of the ESC should be simulated for longer wind scenarios that cover the whole FLR and be compared based on those simulations. By doing so the comparison will assess the behaviour of the two techniques in a wider range of wind speeds within each scenario.

2. The model of the generator implemented in the simulation environment [2] has a constant efficiency with respect to the generator speed. It might be relevant to investigate how wider generator speed variance due to fatigue mitigation would impact power production for a varying generator efficiency.

3. In Chapter 7 it was concluded that ESC is not suitable to achieve fatigue mitigation by direct computation of the pitch references. During the final stage of the project, the effectiveness of ESC as auto-tuning routine was investigated by means of preliminary simulations. More specifically, the estimation of the pitch references was in charge of the baseline PI regulators [23]. However, the proportional and the integral gains were optimized during operations by the ESC routine. Simulations tests showed that the scheme proved effective in achieving levels of fatigue

comparable to the BMC, while reducing the variance of the generator speed. Furthermore, the resulting pitch references were smooth because the probing signals were acting on the control gains. Future works could include investigating the effectiveness of this technique in a wider range of wind scenarios.

Appendices

APPENDIX A

Frequency Response Estimation

The frequency response quantifies the output spectrum of a dynamic system to an input, whose action spans a certain frequency range. The frequency response takes complex values for each frequency. It measures the amplitude and the phase of the output, compared to the input as a function of the frequency. In Linear Time Invariant (LTI) BIBO stable systems the frequency response $H(j\omega)$ can be obtained by evaluating the system transfer function(s) $H(s)$ in $j\omega$, $\omega \in \mathbb{R}_{\geq 0}$ being positive real frequencies. If a sine wave at a certain frequency is injected into an LTI system, the output is still a sine wave with the same frequency but different amplitude and phase.
The analytic transfer function from wind speed to pitch reference is not available when the ESC is active, due to the non-linearity introduced by the dithering and demodulation processes. However, it is possible to estimate the frequency response by means of time domain experiments. The experiments inject sinusoidal wind inputs to an SRT in a relevant frequency range. Ignoring the high frequency component in the pitch reference due to dithering and demodulation, the output is assumed to be sinusoidal with approximately the same frequency as the input, but different amplitude and phase. In other words it is assumed that the averaged system is approximately LTI. The first harmonic of the Fourier series approximates the pitch reference as follows

$$\mathcal{F}(\beta) \approx a_0 + a_1 \cos \omega t + b_1 \sin \omega t \tag{A.1}$$

Indeed, the first harmonic averages the high frequency components away. The bias a_0 represents the average wind speed, hence it is neglected. Using trigonometry formulas it is possible to rewrite the approximation as

$$\mathcal{F}(\beta) = K \sin(\omega t + \phi) \tag{A.2}$$

$K \geq 0$ being the amplitude and ϕ being the phase shift. The values are obtained by the coefficients a_1 and a_2 of (A.1)

$$K = \sqrt{a_1^2 + b_1^2} \tag{A.3}$$

$$\tan \phi = \frac{a_1}{b_1} \tag{A.4}$$

The frequency response is represented through the Bode plot, which includes a plot of the amplitude in dB and of the phase shift in degrees. The amplitude is computed as $|H(j\omega)|_{dB} = 20\log_{10}\frac{K}{A}$, A being the amplitude of the input sine. The experiments utilize unitary amplitude sine waves as input, hence $|H(j\omega)|_{dB} = 20\log_{10}K$. The phase shift corresponds to ϕ because the input sine has zero phase shift.

Bibliography

[1] Kartik B. Ariyur and Miroslav Krstic. *Real-Time Optimization by Extremum-Seeking Control*. Wiley, 2003. ISBN: ISBN: 978-0-471-46859-2. accessed: 25-1-2019.

[2] Vestas Wind System A/S. *MRTCC*. 2018. URL: `https://github.com/kihso/MRTCC`. accessed: 25-01-2019.

[3] J. J. Barradas-Berglind and Rafael Wisniewski. "Representation of fatigue for wind turbine control". In: *Wiley Online Library* (2016), pp. 2189–2203. DOI: `10.1002/we.1975`. accessed: 11-02-2019.

[4] J. J. Barradas-Berglind, Rafael Wisniewski, and Mohsen Soltani. "Fatigue damage estimation and data-based control for wind turbines". In: *IET Control Theory Applications* (2014), pp. 1042–1050. DOI: `10.1049/iet-cta.2014.0730`. accessed: 11-02-2019.

[5] Fernando D Bianchi, Hernan De Battista, and Ricardo J Mantz. *Wind Turbine Control Systems. Principles, Modelling and Gain Scheduling Design*. Springer, 2006. ISBN: 978-1-84628-493-9. accessed: 25-1-2019.

[6] Benjamin Biegel et al. "Distributed Low-Complexity Controller for Wind Power Plant in Derated Operation". In: *IEEE International Conference on Control Applications* (2013), pp. 146–151. DOI: `10.1109/CCA.2013.6662758`. accessed: 07-02-2019.

[7] Martin Brokate and Klaus Dreßler. "Rainflow Counting and Energy Dissipation for Hysteresis Models in Elastoplasticity". In: *European Journal of Mechanics, A/-solids* (1996), pp. 705–737. accessed: 12-02-2019.

[8] Martin Brokate and Jiirgen Sprekels. *Hysteresis and Phase Transitions*. Springer, 1996. ISBN: 978-1-4612-4048-8. accessed: 12-02-2019.

[9] CENELEC. *Wind turbines - Part 1: Design requirements*. 2010.

[10] Justin Creaby, Yaoyu Li, and John E Seem. "Maximizing wind turbine energy capture using multivariable extremum seeking control". In: *Wind Engineering* (2009), pp. 361–388. DOI: `10.1260/030952409789685753`. accessed: 05-03-2019.

[11] S Dougherty and M Guay. "An Extremum-Seeking Controller for Distributed Optimization Over Sensor Networks". In: *IEEE Transactions on Automatic Control* (2016), pp. 928–933. DOI: `10.1109/TAC.2016.2566806`. accessed: 14-02-2019.

[12] Judith Ebegbulem and Martin Guay. “Power Maximization of Wind Farms using Discrete-time Distributed Extremum Seeking Control”. In: *IFAC* (2018), pp. 339–344. DOI: 10.1016/j.ifacol.2018.09.323. accessed: 14-02-2019.

[13] Wind Europe. *UPWIND*. 2011. URL: https://windeurope.org/policy/eu-funded-projects/upwind/. accessed: 25-05-2019.

[14] Wind Energy THE FACTS. *The Cost of Energy Generated by Wind Power*. URL: https://www.wind-energy-the-facts.org/the-cost-of-energy-generated-by-wind-power.html.

[15] Aeolus FP7. *SimWindFarm*. 2011. URL: http://www.ict-aeolus.eu/SimWindFarm/model-turbine.html.

[16] PMO Gebraad and JW Van Wingerden. “Maximum power-point tracking control for wind farms”. In: *Wind Energy* (2014), pp. 429–447. DOI: 10.1002/we.1706. accessed: 07-02-2019.

[17] A Ghaffari, M Krstic, and S Seshagiri. “Power optimization and control in wind energy conversion systems using extremum seeking”. In: *1st American Control Conference* (2013), pp. 2241–2246. DOI: 10.1109/ACC.2013.6580168. accessed: 05-02-2019.

[18] A Ghaffari, S Seshagiri, and M Krstic. “Power Optimization for Photovoltaic Micro-Converters using Multivariable Gradient-Based Extremum-Seeking”. In: *1st American Control Conference* (2012), pp. 3383–3388. DOI: 10.1109/ACC.2012.6314761. accessed: 16-03-2019.

[19] Azad Ghaffari, Miroslav Krstić, and Dragan Nešić. “Multivariable Newton-based extremum seeking”. In: *2011 50th IEEE Conference on Decision and Control and European Control Conference* (2011), pp. 4436–4441. DOI: 10.1109/CDC.2011.6160495. accessed: 10-02-2019.

[20] Tomislav Horvat, Vedrana Spudić, and Mato Baotić. “Quasi-stationary optimal control for wind farm with closely spaced turbines”. In: *MIPRO. Proceedings of the 35th International Convention. IEEE* (2012), pp. 829–834. accessed: 09-02-2019.

[21] Jonas Kazda et al. “Framework of Multi-objective Wind Farm Controller Applicable to Real Wind Farms”. In: *Wind Europe Summit* (2016). URL: https://shorturl.at/eFGKL. accessed: 04-02-2019.

[22] Torben Knudsen, Thomas Bak, and Mikael Svenstrup. “Survey of wind farm control—power and fatigue optimization”. In: *Wind Energy* (2014), pp. 1333–1351. DOI: 10.1002/we.1760. accessed: 05-02-2019.

[23] Torben Knudsen et al. “Multi-rotor wind turbine control challenge - A benchmark for advanced control development”. In: *IEEE International Conference on Control Applications* (2018), pp. 1615–1622. DOI: 10.1109/CCTA.2018.8511511. accessed: 25-01-2019.

[24] Daria Madjidian, Karl Mårtensson, and Anders Rantzer. "A Distributed Power Coordination Scheme for Fatigue Load Reduction in Wind Farms". In: American Control Conference, 2011 ; Conference date: 29-06-2011 Through 01-07-2011. 2011, pp. 5219–5224. accessed: 06-02-2019.

[25] Jason R Marden, Shalom D Ruben, and Lucy Y Pao. "A Model-Free Approach to Wind Farm Control Using Game Theoretic Methods". In: *IEEE Transactions on Control Systems Technology* (2013), pp. 1207–1214. DOI: 10.1109/TCST.2013.2257780. accessed: 07-02-2019.

[26] Dragan Nesic, Ying Tan, and Iven Mareels. "On the Choice of Dither in Extremum Seeking Systems: a Case Study". In: *Proceedings of the 45th IEEE Conference on Decision and Control* (2006), pp. 2789–2794. DOI: 10.1109/CDC.2006.377309. accessed: 10-02-2019.

[27] Maryam Soleimanzadeh and Rafael Wisniewski. "Controller Design for a Wind Farm, Considering Both Power and Load Aspects". In: *Mechatronics* (2011), pp. 720–727. DOI: 10.1016/j.mechatronics.2011.02.008. accessed: 05-02-2019.

[28] Maryam Soleimanzadeh, Rafael Wisniewski, and Stoyan Kanev. "An Optimization Framework for Load and Power Distribution in Wind Farms". In: *Journal of Wind Engineering and Industrial Aerodynamics* (2012), pp. 256–262. DOI: 10.1016/j.jweia.2012.04.024. accessed: 06-02-2019.

[29] Control Specialist. Private Conversation. Vestas Wind Systems A/S, Århus, Dk, 2019.

[30] Yan Xiao, Yaoyu Li, and Mario A Rotea. "Multi-objective Extremum Seeking Control for Enhancement of Wind Turbine Power Capture with Load Reduction". In: *Journal of Physics* (2016), pp. 1–10. DOI: 10.1088/1742-6596/753/5/052025. accessed: 25-01-2019.

[31] Yan Xiao, Li Yaoyu, and John E Seem. "Multi-variable Extremum Seeking Control for Mini-split Air-conditioning System". In: *International Refrigeration and Air Conditioning Conference* (2016), pp. 1–12. DOI: 10.1.1.843.5019. accessed: 05-03-2019.

[32] C. Zhang and R. Ordóñez. *Extremum-Seeking Control and Applications*. Springer-Verlag London, 2012. ISBN: ISBN 978-1-4471-2224-1. accessed: 25-1-2019.